Rochester Institute of Technology

RIT Digital Institutional Repository

8-2021

Direct Writing of Printed Electronics through Molten Metal Jetting

Manoj Meda

mm2928@rit.edu

Rochester Institute of Technology

Direct Writing of Printed Electronics through Molten Metal Jetting

by

Manoj Meda

A dissertation submitted in partial fulfilment of the requirements for the degree of
Doctor of Philosophy in Mechanical and Industrial Engineering

Mechanical and Industrial Engineering (PhD program)
Kate Gleason College of Engineering

Rochester Institute of Technology,
Rochester, New York
August 2021

Direct Writing of Printed Electronics through Molten Metal Jetting
By
Manoj Meda

Committee Approval:

We, the undersigned committee members, certify that we have advised and/or supervised the candidate on the work described in this dissertation. We further certify that we have reviewed the dissertation manuscript and approve it in partial fulfillment of the requirements of the degree of Doctor of Philosophy in Mechanical and Industrial Engineering.

Dr. Denis R. Cormier (Advisor)   Date:

Professor, Department of Industrial and Systems Engineering

Dr. Marcos Esterman   Date:

Associate Professor, Department of Industrial and Systems Engineering

Dr. Rui Liu   Date:

Assistant Professor, Department of Mechanical Engineering

Dr. Yunbo Zhang   Date:

Assistant Professor, Department of Industrial and Systems Engineering

Table of Contents

List of Figures

List of Tables

Abstract

This research proposes a novel approach to printed electronics manufacturing via molten metal droplet jetting (MMJ). Large scale experimental work is presented to establish suitable jetting parameters for fabrication of high quality conductive electronic traces. Following process optimization, resistivity values as low as 4.49 $\mu\Omega$-cm for printed 4043 aluminum alloy traces have achieved. This essentially matches the electrical resistivity of the bulk alloy, and it represents a significant improvement over results obtained with printed nanoparticle ink electronics. Electrical resistivity of printed traces that undergo static and cyclical flexing is included in the analysis. The cross-sectional area of traces printed with this approach is orders of magnitude larger than those achieved with nanoparticle inks, hence the traces essentially behave like solid-core metal wire capable of carrying very high currents. The relationship between jetting parameters and the equivalent wire gauge of the uniform printed traces is presented.

Early experimental trials revealed the formation of large pinholes inside droplets deposited onto room temperature polyimide substrates. This was hypothesized to be due to the release of adsorbed moisture from the polyimide into the solidifying droplet. Subsequent experiments revealed that heating the polyimide substrate drives off the moisture and eliminates moisture-induced porosity.

A multi-physics Ansys process model is also presented to understand behavior of molten metal droplets as they impinge upon a temperature sensitive polymer substrate, spread out, cool down, and solidify. The process model allows the study of many process conditions without expensive and time-consuming physical experimentation.

Acknowledgements

The research work presented in this dissertation has been made possible because of the support I received from many individuals over the course of my PhD. Even though I may not have mentioned every single person by name, I am still very grateful to everyone who has assisted me in one way or the other in conducting this work. Firstly, I would like to express my sincerest gratitude to my advisor Dr. Denis Cormier for giving me the chance to not only work on an exciting thesis topic using cutting edge equipment, but also to work on several research projects in collaboration with industries.

I would like to thank my committee members Dr. Marcos Esterman, Dr. Rui Lui, and Dr. Yunbo Zhang for their feedback which has made this thesis more robust. I am grateful to Dr. Bruce Kahn, Dr. David Trauernicht and Robert Kraynik for their guidance and support in the AMPrint Center and Brinkman Lab. I am thankful to Dr. Viktor Sukhotskiy for clarifying several aspects of numerical modelling. I am very thankful to my friends Dr. Chaitanya Mahajan and Dr. Pruthvik Raghupati for their discussions and suggestions which helped me navigate the graduate school journey with better clarity. I am extremely grateful to Dr. Mandakini Kanungo for taking a chance on me and giving me the opportunity to do an internship at Corning. I'd like to thank all of my lab mates for not only your assistance in the lab but also for the many fun conversations which made the solitary graduate school journey more fun. I'd like to thank Rebecca Ziebarth for all the administrative help in the PhD program.

I'd like to express my gratitude to my parents Venkateswarlu Meda and Anjali Meda for encouraging me to pursue a PhD. I am very grateful to you for giving me the freedom to make my own choices. Finally I'd like to express my deepest gratitude to my lovely wife Sneha Chitturi for being supportive through all the ups and downs in this graduate school journey. I feel blessed to have shared this journey with you.

Chapter 1. Introduction

Manufacturing is fundamentally the process of converting raw materials into finished goods. Manufacturing of any product requires an understanding of the physical properties of raw materials being used and the technical process required to transform the materials into the desired product. Novel manufacturing techniques have been enabling the creation of new products and driving societal progress since the dawn of humanity. One of the first and oldest manufacturing technology milestones, that has in time enabled humans to become the most dominant and technologically advanced species on the earth, is the manufacturing of stone tools by our paleolithic ancestors over 2 million years ago [1]. Since the advent of stone tools, there has been an incremental increase in the collective human understanding of various material characteristics and manufacturing processes through specialization of skills and the exchange of accumulated knowledge. This has shaped the modern world; with all the diverse array of sophisticated technological devices we see around us and use every day.

In the past 300 years, manufacturing processes have been industrialized, i.e. they have transformed from hand-based to machine-based production methods. During this period, the world has witnessed three industrial revolutions that have resulted in tectonic shifts in the human way of living - from chiefly agrarian to urban societies. In the words of Klaus Schwab, the founder and chairman of the world economic forum, an industrial revolution can be defined as the appearance of "new technologies and novel ways of perceiving the world [that] trigger a profound change in economic and social structures" [2]. The first industrial revolution began around 1760 through the advent of the steam engine and revolutionized transportation, agriculture etc. The second industrial revolution was the era of mass manufacturing that began in the early 1900's with the advent of the assembly line. The third and most recent is the digital revolution, that began in the 1950's, which brought electronic devices, semiconductors, mainframe/personal computing, and the internet [2].

The advent of electronic devices through the third industrial revolution, led to the disruption of all the vital avenues of the global economy such as healthcare, energy, transportation, heavy industries, communication networks, military etc. Electronic devices have now become an integral part in the day to day lives of almost everyone in the world. The key driver for ubiquity of electronic devices around us can be attributed to the advancements in integrated circuits (IC) which have faithfully followed Moore's law and become more powerful, smaller, and affordable in every iteration [3]. Moore's law states that the number of components that could fit onto a chip double every couple of years. The faithfulness with which IC's have followed Moore's law has been primarily due to the dramatic increase in the capabilities of manufacturing processes, such as photolithography, which have enabled the fabrication of more compact and powerful IC's in every generation [3].

We are currently at the dawn of the 4th industrial revolution, which is poised to disrupt and profoundly transform the electronics landscape with the internet of things (IoT). IoT can be described as a network of diverse physical devices embedded with electronics that can connect, collect, and exchange data in real time. This integrates the physical world with the digital world and results in significant increases in productivity, incremental economic benefits, and reduced human efforts [2]. One of the key drivers for the IoT is light weight and extremely cost-efficient printed electronic appliances manufactured through various types of printing processes. Furthermore, printing processes also enable fabrication of flexible and stretchable electronics. The flexible nature of these devices makes them very well suited to be used in numerous areas where rigid electronics cannot be employed. Printed flexible electronic devices are also intended to be extremely cost-efficient and could be employed in several more avenues than rigid electronics.

Flexible electronics, with intriguing properties such as softness and ductility have broad application prospects in the communication, energy, healthcare, transportation, and defense technology fields, through a diverse array of flexible devices. Intelligent packaging, low-cost RFID (radio-frequency identification) transponders, flexible displays, flexible solar cells, flexible batteries, and disposable diagnostic/monitoring

2

devices are just a few examples of appliances possible with flexible electronics [4-8]. In addition to that, as flexible electronics use substrates such as polymers or paper - which cost significantly less than widely used rigid substrates such as silicon wafers or glass - they are also poised to be incrementally cheaper.

From a manufacturing perspective, the current state of the art fabrication techniques that have propelled progress in IC manufacturing are not well suited for fabrication of cheap flexible electronics, as they are expensive fabrication techniques that require clean room environments, thereby increasing the cost of the final product. Most of the conventional manufacturing techniques are also not designed to accommodate the low temperature flexible substrates employed in flexible electronic devices. Conversely, printing techniques that have been adapted to deposit conductive inks are very well suited for the fabrication of flexible electronics. When printing technologies are employed in manufacturing of electronic circuits and electrical components, they are often referred to as printed electronics (PE) or functional printing. The main aim of PE is to enable the fabrication of flexible/stretchable electronics while reducing the manufacturing cost of electronics per unit area, using relatively less expensive, low waste and all-additive printing methods.

1.1 Printed electronics

The origins of printing processes can be traced all the way back to the 1400's when Johannes Gutenberg developed the mechanical movable type for printing text and started the mechanical printing revolution in Europe [9]. Printing of text provided people with access to information and knowledge on a scale hitherto unseen in history. This has enabled future generations to build on the intellectual accomplishments of earlier ones on an exponential scale, and its effects were far reaching. Over the last century, the process of printing has grown from printing of text and graphics to include manufacturing of high-quality electronic devices. Using printing technologies, it is now possible to print various electrically conductive materials such as

nanoparticles [10], conductive polymers [11], and metals [12] on a diverse array of flexible substrates such as polymers [13], paper [14], fabrics [15] to fabricate various flexible electronic devices.

The idea of printing circuits and wiring boards can be dated to the 1950's, when gravure printing was proposed as a promising manufacturing process for fabricating electronics [16]. Printed electronics took off after a couple of decades when Nobel laureates Alan Heeger, Alan MacDiarmid, and Hideki Shirakawa realized the first conducting polymers [17]. Over the next three decades, PE technologies have come of age, and it is now feasible to employ PE techniques for manufacturing a diverse array of electronic products that are thin, flexible, stretchable, wearable, lightweight, cost-effective, and environmentally friendly [16].

In terms of the market penetration for PE appliances, the first PE products reached the consumer market in the mid 2000's [4]. PE technologies are currently being employed in the fabrication of a diverse array of devices such as flexible batteries [18], flexible photovoltaics [19], flexible active matrix light emitting diodes (AMLED) [20], flexible organic field effect transistors (OFET) [21], flexible displays [22], disposable radio frequency identification (RFID) tags [23], gas sensors [24] large area pressure sensors [25] etc. Figure 1.1 shows some printed functional appliances in the published literature. With a market size of about US $31.7 billion in 2019, PE technologies are finding their stride in capturing the inexpensive electronics market [26]. According to the market research firm IDTechEx, the market for printed electronics is projected to reach US $73B by 2029 [26]. The Organic Electronics Association (OE-A), an industry association for organic and printed electronics, projects the combined market for organic and printed electronics to reach US $200B in the next decade [27].
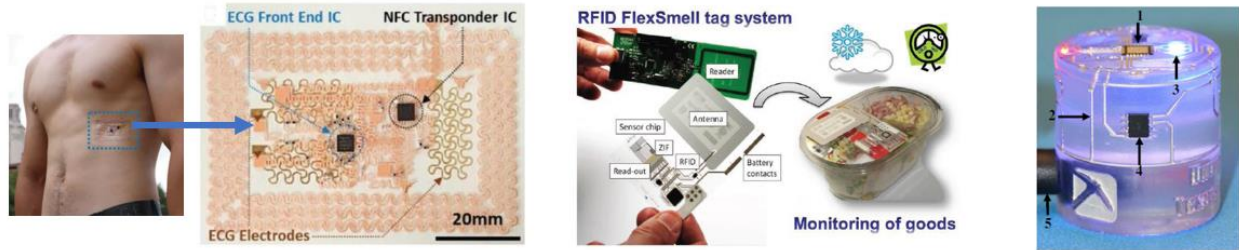
Figure 1.1 (a) A peel-and-stick form factor wearable ECG patch (used with permission from [28]) (b) Multi sensor platform for monitoring freshness of food (used with permission from [29]) (c) A 3D printed magnetic flux sensor with embedded electronics (used with permission from [30].

1.2 Direct writing

Traditionally, electronic devices have been primarily fabricated by subtractive manufacturing techniques such as photolithography [3], electroless plating [31], chemical vapor deposition [32], physical vapor deposition [33] etc. These techniques have facilitated the fabrication of printed circuit boards (PCB) and ushered tremendous advancements in modern electronics. However, these fabrication techniques are multistage processes that require high-cost equipment and huge upfront costs.

An illustration of photolithography technology – the most widely used PCB manufacturing process – is shown in Figure 1.2 to demonstrate the various process steps in the complex, multistage, subtractive fabrication technique. The established techniques are also energy intensive, require special clean room environments, use environmentally undesirable chemicals that are corrosive and also result in the formation of huge amounts of waste [34]. Several of the polymer-based materials used for the flexible substrates tend to be incompatible with the high temperature processing conditions employed in these processes, making them less than ideal for manufacturing of flexible electronic devices [33].

5
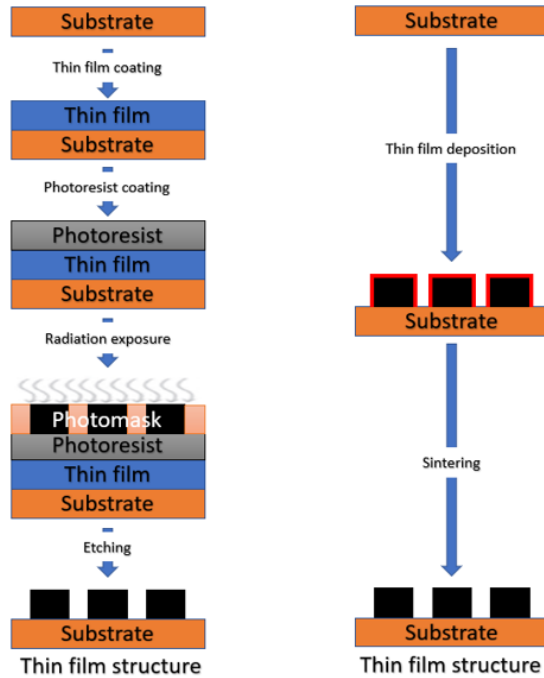
Figure 1.2 A schematic diagram comparing conventional subtractive manufacturing technology and direct writing technology.

At this juncture, pattern-based printing processes such as flexography [35], gravure [36], screen printing [37] etc. were investigated as viable alternatives to fabricate flexible electronic circuits with low material waste and higher throughput. The high throughput capability of these techniques makes them well suited for high volume manufacturing of various functional devices. Several devices such as flat panel displays, printed antennas, transparent electrodes etc. have been manufactured on a large scale using these techniques [38]. However, these processes employ master patterns to print the materials. The fabrication of patterns involves several complicated steps. The manufacturing of master patterns tends to increase the production time and cost, especially in situations where the production volumes are low [16]. Due to the limitations associated with the conventional manufacturing techniques and pattern based printing techniques, the research in PE progressed into developing manufacturing processes that are faster, cheaper and more eco-friendly for fabrication of flexible electronic circuits [34].

6

Digital printing processes proved to be well suited for manufacturing flexible electronics, as they are completely additive, non-impact, digital patterning techniques, that involve significantly fewer processing steps. Some of these processes are also referred to as direct writing (DW), as they can directly deposit functional materials on to the substrate in a precise manner. These processes are capable of printing complex patterns of circuitry at digitally defined locations directly from the computer aided design (CAD) files without the need for any master patterns. This provides complete control over the printing process.

These attributes facilitate rapid design iterations and reduce the prototyping time, which is very helpful in manufacturing of electronics which tend to have very short product life cycles. The completely additive manufacturing attributes of DW processes also results in significant reduction of material waste, making them much more environmentally friendly than conventional fabrication techniques [39, 40]. Some DW techniques are also capable of depositing material on both planar and non-planar substrates, which enables the development of sensors and circuits that conform to curved surfaces. This is extremely difficult to achieve using conventional wafer-based techniques and pattern-based printing methods. This unique ability of DW processes to exploit the mechanically flexible form-factor of abundant and cheap materials helps in achieving inexpensive flexible electronic devices.

One limitation of DW is that these processes currently have a feature resolution in the 10's of microns, which is about a couple of orders of magnitude larger than the achievable resolution using subtractive manufacturing techniques. Furthermore, the electrical performance of printed features is also lower than the features fabricated using conventional subtractive manufacturing techniques. Consequently, printing techniques are not used as a replacement for conventional electronics manufacturing technologies such as lithography; rather, they serve as complimentary technologies that can enable the manufacture of very low-cost flexible electronics. Although DW techniques are very attractive due to them being completely additive, completely digital, non-impact, and having fewer processing steps, they currently have some limitations that have prevented them from being more widely adopted for high volume manufacturing.

1.3 Limitations of direct writing processes

Direct writing techniques encompass a wide array of deposition methods including inkjet printing [41], aerosol based deposition [42], micro-extrusion [43] etc. These techniques generally tend to use functional materials in dispersion or solution ink forms. Depending on the deposition technique and the substrate, the inks require specific rheological properties to achieve high resolution patterns and good adhesion on to the substrate. Low temperature processing conditions are also essential because typical flexible polymer substrates undergo a glass transition around 150-200°C, and the subsequent deformation of the substrate at higher temperatures may detrimentally impact the performance of the printed devices [44].

Various electrically conductive materials such as nanoparticles [10], polymers [11], metals [12] etc. have been used as key components of functional inks. Among them, metal-based inks such as metal nanoparticle (NP) inks [10] and Metal-Organic Decomposition (MOD) inks [45] have become the main system of choice for fabrication of electronic circuitry due to their potentially high electrical conductivity and desirable physical behavior with the substrates. Electrical resistivity on the order of 2-8 times the bulk conductivity of the metals has been achieved using the metal-based inks [10, 46] .

While printed metal inks are promising, fabrication of an electrically conductive circuit using metal-based inks is not a single step process. Both the metal NP and MOD inks require additional post processing steps such as drying and curing or sintering in order to achieve reasonable electrical conductivity. In these steps, the electrically non-conductive organic components in the ink are removed to the extent possible, and the metal nanoparticles are fused together to form connections that make the printed features electrically conductive. Sintering has traditionally been done by thermally heating the deposited inks at high temperatures [47]. However, thermal heating limits the usage of thermally sensitive substrate materials, hence novel sintering processes such as laser [48], microwave [49], photonic [50], plasma [51], and chemical sintering [52] have been developed to enable rapid sintering of the nanoparticles without

8

damaging the substrate. However, even accounting for the reduction in sintering time, tremendous care must be taken during drying and curing to avoid defects such as coffee ring, cracking, and/or delamination from the substrate. Elimination of the need for drying and curing could reduce capital costs, manufacturing cycle time, and/or defects that adversely affect conductivity of the printed traces.

In terms of the electrical performance, the electrical resistivity of 2-8 times the bulk metal resistivity [46, 53, 54] that has been achieved using metal-based NP and MOD inks, qualifies the features to be employed in fabrication of numerous flexible electronics devices. However, the ability to achieve bulk metal electrical resistivity would be highly desirable, as it would reduce resistive losses and could enable use in high current applications. Several studies have dedicated their efforts to improve the performance of printed tracks through novel modifications to the nanostructures of conductive materials [34], novel sintering techniques [48], substrate surface modifications [55] etc. Although tremendous progress has been made, there exists a need for inks that can achieve bulk metal conductivity for printed circuitry with little or no post processing.

Significant effort has also been made in printing liquid metals such as alloys of gallium to achieve conductivity for printed flexible/stretchable circuits without the usage of a sintering step. Devices such as RFID tags printed directly onto skin [56] and stretchable electronics [12] - that are not feasible to fabricate using metal-based NP and MOD inks - have been fabricated using the liquid metal inks. However, the low adhesion of these materials to many substrates, easy oxidation and high surface tension, restricts the employment of these materials in fabrication of reliable and stable circuits [12]. Also, alloys of gallium are limited in their applications as they are in liquid state at room temperature and cannot be used without an encapsulation layer around them. They are also not suited for usage in areas that require the devices to operate above room temperature conditions [12]. Electrical resistivity of the alloys is also over 10 times the bulk resistivity of highly conductive metals such as silver and copper, making them less than ideal for employing in several avenues.

Lastly, the cost of nanoparticle metal inks on a weight basis (i.e. $/kg or equivalent) can be 100 times higher than the cost of the same metal in wire or other bulk form [57-59]. Lower raw material costs would

9

contribute to wider adoption of digital printing techniques for printed electronics. Addressing these issues with the current manufacturing approach may boost the adoption of pattern-less digital printing techniques for fabrication of flexible electronics.

The current major challenges in direct writing for printed electronics can be briefly summarized in the following points.

1. **Electrical conductivity**: the electrical resistivity of features printed using the widely employed metal based functional inks is typically about 2-8 times the bulk resistivity of the metal which is used as the raw material in the inks. Fabricating printed features with electrical resistivity closer if not equal to the bulk metal resistivity of highly conductive metals would be highly desirable, as it would reduce resistive losses and could enable use in high current applications.

2. **Post processing**: Metal based inks require post processing after printing through techniques such as drying and sintering to achieve electrical conductivity for the printed features. These post processing steps increase the installation cost, fabrication time and thereby the final product cost. Ideally the functional material would be conductive without the need for an additional sintering process.

3. **Raw material cost**: The cost of the nanoparticle metal inks on a weight basis (i.e. $/kg or equivalent) are typically 100 times higher than the cost of the same metal in wire or other bulk form. Lower raw material costs would contribute to wider adoption of digital printing techniques for printed electronics.

1.4 Motivation

Finding solutions to the three major challenges in terms of low electrical conductivity, the need for post processing, poor substrate adhesion, and high raw material cost mentioned in the previous section may boost the adoption of pattern-less digital printing techniques for fabrication of flexible electronics. To address these issues, we propose the direct deposition of molten metals for fabrication of flexible electronic circuitry. The direct deposition of molten metals could be achieved by exploring a novel direct writing technique referred to here as molten metal jetting (MMJ).

MMJ processes have been developed with the intent of fabricating three-dimensional metal parts (i.e. metal additive manufacturing). MMJ techniques are currently capable of depositing highly conductive bulk metals, such as aluminum, in the form of liquid droplets. The ability to deposit droplets of molten metals has so far been explored for fabrication of complex three-dimensional metal parts. We intend to harness this ability to deposit droplets of highly conductive metals such as aluminum and copper in the fabrication of flexible circuitry. The circuits fabricated using MMJ techniques are expected to have electrical resistivity close if not equal to the bulk metal conductivity of the deposited metal, as the metal only goes through a liquid-to-solid phase change, and there is no fusing of nano particles. As the conductive material being deposited is a bulk metal, successfully fabricating electrical circuits using MMJ processes will eliminate the need for post processing to achieve electrical conductivity. This would lower manufacturing time and thus the production cost. MMJ processes have significantly higher volumetric throughput in comparison to the currently used digital printing techniques and are also scalable for mass manufacturing [60, 61]. Furthermore, the raw material used in MMJ processes is coiled wire whose cost is several orders of magnitude lower than the equivalent weight of nanoparticles [58, 59]

Chapter 2 provides a thorough literature review that concludes that there hasn't yet been any research effort made in investigating droplet jetting of high temperature conductive molten metals (melting point > 250

$^{\circ}$C) such as copper or aluminum onto polymer substrates for fabrication of highly electrically conductive circuits. Understanding the impact of depositing high temperature molten metal droplets on low temperature substrates and developing printing strategies for successfully fabricating high resolution conductive features could enable the usage of these techniques in fabrication of high quality flexible electronic circuits with bulk conductivity that has so far eluded other direct write techniques. Successfully fabricating flexible electronics with these techniques could address the three major challenges (i.e. relatively low conductivity, need for post processing, high raw material cost, and poor substrate adhesion) associated with the DW status quo. This could potentially pave the way for fabrication of highly conductive flexible electronic circuits and usher in various novel flexible electronics appliances for the IoT.

1.5 Research objectives

The aim of this dissertation study is to explore a novel droplet-based metal additive manufacturing process referred as molten metal jetting for fabrication of highly conductive printed electronic circuits. This aim will be achieved by solving the following three objectives:

1. **Objective 1: To determine ideal process parameters for printing uniform printed electronic traces on polymer substrates**- The first objective is to study the impact of various MMJ process conditions on the quality of features printed on flexible substrates. This is intended to provide the process conditions that would be suitable for fabricating high quality metal traces on polymer substrates.

2. **Objective 2: To evaluate the performance of printed features**- The second objective is to evaluate the performance of the printed features in terms of their electrical and mechanical properties to assess the viability of using this process to produce functional electronic circuitry.

3. **<u>Objective 3: To develop a numerical model of the metal droplet impingement process onto polymer substrates</u>** - The third objective is to develop a numerical model to provide a better understanding of the thermodynamic behavior of the polymer substrate with metal droplet impingement. This is important to help understand the jetting conditions under which molten metal drops will bond with, but not burn through, temperature sensitive polymer substrates.

1.6 Summary

The current section has shown the potential of printed electronics in enabling a diverse array of appliances for the IoT in the 4th industrial revolution. Direct write techniques were noted to have high potential to fabricate a diverse array of printed and flexible electronic devices. However, there are some key challenges with the current DW processes, such as the lower electrical conductivity of printed features than the bulk metal used as the raw material, the need for post processing of the printed features through processes such as sintering, poor substrate adhesion, and the high cost of raw materials such as metal nano particles. Addressing these challenges with the current manufacturing approach could boost the adoption of pattern-less digital printing techniques for fabrication of flexible electronics. In this dissertation research, we propose exploring molten metal deposition processes for fabrication of printed electronic features to address the major challenges with the established processes. The dissertation research will be conducted by solving three major objectives. The first is to determine ideal process parameters for printing uniform metal features on polymer substrates. The second is to evaluate the performance of the printed features in terms of their electrical and mechanical properties to assess the viability of using the features as functional electronic circuitry. The third is to develop a numerical model for getting a better understanding of the thermodynamic behavior of the polymer substrate with metal droplet impingement.

Chapter 2. Literature review

Two fundamental aspects govern the ability to successfully fabricate functional electronic circuitry of desired characteristics using printing techniques. They are a) the process capabilities of the printing technique and b) the characteristics of the conductive materials used in these processes. This chapter is aimed at providing an overview of the state of the art in printed electronics processes and the conductive materials that are being used for the fabrication of flexible electronics. We show the capabilities and challenges with the current systems to demonstrate the need to study molten metal deposition for fabrication of flexible electronics.

The chapter is organized as follows. Section 2.1 presents an overview of various electrically conductive printable materials. We show the advancements – in terms of electrical performance, price reduction and post process time reduction – that have been made in developing functional materials, and we discuss the current challenges with them. This is done with the intent to demonstrate how direct printing of bulk metals onto substrates for fabrication of electrically conductive features can address some of the key challenges with the currently used conductive materials.

In Section 2.2 we discuss various direct write technologies utilized for deposition and patterning of printable conductive materials. We show the process capabilities – in terms of minimal attainable feature resolution, compatible materials, and throughput - of the currently used DW processes. We highlight how the proposed molten metal deposition approach can address various challenges with the established DW processes by enabling printing of bulk metals directly onto substrates and thus enabling one step fabrication of highly conductive flexible electronic circuitry. We discuss the progress that's been made so far in developing molten metal jetting (MMJ) techniques for additive manufacturing of three-dimensional parts and highlight the lack of studies in investigating MMJ techniques for printed electronics applications. Taking all of this into account, we demonstrate the need for research, in developing printing strategies for MMJ techniques

to achieve one step fabrication of printed electronics with close to bulk metal conductivities that has so far eluded the current printing techniques and conductive materials.

2.1 Metal-based electrically conductive materials

Electrically conductive materials are a fundamental part of electrical circuitry in all electronic devices. Depositing electrically conductive materials in the form of fluids has been the primary method for fabrication of electronics through printing processes. A diverse array of conductive materials, such as conductive polymers [11], metal nanoparticles [10], metal nanowires [62], carbon nanotubes [63], and low melting point metals [12], have been developed over the last few decades for their usage as electrical conductors in printed flexible electronics. The choice of the conductive material for fabrication of a functional device depends on various physiochemical properties of the material, its compatibility with the deposition technique and the material characteristics of the substrate it's being deposited on.

Various polymer substrates such as polyimide (PI, or Kapton), polyethylene naphthalate (PEN), polyethylene terephthalate (PET), polytetrafluoroethylene (PTFE, or Teflon), among others have long been employed as the underlying substrate material for flexible electronics owing to their excellent material properties that include intrinsic plasticity, hydrophobicity, excellent dielectric and insulating properties, thermal stability, low coefficient of thermal expansion, structural resiliency against repeated forces, and compatibility with roll-to-roll fabrication processes [64].

To have complete process control and achieve repeatability for the printed circuitry, several of the material properties of the conductive materials including viscosity, melting temperature, mean particle size, surface tension, wetting properties, particle size distribution, particle morphology, specific heat, thermal conductivity, density, emissivity, diffusivity, reflectivity, solid loading, substrate material, sintering rate and porosity must be thoroughly considered [60]. Conductive materials are often referred to as inks when

they are deposited using printing technologies. Ideally, the inks used for fabrication of electronic circuits would be cheap, easy to prepare, store, deposit, have high adhesion to flexible substrates and provide high electrical conductivity after deposition, without the need for any post-processing.

The earliest work in the fabrication of conductive patterns using printing techniques was focused on conductive polymers such as polyanilines, polypyrroles, PEDOT etc. [65]. The discovery of conductive polymers was a seminal accomplishment which jumpstarted the modern era of organic conductors and semiconductors, and earned the contributors a Nobel prize [17]. Various advantageous features of conductive polymers, such as their electronic compatibility with organic semiconductors, their low temperature processing, and film forming properties, have facilitated their wide adoption in thin-film devices such as organic light emitting diodes. However, formulation of conductive polymer inks can be challenging and thereby expensive. The base materials used in these inks are usually salts which may be difficult to dissolve in organic solvents. Furthermore, their electrical conductivities are highly dependent on their oxidative state, which is susceptible to degradation by oxygen and atmospheric moisture [65].

It is general knowledge that elemental metals are excellent conductors of electricity. Owing to their high electrical conductivity, extensive research involving formulation of metallic conductive inks for printed electronics has been performed. As most printing systems are limited to use with low temperature solutions, the most obvious approach for obtaining a conducting film is by depositing a powdered form of elemental metals that are either dissolved or suspended in a solution. Metal-based inks, such as metal flake inks, nanoparticle inks, nanowire inks, or metal organic decomposition inks, have since been widely employed in the printed electronics industry due to their various attractive attributes.

Among the metal-based inks, metal flake inks have been one of the most widely used. The high adoption is primarily because of their low cost, owing to their inexpensive ink formulation process. The electrical conductivity of the ink occurs from the physical contact between large metallic flakes. This means the post processing temperature for the inks can be relatively low, as the temperature needs to be only high enough to remove the inks solvent and harden any binder or polymer material to give the film mechanical stability

16

[66, 67]. However, the conductivity of the inks is comparatively higher than sintered NP or MOD inks due to their low contact area between the flakes. This is a significant drawback for using flake inks for electronic device fabrication. Flake inks are not further discussed in detail due to issues with their relatively high electrical resistivity and incompatibility with several printing techniques.

2.1.1 Nanoparticle inks

The metal-based inks that are most widely used for printed electronics are nanoparticle (NP) inks, as they provide reasonably conductive features at relatively low processing temperatures. The relatively low temperature processing conditions are due to the phenomenon known as melting point depression. This means that the melting point of metal nanoparticles is significantly lower than that of the bulk metal. The metallic nanoparticles are suspended in a suitable solvent which could either be aqueous or organic [10]. To obtain highly conductive tracks that are desired in electronics applications, NP inks are typically based on the most electrically conductive metals, such as silver [54] (bulk metal electrical resistivity: 1.59×10^{-8} ohm.m), copper [68] (bulk metal electrical resistivity: 1.68×10^{-8} ohm.m), gold [69] (bulk metal electrical resistivity: 2.44×10^{-8} ohm.m), or aluminum [70] (bulk metal electrical resistivity: 2.65×10^{-8} ohm.m) etc.

Among the most electrically conductive metals, gold currently has a price of over \$1000/ounce and is thereby prohibitively expensive for manufacturing of low-cost electronics. Aluminum has very low reduction potential, which makes it highly reactive with atmospheric oxygen, and hence very hard to handle [70]. Silver, has been the most widely studied metal NP ink, because it is the most electrically conductive element, it has a low oxidation rate, and it has good stability on various substrates [46]. Electrical resistivity of printed features as low as 2-3 times the resistivity of bulk silver has been demonstrated for silver NP inks [54]. However, silver is a precious metal with a price of about \$15/ounce. This is not ideal for achieving inexpensive flexible electronic devices.

17

Copper has attracted wide attention in printing conductive features as it is abundant, cheap ($0.20/ounce) and highly conductive. However, the high reduction potential of copper presents some handling and storage difficulties as its nanoparticles tend to oxidize spontaneously in air [68]. To prevent issues with rapid oxidization, copper nanoparticles encapsulated in an anti-oxidation shell of noble metals such as gold, silver, or platinum have been developed [34]. However, the encapsulation process is an additional ink-synthesis step that results in higher product cost. Despite that, commercially available copper NP inks tend to be significantly cheaper than silver NP inks due to the lower raw material cost. They are therefore very attractive for the industry [71, 72].

A significant challenge for NP inks exists in terms of substrate adhesion. Nanoparticles in the inks do not adhere well to the surface of widely used hydrophobic and inert polymer substrates. Two approaches have been used to improve the adhesion of the printed NP inks: ink modification and substrate conditioning. Additives such as surfactants and binders have been shown to promote ink adhesion to the substrates [55]. Studies have shown that NP inks with modification of the inks to promote adhesion offered excellent adhesion and qualified them to be ranked in the highest category in the ASTM D-3359 standard adhesion test [73, 74]. Conditioning of the substrate surface through either physical (plasma, ultra violet etc.) or chemical (self-assembled monolayers or multilayers) modification has also been shown to be effective in promoting adhesion [55]. However, the tradeoff with use of substrate conditioning is the increase in processing time which makes this approach less attractive for industrial applications.

In terms of the electrical performance of the inks, additives such as humectants, binders, defoamers, dispersants, colloidal stabilizers, rheology, and surface tension modifiers help achieve optimal printing performance of the ink. However, they tend to be electrically non-conductive and thereby detrimentally impact the electrical conductivity of printed circuits. Despite these challenges, electrical resistivity values as low as of 2-3 times the resistivity of bulk metals have been reported for the printed features [68, 75, 76]. The impressive electrical performance of NP inks qualifies them to be employed in fabrication of various functional devices such as flexible organic field effect transistors (OFET) [21], disposable radio frequency

identification (RFID) tags [23], and thin film photovoltaic solar cells [54]. However, achieving electrical resistivity that is closer if not equal to bulk resistivity of the metals can enable the fabrication of several more devices that require high current carrying capabilities such as bus bars, backplanes, radio frequency transistors etc.

In their current state, there are some key limitations associated with NP inks. In most of the cases, NP inks do not possess little or no intrinsic electrical conductivity, as the metal is in the form of a suspension of nanoparticles in non-conductive solvents [47]. Therefore the circuits printed with NP inks require a sintering process at elevated temperatures (100–200 °C) to remove the electrically non-conductive organic components, fuse the nanoparticles, promote grain growth within the printed features and enhance the conductivity [47]. The thermal sintering process typically requires about half an hour to render the precursor compounds conductive. This makes thermal sintering unscalable for roll-to-roll (R2R) production [48]. Also, most of the substrates used in flexible electronics are thermoplastic in nature, so it is crucial that the processing temperature remains below the glass transition temperature (T_g) of the substrate. Higher sintering temperatures might permanently deform the substrate, hence thermal sintering at elevated temperatures restricts the choice of available substrates.

To overcome this issue, novel sintering techniques such as laser [48], microwave [49], photonic [50], plasma [51], and chemical sintering [52] have been developed for making NP inks conductive. They reduce the sintering temperature and time, and thereby enable the usage of various flexible polymer substrates. This also helps enable scalability for R2R production. Accounting for the advancements in reducing the temperature and time to sinter, the post processing of NP inks is nonetheless an additional manufacturing process step that increases the manufacturing time, installation, scope for potential manufacturing errors and manufacturing costs, which is undesirable for mass manufacturing.

NP inks which are capable of achieving higher electrical conductivities via high nanoparticle loading ratios are associated with frequent clogging of print heads and can thereby result in poor print quality when used for extended periods of time [77]. Synthesis of the nanoparticles is also very expensive, resulting in

relatively high cost for purchasing nanoparticles. The current purchasing price of copper nanoparticles is about $56/oz, which is two orders of magnitude higher than the price of bulk copper [78]. Likewise, the purchasing price for silver nanoparticles is about $114/oz, which is about 7 times the price of bulk silver [79]. The high price of purchasing nanoparticles and the additional cost associated with the synthesis of the ink further increases the cost of NP inks. The cost of commercially available NP inks that are compatible with digital printing processes are currently priced at about $60/fl.oz. for copper NP inks [71] and $200/fl.oz. for silver NP inks [72]. This high price point poses a significant barrier for the adoption of NP inks in fabricating inexpensive flexible electronics on an industrial scale.

Despite these issues, NP inks are becoming an attractive choice for fabrication of flexible electronics due to their compatibility with various digital printing techniques. Significant research effort has been devoted to improving the adhesion, electrical performance and reducing the post processing time for NP inks. However, the relatively high cost of the inks in comparison to bulk metals and the need for post processing through sintering tends to increase the manufacturing time and cost. This has so far limited them to prototyping and low volume manufacturing of printed electronics.

2.1.2 Metal-organic decomposition inks

In contrast to the NP inks which are in the form of a suspension, metal-organic decomposition (MOD) inks take the form of metal salts dissolved in organic or aqueous solvents and are promising alternatives to NP inks. As the inks are solutions rather than particulate suspensions, they can help reduce the risk of agglomeration and the consequent nozzle clogging associated with NP inks. The cost of the raw materials and ink processing is also comparatively lower than that of NP inks [80]. The cost of copper salts and silver salts are about $1/gm and $3/gm respectively [81, 82]. This makes them about 25-50% less expensive than the purchasing price of copper or silver nanoparticles [78, 79]. They also tend to have a higher shelf life

than NP inks as they do not require the addition of colloidal stabilizers. Moreover, they do not need a highly controlled environment for storage and usage. They can be printed in layers to get properties that are close to bulk metals.

Several MOD inks have been developed using highly conductive metals such as silver [45] , copper [83], nickel [84] platinum [85], gold [86], aluminum [87] etc. Electrical resistivity values as low as 2 times the theoretical resistivity of bulk metals have been reported for silver [45] and copper [83] MOD inks respectively. Studies have shown that MOD inks offer sufficient adhesion to be ranked in the highest category in the ASTM D-3359 standard adhesion test [88, 89]. Out of the various available metals, the most commonly used metal for MOD inks is silver. Salts of silver are organic silver complexes which can be thermally transformed into silver thin films with resistivities approaching twice that of bulk silver [45]. However, the metal exists in its oxidized form and needs to be reduced to its elemental form to make it electrically conductive. Circuits printed with MOD inks require a thermal curing process at elevated temperatures (>200 °C) to decompose the salts into electrically conductive metal [41]. To enable the usage of low temperature flexible polymer substrates, novel approaches for synthesizing metal salt complex solutions that become electrically conductive at low curing temperatures around 90–110 °C have been proposed [45, 90].

The procedures for synthesis of the organic silver salts which become conductive at low sintering temperatures tend to be quite complicated and require several synthesis steps. To overcome this issue, some researchers have presented single step processes to achieve conductive traces using commercially available silver MOD inks by printing on preheated substrates [91]. However, the preheating is also done at elevated temperatures (>150 °C), which can restrict the usage of inexpensive flexible substrates such as PET. Alternative curing techniques, such as microwave [11], chemical [92], UV irradiation in combination with thermal curing [93], photonic [89, 94], and laser [95] have been investigated. These curing techniques were shown to be effective in reducing the curing temperature and time. Hence, they enable the usage of flexible substrates and simultaneously achieve scalability for R2R production.

Despite the advancements in reducing the process time, the curing process is nonetheless an additional manufacturing step that increases the production time, installation, and manufacturing costs, and is thereby undesirable for high volume manufacturing. Another problem that has been observed for printing of MOD inks is that the deposited features can display a morphological phenomenon commonly called as 'coffee ring' [45]. Droplets and tracks that show this phenomenon have a significant concentration of solute at their edges. In extreme cases, no material remains in the center. The inks being in the form of solutions are also susceptible to motion during the printing and the subsequent curing process. This often leads to loss in the feature definition of the tracks and can greatly affect the reproducibility of the printed elements. The shape boundary instability problems tend to be especially severe on hydrophobic substrates with small contact angle hysteresis [77]. Pretreatment processes such as plasma or chemical polishing can be used before the printing process to ensure both wettability and homogeneity of surfaces. Even with proper surface modification, the intrinsic fluid mechanical instability can lead to print quality deterioration thereby necessitating ink solvent adjustments to eliminate the ink-substrate incompatibility.

The addition of various solvents to enable optimal ink deposition and adhesion can also have a detrimental impact on the electrical conductivity of the deposited materials. However, even with these limitations, electrical resistivities in the range of 2-3 times the theoretical resistivity of bulk metals has been reported for MOD inks [45, 83]. The impressive electrical performance and excellent adhesion of the MOD inks to polymer substrates qualifies them to be employed in fabrication of various printed electronic devices such as flexible displays [83], photovoltaic cells [96], RFID [97] etc.

It can be summarized that MOD inks are an attractive alternative to NP inks for printed electronics because of their desirable electrical conductivity, excellent adhesion, relatively lower cost, and compatibility with various digital printing techniques. Significant research effort has been made in reducing the thermal sintering temperature and time to enable the usage of low-cost polymer substrates. However, the shape boundary instability problems associated with the inks necessitate pretreatment processes such as plasma or chemical polishing, which increases the manufacturing cost. The inks also require post processing

through curing to achieve electrical conductivity. This is less than ideal for high volume manufacturing, and there is currently a need for research effort in developing MOD inks that are inexpensive to synthesize, and which achieve stable metallic tracks with bulk conductivities without the need for pre/post processing.

2.1.3 Liquid metal inks

Liquid metal inks are newly emerging category of conductive inks that are in liquid phase at room temperature. As mentioned in the previous sections of this chapter, NP and MOD based conductive inks do not have intrinsic electrical conductivity and need special post-processing steps such as sintering or curing to remove solvents from the inks and achieve conductive capacity. Liquid metal inks on the other hand are intrinsically conductive without the need for post processing.

Although the metals are in liquid state at room temperature, the inks form a protective oxide layer instantaneously after deposition due to the exposure to atmospheric oxygen. The oxide layer provides stability to the liquid ink and helps in retaining its features. The protective oxide layer can be cracked when the printed tracks are bent or stretched, however, the newly exposed liquid metal reacts with the atmospheric air and instantaneously forms a new oxide layer. This endows a kind of self-healing property to the inks which makes them very attractive not only for flexible electronics but also in stretchable electronics [98]. The inks are also non-hazardous and bio compatible. This has led them to be employed in novel applications where NP & MOD inks are unsuitable, such as printing RFID tags directly onto skin [56] and in fabrication of wearable stretchable electronics [12].

Alloys of gallium such as EGaIn (75.5% gallium and 24.5% indium by weight) and galinstan (62.5% gallium, 21.5% indium and 16% tin by weight.) have been the most widely investigated liquid metal inks [12, 56, 98] . The low melting points of these metals (~30 ℃) allows the fabrication of electrically

conductive features on flexible substrates at room temperature without the need for sintering. Electrical resistivity in the range of $13.6 - 29.5 \times 10^{-8}$ ohm.m have been reported for these inks [12].

However, there are some significant challenges associated with liquid metal inks in terms of their performance. The inks tend to have high surface tension which results in low adhesion to several substrates and thereby restricts the choice of commercially available flexible substrates. Also, the oxide layer doesn't offer complete protection in all the bending scenarios and can lead to leakage of the liquid ink and the failure of printed circuitry. Hence the printed tracks are almost always encapsulated beneath a polymer layer such as polydimethylsiloxane (PDMS) to preserve the shape of printed features [12]. However, the encapsulation process is an additional post processing step that increases the production cost and time.

Some of the best reported values of electrical resistivity for these inks are in the range of $13.6 - 29.5 \times 10^{-8}$ ohm.m. These resistivity values are about 10 times higher than the bulk resistivity of highly conductive metals such as silver and copper which are in the range of $1.59 - 1.68 \times 10^{-8}$ ohm.m. The inks also tend to be relatively expensive for high volume manufacturing, as the purchasing cost of liquid metals is about \$2/gm [99].

Hence it can be summarized that liquid metal inks offer tremendous novel opportunities in fabrication of flexible and stretchable electronics that are not feasible with NP and MOD inks. Studies have shown that liquid metal inks provide good enough electrical conductivity and substrate wetting to qualify them for various printed electronics applications. However, there are some key limitations associated with them, such as the requirement of post processing encapsulation step, poor wetting with some substrates due to high surface tension, and significantly higher electrical resistivity than other widely used metals. There is currently a research need to improve the electrical conductivity, eliminate post processing, and increase the ink stability/adhesion of liquid metal inks so that they can be employed in a wider number of applications.

2.1.4 Summary: Metal based electrically conductive materials

In summary, there has been significant progress made over the past few years in developing metal-based conductive inks for printed electronics applications. Following extensive experimentation and optimization, the electrical and adhesive performance of the inks can be employed in fabrication of some functional flexible devices. However, there are three major challenges with all of the currently available metal-based conductive inks. Firstly, the electrical resistivity of the inks for NP and MOD inks is typically 2-8 times that of the functional metal used in them. In case of the electrical resistivity of liquid metal inks, it is about 10 times that of the highly conductive bulk metals such as copper. Although this electrical conductivity performance is good enough to be employed in various printed electronics applications, achieving bulk metal conductivities would enable fabrication a wider array of novel functional devices. Secondly, all the metal-based inks require post processing (sintering/curing/encapsulation) to achieve the final product. This increases the production cost and time, which is not desirable for high volume manufacturing. The third major limitation is that the cost of the inks tends to be orders of magnitude higher than the cost of the bulk metal, and this in turn drives up the fabrication cost of final product.

Ideally, the conductive ink would be cheap, easy to prepare, store, deposit, and provide high conductivity after deposition without the need for post-processing. A very efficient way of fabricating highly conductive features without the need for postprocessing would be to deposit bulk metals directly onto the substrates. Although, alloys of gallium have been directly printed successfully to achieve flexible and stretchable electronics, they are very limited in the scope of their applications due to their room temperature melting point and low adhesion to several substrates.

Successfully melting and depositing highly conductive metals on flexible substrates can address all three challenges with the current metal-based inks. As depositing bulk metals does not require synthesis of nanoparticles, the cost of raw materials would be significantly cheaper. As the metal is in its bulk state, it would be inherently electrically conductive and would not need post processing to achieve conductivity.

The conductivity of the deposited metal would also be theoretically very close if not equal to the bulk conductivity of the metal. Table 2.1 shows the key characteristics of the metal-based inks (e.g. electrical resistivity, raw material cost, post processing), and puts them in perspective with bulk copper.

Table 2.1 Key features of various metal based conductive materials.

Type	Electrical resistivity	Cost of the conductive raw materials	Post processing
NP inks	2-3 times of bulk copper	$2-4/gm	Sintering
MOD inks	1.5-2 times of bulk copper	$1-3/gm	Curing
Liquid metal eGaIn	8-17 times of bulk copper	$2-3/gm	Encapsulation
Bulk metal	Same as bulk copper	$0.2/gm	No postprocessing

We have noted from our literature review that there haven't been any reported studies that have investigated the deposition of highly conductive bulk metals (silver, copper, gold, aluminum etc.) directly onto temperature sensitive flexible substrates using printing techniques for fabrication of electrical circuitry. This can be attributed primarily to the limitations in the capabilities of available digital printing techniques in handling high temperature molten metals. Also foreseeable are various challenges associated with depositing high temperature molten metals on temperature sensitive polymer substrates.

The newly emerging molten metal jetting (MMJ) techniques that were originally envisioned for use as metal additive manufacturing techniques offer the possibility of jetting high temperature molten metals for printed electronics applications. The next section provides an overview of various digital printing technologies utilized for deposition and patterning of the printable conductive materials, and it demonstrates how MMJ techniques can be employed in depositing highly conductive bulk metals directly onto flexible substrates. This would potentially enable one step fabrication of high performance inexpensive flexible electronic circuitry.

2.2 Direct writing techniques

Over the last four decades, a wide variety of printing techniques have been developed to print functional materials for the fabrication of electronic circuitry. Based on the way in which the material is deposited onto a substrate, printing processes can be broadly classified as "contact" and "non-contact" printing. There are tradeoffs associated with each type of process, and they are to be considered while choosing a printing process for any specific device. Figure 2.1 shows some examples of each of the printing approaches.
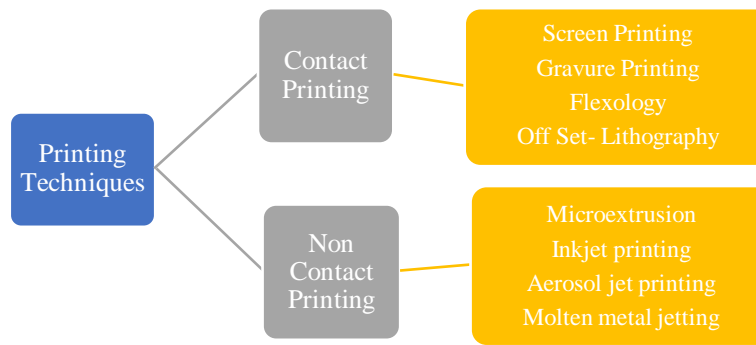
Figure 2.1 Classification of printing techniques based on the type of deposition.

Contact printing processes were the first printing techniques to be employed in printing of electronic circuits [16]. As their name suggests, "contact" printing processes such as flexography, gravure printing and offset lithography need physical contact between the materials being deposited and the underlying substrate on which the material is deposited. They are efficient analog processes that can achieve high throughputs (~10 m^2/s) and lateral feature resolution as small as 10 μm [4]. The high throughput, scalability, and the ability to achieve fine resolution makes them very well suited for high volume printing. However, the contact between the functional materials and the substrate can damage fragile substrates. Furthermore, most contact printing processes are not suitable for conformal (non-planar) printing.

The limitations associated with contact printing processes propelled research efforts involving non-contact printing process for fabrication of electronic circuits. Unlike the contact printing process, non-contact printing techniques do not use master patterns and are capable of depositing conductive materials to form desired patterns directly from digital image files. Some of these processes are also referred as direct write (DW) techniques, as the material is deposited directly onto the substrate instead of having an intermediary device onto which the ink is transferred before it is deposited onto a substrate. As the direct writing processes enable complete digital control of material deposition, they are also referred to as digital printing techniques. DW techniques do not employ fixed master patterns, hence the cost and additional time associated with changeover and replacement of master patterns is also eliminated. The major limitation with these techniques are that they have a significantly lower throughput ($\sim$0.01 m^2/s) in comparison to the throughput ($\sim$1 m^2/s) of contact printing processes [4].

An ideal printing process for fabrication of electronic devices would be digitally controllable, fully additive, functional in atmospheric conditions, high throughput, scalable, non-contact, low-temperature, and can print highly conductive materials at a high resolution. Both contact and non-contact printing processes still lack some of the attributes desired in an ideal printing process. Although contact printing provides significantly higher throughput, most of the recent research in printed electronics technology has been focused on non-contact DW processes primarily because of the greater control over feature position, ability to iterate designs much more rapidly, and excellent layer registration.

DW covers several processes that employ radically different methods for material transfer onto the desired substrate. DW processes can be classified as droplet-based and flow-based depending on the mechanism of materials transfer [60]. As their name suggests droplet-based printing techniques deposit droplets of the functional materials whereas the flow-based deposition techniques deposit the material in the form of a flow. Figure 2.2 shows the classification and some examples of each of the two DW approaches.
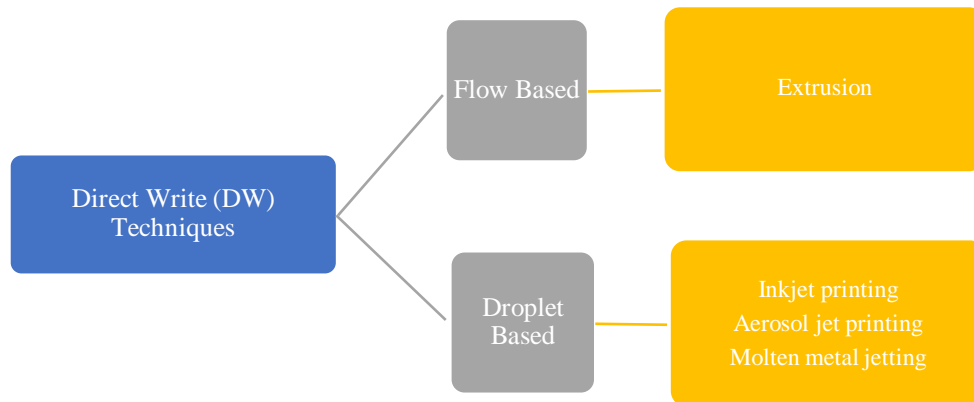
Figure 2.2: Classification of Direct writing techniques.

This research is focused on investigating the feasibility of employing a droplet based DW technique referred to as molten metal jetting (MMJ) system, for deposition of molten metals directly onto flexible substrates to fabricate high-performance flexible electronics. MMJ techniques offer most of the attributes desired in an ideal printing process for fabrication of electrical circuitry. This section provides the background information on the most widely employed digital printing techniques, including aerosol-based printing, micro extrusion, and inkjet printing. It puts them in perspective with MMJ techniques to demonstrate how this process could address several of the shortcomings with the established DW techniques and enable one step fabrication of inexpensive high performance flexible electronic devices. The lack of studies in investigating MMJ techniques in fabrication of electronics is highlighted to illustrate the need for research in this area.

2.2.1 Micro-extrusion

Micro-extrusion is a flow based direct write approach that is favored for dispensing heavily loaded inks. This process is capable of depositing highly viscous materials up to 5,000 Pa.s [100]. The delivery of material for micro extrusion systems is continuous as opposed to processes involving jetting of discrete drops. Usually, the delivery of the flowable material is through a very small orifice or a needle. The illustration in Figure 2.3 shows a cross-sectional view of a commercially available micro-extrusion system manufactured by nScrypt, Inc. The ink is stored in a reservoir, typically a syringe, and pneumatic or screw actuated pressure is applied to the plunger to push the ink out of the reservoir. The flow of material is controlled through a smart valve. The use of higher viscosity pastes allows for fabrication of thick films.
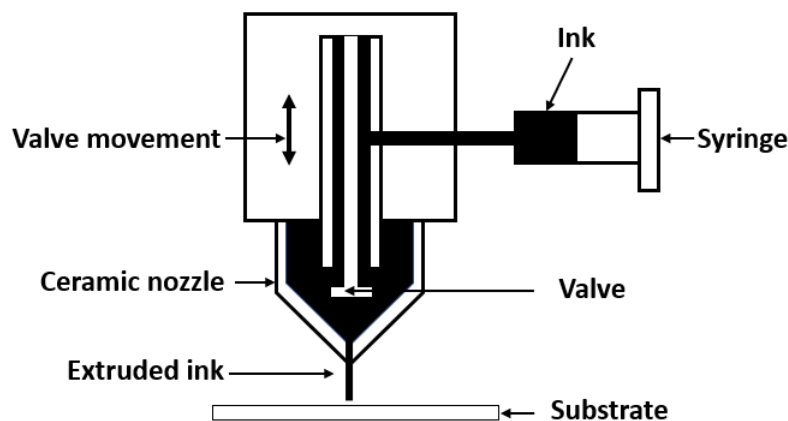
Figure 2.3: Schematic diagram of micro-extrusion process. Adapted from [100].

Inks with metal loadings in the 60-70% range can be deposited using this process [100]. This enables fabrication of circuitry with relatively higher conductivity. Line widths as small as 25 μm have been produced using this technique, although this value increases with the usage of higher particle loaded inks [43]. Depending on the line width of the printed tracks, the resolution tolerance varies from ±3% to ±5%, which is better than some droplet based digital printing techniques [60]. This technique is capable of

printing on highly conformal surfaces with the aid of laser-based height sensors [101]. The technique also enables the usage of multiple ink reservoirs to mix different materials before printing. Linear writing speeds are typically about 50 mm/s, however they can reach as high as 300 mm/s [60]. Volumetric deposition rates depend on nozzle size, which is in turn limited by the material selection. Various components such as solid oxide fuel cell materials, antennas, and strain gauges [102] have been fabricated using this process.

2.2.1 Aerosol deposition

Aerosol deposition is a droplet based direct write process that is very well suited for deposition of low viscosity inks in the range of 1-2500 cP [42]. In this process, the functional ink is placed in an atomizer, creating a dense aerosol of micro-droplets from 20 nm – 5 μm in diameter [60]. Depending on the properties of the ink, either an ultrasonic or pneumatic atomizer can be used. Low viscosity inks (0.7-30 cP) which contain small particles (<50 nm) can be ultrasonically atomized. Pneumatic atomizer can be employed for inks with higher viscosity (<2500 cP). A schematic illustration of a commercially available pneumatic aerosol-based deposition system manufactured by Optomec, Inc is provided in Figure 2.4 to explain the working of a typical aerosol-based deposition process. The system can be divided into three steps, wherein the functional material is atomized in the first step. In the second step, the aerosol is transported to the deposition head by an inert carrier gas flow. Finally, the aerosol stream is aerodynamically focused using a flow of sheath gas. The collimated aerosol is then deposited on the desired substrate.
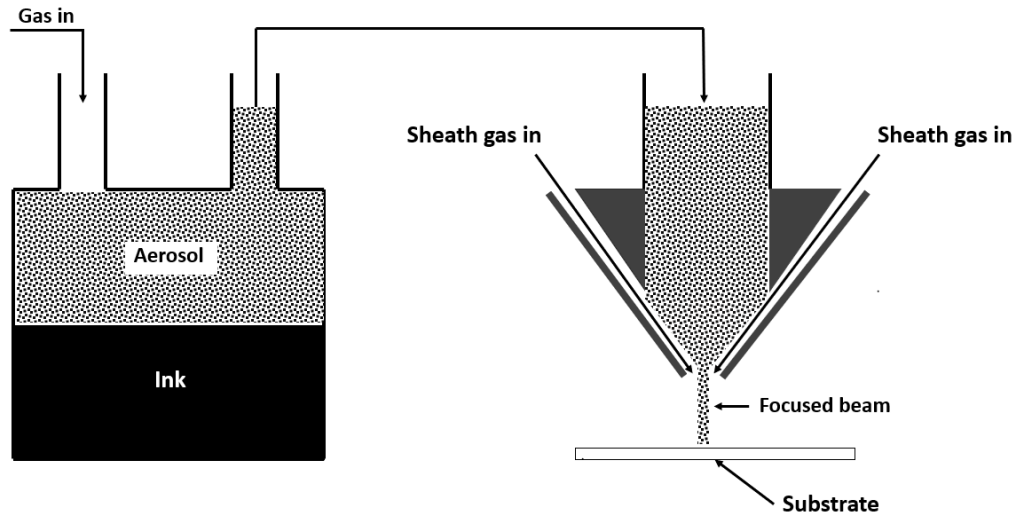
Figure 2.4: Schematic of the Optomec Aerosol-jet printing process. Adapted from [42].

Films of thickness in the range from 100's of nanometers to 10's of microns and lateral feature resolution as small as 10 μm have been achieved using this technique [42]. The process is also capable of printing on planar as well as non-planar substrates making it suitable for conformal patterning. The process is well suited for applications that require low film thickness such as thin film transistors, solar cells, printed antennae, etc. [42]. Writing speeds as high as 200 mm/s and corresponding volumetric deposition rates of up to 0.25 mm^3/s with a single nozzle can be achieved using this technique [60]. However, the throughput capability of single nozzle aerosol printing is not ideal for high volume manufacturing (millions of parts per annum). The process is well suited for rapid prototyping of electronics in the product development phase and in low volume manufacturing. Development of multiple nozzle deposition systems is one way of improving process scalability.

2.2.3 Inkjet printing

Inkjet printing is a droplet-based printing technique and is the most mature among the DW techniques for fabrication of flexible electronics. Lord Rayleigh published in 1878 that a stream of inviscid liquid can be broken into stream of individual droplets by the application of a transient pressure to the nozzle [41]. This fundamental behavior of liquids is keystone on which several types of inkjet printing techniques have been developed. The earliest version of inkjet printers appeared in the mid-1970s and quickly became very popular in the context of small office and home applications [60].

The technology was introduced in an industrial context for in-line date coding and marking of products. Inkjet printers have since been modified to deposit functional materials onto desired substrates and thereby fabricate electronic circuitry [103]. The process of inkjet printing can be broadly classified into two types based on the way in which droplets are deposited onto the substrate - continuous inkjet (CIJ) and drop-on-demand inkjet (DOD). The continuous mode can be further subdivided into binary deflection, multiple deflection, hertz, microdot, etc. DOD inkjet process can be predominantly classified as thermal and piezoelectric printing based on the type of ejection.

As illustrated in Figure 2.5, CIJ involves continuously jetting the conductive ink through a single nozzle due to application of pressure. An electrical charge is applied to individual droplets while the droplets are forming. The charge remains on the individual drops, and the droplets can be deflected towards a specific location on the substrate based on the level of charge in them. The uncharged droplets are deflected to an ink collection and recirculation system [104].
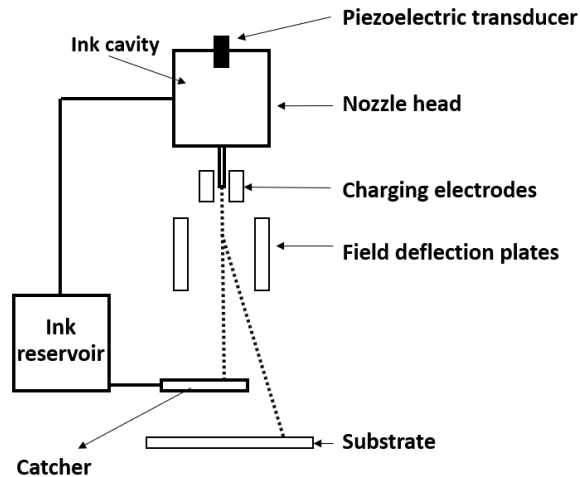
Figure 2.5: Schematic illustration of continuous inkjet printing. Adapted from [60].

DOD involves jetting of ink droplets in a precisely controlled manor. Drops of ink are only ejected from the system when they are required to be deposited on the substrate. Hence the need for recycling the unused ink is eliminated. DOD processes are also of significantly lower complexity than CIJ, as they do not require droplet charging, deflection and ink recirculation [41]. In comparison to micro-extrusion systems, the drop-by-drop control for the DOD systems allows for more discrete placement of material.

In thermal DOD inkjet printing, a resistive heater, as illustrated in Figure 2.6, is used to heat the ink. The heating of the ink results in the formation of vapor bubbles that subsequently lead to the ejection of droplets though a nozzle [104]. However, the thermal cycling associated with this process can lead to ink degradation and loss of some desired functional properties in the ink [41]. This places significant restriction on the materials which can be jetted using this process. The creation of vapor bubbles can sometimes lead to the formation of a layer of solidified ink over the resistive heater, thereby detrimentally affect the performance of the printer over time [41].
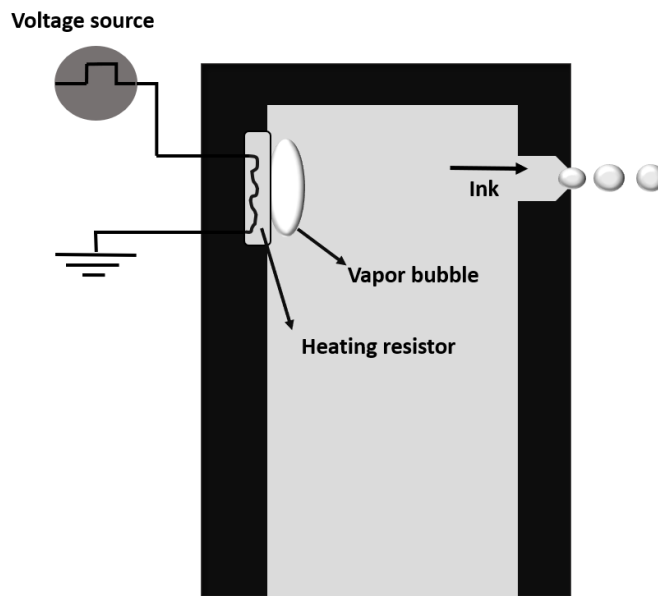
Figure 2.6: Schematic illustration of thermal inkjet printing. Adapted from [41].

Most of the inkjet printing of functional materials to date has been done using piezoelectric DOD systems. In this technique, a piezoelectric electrode, as illustrated in Figure 2.7, is used to eject the ink by application of voltage to a piezoelectric membrane that deforms and ejects ink out of the nozzle. It is a precise process which allows complete control over the amount and rate of droplet ejection through the manipulation of magnitude and frequency of the pulse voltage. A broad range of water-based or solvent-based functional inks can be deposited using this technique. Studies have shown that lateral feature resolution as small as 20 μm can be achieved using this process. This makes it a very attractive choice for fabricating printed electronics components [41]. In terms of throughput, the volumetric dispensing rate of a single nozzle is about 0.3 mm^3/s [60]. However, this can be increased by using an array of nozzles. DOD inkjet printing has been extensively used to print NP inks [46, 53, 54, 105] and MOD inks [45, 85, 96]. Numerous devices such as photovoltaic cells [96], organic light emitting devices [106], thin-film transistors [107] and integrated circuits [108] have been fabricated using DOD inkjet printing techniques.

35
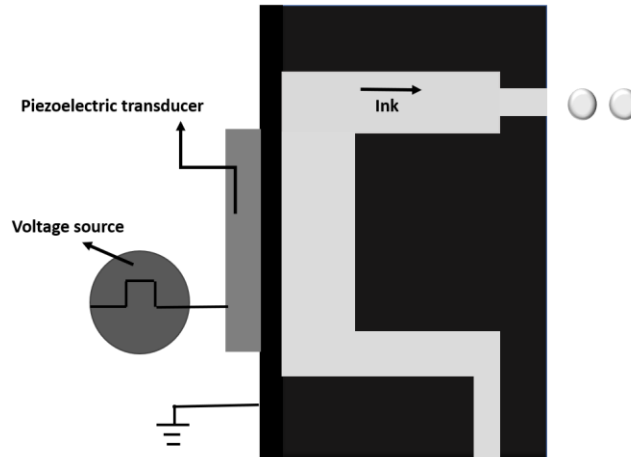
Figure 2.7: Schematic illustration of Piezoelectric Inkjet printing process. Adapted from [41].

There can be a range of challenges associated with using piezo electric DOD inkjet printing in the deposition of functional materials. These issues can arise in areas related to ink formulation, printing processes parameters, surface characteristics of the substrate, rate of solvent evaporation, etc. As this is a drop-by-drop deposition technique, it is subject to pixilation-related problems. The printed patterns can sometimes vary considerably, thus affecting the repeatability of the process. This is due to the complicated drying phenomena known as the "coffee ring" effect previously discussed. There are also some key challenges associated with the deposition of droplets, such as issues related to droplet flight path, impact location on the substrate, droplet velocity, and droplet size [109]. Despite its very promising results on the laboratory scale, the relatively low throughput (in comparison to contact printing processes) and relatively low pattern resolution (in comparison to photolithography) are some major challenges for the process in becoming an industrial scale production technique for printed electronics.

2.2.4 Molten metal jetting

Molten metal jetting (MMJ) is a novel and exciting metal additive manufacturing technology that is being explored to address challenges associated with the widely used powder-based metal additive manufacturing processes. The operating principle behind the technology is analogous to conventional DOD ink-jet printing, but with the unique ability to deposit droplets of high temperature molten metals instead of nanoparticle or MOD inks. In this process, the molten metal is held in a crucible, and the droplets are ejected from a nozzle via the application of an electrical pulse.

Over the last couple of decades, several techniques capable of dispensing individually controlled molten metal droplets at precise locations have been developed [61, 110, 111]. The ability to precisely control the droplet stream enables the fabrication of 3D objects in a highly reproducible manner from digitally stored computer-aided design (CAD) data. In comparison to the established powder-based metal additive manufacturing technologies, this approach has a number of attractive advantages. It uses relatively inexpensive wire rather than powder as the feedstock material. This lowers cost, yet it is also much safer to work with. There is no powder bed, hence the need to recycle and mix lots of powder is also eliminated [61].

The field of MMJ began with the development of low temperature solder jetting by IBM corporation in 1972 for fabrication of solder bumps in the electronics industry [112]. One of the earliest patents for the technology was obtained by Heiber in solder jetting for Philips North American in 1989 [113]. Their deposition system is based on a lead zirconium titanite (PZT) piezo-electric crystal for the generation of the droplet stream. However, this limited the technique to use with low melting point metals (melting point < 175 °C) such as low temperature solder [112]. With improvements in product design and development of new PZT materials that can operate at higher temperatures, the jetting of metals with slightly higher melting points (melting point < 250 °C) such as 63/37 solder became possible [112]. The late 1980's and the early

1990's saw a significant rise in the scientific studies related to solder jetting research for its applications in the electronics industry [114-117].

The inherent benefits in solder droplet deposition processes, such as the high throughput, material recycling capabilities and low operational costs, propelled research utilizing these techniques in fabrication of 3D components [110, 118]. The research started with development of droplet generators capable of generating droplet streams of low temperature materials such as wax, tin and solder with minimal deviation in the droplet size [118] and droplet stream trajectories [110]. The early research was focused on low temperature metals, and employed continuous inkjet (CIJ) style deposition systems wherein the molten metal droplets ejected from a nozzle were electro-statically charged and subsequently deflected onto desired locations on the substrate [111].

The research then progressed into development of systems capable of depositing intermediate temperature (melting point > 250 °C) metals. The first demonstration of depositing high temperature metal droplets was performed by Orme *et al.*, wherein molten aluminum was deposited with a deposition rate as high as 24,000 droplets/sec using CIJ style deposition [111]. However, the continuous stream of droplets generated by the CIJ style devices cannot be rapidly turned on and off. Consequently, droplet deposition on the substrate must be interrupted to divert the metal droplet stream into a catch reservoir, resulting in significant raw material waste. The limitations with the CIJ style systems prompted the research to move into the development of drop-on-demand (DOD) metal droplet printing techniques.

DOD systems as described in the inkjet printing section are systems that are capable of depositing droplets on demand at desired locations. As they do not generate droplets in a continuous stream, they reduce the material waste associated with CIJ systems. Several patents filed since the early 2000's have shown the development of ejection techniques capable of depositing metal droplets using the DOD technique [119-126]. Various types of droplet ejection mechanisms such as pneumatic, piezo electric and magneto hydrodynamic (MHD) have been explored. A patent by Chandra and Jivraj discusses a pneumatic drop-on-

demand process for depositing molten metals wherein the generation of a pressure oscillation in the molten metal chamber results in droplet ejection through an orifice [126].

Among the different types of ejection mechanisms explored for DOD molten metal jetting, magneto hydrodynamic (MHD) molten metal jetting was found to be promising. A patent by Sackinger et al. in 2001, demonstrates an apparatus that can jet molten metal droplets on demand [123]. They have employed the MHD principle for ejection of molten droplets as piezoelectric crystals suffer depolarization at elevated temperatures, resulting in decreased performance. A 2012 publication by Suter *et al.* shows the development of a functional drop-on demand metal droplet generator using the operating principle of MHD [121]. Their print head had no moving parts and was capable of ejecting droplets of molten tin. Although they were able to show successful formation and ejection of high temperature metal droplets from the print head, their system was occasionally susceptible to sparks in the metal chamber. Also, the liquid tin in the print head behaved dramatically different with age due to the formation of oxide layers and led to chaotic droplet generation over time.

A 2016 publication by Mircea *et al.* shows a DOD droplet generator for metal compositions comprising of a metal and silicon [127]. The silicon in the composition was added to prevent the contaminants present in the composition from precipitating and thereby clogging the nozzle orifice. Berkhout *et al.* developed a device with a replaceable graphite fluid chamber body to make the process of printing high temperature metals easier [119]. Patent applications in 2017 by Sachs *et al.* [120] and Vader *et al.* [125] shows the development of metal DOD deposition systems using the principle of MHD for manufacturing of 3D components. The patent by Vader *et al.* served as the foundation for research and development which eventually led to a commercially available metal droplet printer marketed under the name ElemX by Xerox™ Inc.

MMJ systems have been developed as metal additive manufacturing machines that can fabricate three-dimensional metal parts. In this research, the novel idea of using an MMJ process to fabricate high-performance electronic components on low temperature flexible substrates is explored. A patent by Ohashi

et al. from 2006 shows the idea of using molten metal droplets for producing electric circuitry [128]. They demonstrate the idea of employing MMJ systems for printing electric conductor circuits for bus bars, electric wires, etc. However, no further investigations have been made to fabricate functional features using MMJ techniques and evaluate the performance of the features fabricated using this approach.

The literature survey provided in this section suggests that nearly all of the research in printed electronics materials has been focused on NP inks, MOD inks and low temperature metal alloys. It can be noted that there hasn't yet been any significant effort made in deposition of highly conductive molten metals for fabrication of electronic circuitry. In terms of the raw material cost, the cost of aluminum feed wire used in this research is orders of magnitude lower than the cost of NP and MOD infeed materials [129]. This translates into very significant cost savings for industrial usage. The high throughput of the MMJ systems in comparison to other digital printing techniques also makes them highly attractive for high volume production. As the metal is in its bulk state, there would also be no need for post processing such as sintering, which would drive the cost and manufacturing time further down. Employing the commercially available MMJ deposition processes in printing flexible electronics could result in one step fabrication of circuitry with bulk conductivity that has so far eluded the established DW processes. Even though depositing a high temperature metal droplet on a temperature sensitive substrate without damaging it can be challenging, the potential advantages of this technique eclipse the challenges associated with it.

2.2.5 Summary: Direct write techniques

This section has shown the capabilities and challenges associated with direct write techniques being employed for printed electronics. DW techniques have enabled the fabrication of flexible electronics that are very difficult and expensive to produce via conventional manufacturing techniques. Table 2.2 summarizes the key functional characteristics of the widely employed direct write processes. However, the

established DW processes currently have some challenges associated with them and addressing these challenges could enable fabrication of printed electronics at a lower cost, thus allowing them to be used in novel applications.

Table 2.2: Summary of direct write process characteristics [60, 61].

Printing technique	Line width (L_w) or droplet diameter (D_d)	Deposition rate or writing speed	Compatible metal-based inks	Feed stock material cost
Aerosol based deposition	L_w from 5µm to 5mm D_d from 20nm to 5µm	0.25 mm^3/s with a single nozzle	NP and MOD inks that can be atomized	$1-4/gm
Micro extrusion	L_w from 25µm to 3mm	Max v_w is 300 mm/s, Typical v_w is 50 mm/s	NP, MOD, and liquid metal inks with viscosity up to up to 5,000 p	$1-4/gm
Continuous inkjet printing	L_w from 20µm to > 5mm D_d from 10µm to 150µm	Up to 60 mm^3/s with a single nozzle	NP and MOD inks with viscosity of 2-10 cp	$1-4/gm
DOD inkjet printing	L_w from 20µm to > 5mm D_d from 10µm to 150µm	Up to 0.3 mm^3/s with a single nozzle	NP and MOD inks with viscosity of 10-100 cp	$1-4/gm
Metal droplet deposition	L_w from 250µm to 600µm D_d from 250µm to 600µm	Up to 150 mm^3/s with a single nozzle	Bulk metals	$0.03/gm

Direct deposition of molten metals could potentially address several challenges associated with the established DW techniques. The printed circuits would potentially have bulk metal conductivity without the need for post processing, at a significantly higher throughput. We have noted that MMJ systems that are capable of depositing molten metal droplets, have only been employed so far in 3D printing applications. No effort has yet been made in using them for printing flexible electronic devices. Studying the impact of depositing high temperature molten metal droplets on polymer substrates and development of printing strategies in fabrication of functional electrical circuits could enable the high-volume manufacturing of high-performance flexible electronics in a single manufacturing step.

Chapter 3. Approach

3.1 Problem statement

The literature review presented in the previous chapter has revealed the challenges with established direct write techniques and the conductive materials employed in these systems for fabrication of flexible electronics. The three major current challenges were identified as (1) the high cost of the raw materials and their synthesis for metal-based inks, (2) the need for post processing of the inks and (3) the relatively high electrical resistivity of the printed features. Direct deposition of molten metals has the potential to address these three major issues. Molten metal jetting techniques developed for additive manufacturing of metal structures are capable of precisely depositing droplets onto desired locations on a platform. Studying the process of depositing high temperature molten metal droplets on polymer substrates and optimizing the printing conditions could enable the high-volume manufacturing of highly conductive flexible electronic circuitry in a single manufacturing step.

To perform our experiments, we have chosen to employ a commercially available molten metal deposition system manufactured by Xerox™ Inc. Solving the three major objectives mentioned in section 1.5 would help us in studying the viability of depositing molten metals on flexible substrates for fabrication of flexible electronics. Objective 1 will be achieved through studying the impact of key process conditions of MMJ printing for achieving high resolution features. Objective 2 will be achieved through characterization of the electrical and flexibility properties of the printed features. Objective 3 will be achieved by developing a numerical model using ANSYS numerical analysis software. The following subsections will discuss the methods and materials used for achieving the objectives in detail.

3.2 Magneto hydrodynamic molten metal jet printing

In this work, we have employed a molten metal jet metal additive manufacturing technique based on magneto hydrodynamic (MHD) droplet ejection. This technology is currently being developed by Xerox ™ Inc. In this process, a spooled solid wire (~1 mm diameter) of aluminum alloy 4043 is fed into a ceramic heating chamber where the wire is melted to form about 3 ml of liquid metal. The heating chamber is surrounded by a coil and terminates with a nozzle having a submillimeter diameter orifice. The generation of electrical pulses in the coil produces a transient magnetic field (B) that permeates the molten metal and induces a closed loop transient electric field (E) within it, according to the Maxwell-Faraday equation. This in turn causes circulating eddy currents (J) within the liquid metal as described by Lenz's law. The applied (B) field interacts with the circulating current density (J) and creates a magnetohydrodynamic Lorentz force density (f_{MHD}) within the chamber. A pressure (P) created from the radial component of f_{MHD}, acts to eject a liquid metal droplet from the orifice. . Figure 3.1 provides a schematic illustration of the MHD molten metal jetting process.

When nozzles having different orifice diameters are used, the size of the ejected droplets will change. Droplets are ejected with a velocity of ~1-10 m/s onto an underlying platform. Drop velocity is affected by rheological properties of the molten metal as well as the pulse voltage and pulse length [61]. The platform can translate in the X and Y directions, whereas the printhead can translate in the Z direction. The motion of the print head and the platform can be controlled through G-code, and the droplets can be precisely deposited at any location on the underlying platform through the translation of the platform and the print head. The underlying platform can be heated to enable better adhesion of the deposited metal onto the platform. 3D metal objects of arbitrary shapes and complex geometries can be built by the deposition of droplets in layer-by-layer fashion on the moving platform.
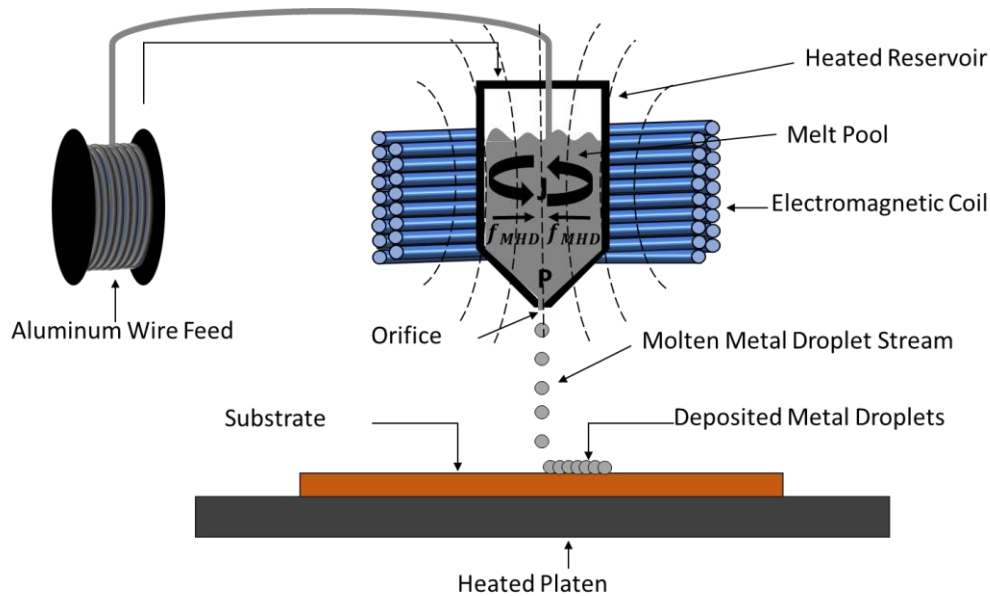
Figure 3.1: Cross sectional view of print head and print process overview.

The quality of the parts fabricated using the magnetojet printing process depends on various user-controlled input parameters fed into the system. The user controllable parameters of the magnetojet system are as follows.

1. **Orifice size** – The diameter of the orifice opening in µm. This affects the size of the ejected droplet and thereby the size of the deposited track.

2. **Droplet temperature** – The temperature of the molten metal in the print head in degrees Celsius. This affects the material properties of the metal such as viscosity and surface tension, and thereby the size of the ejected droplet.

3. **Platform temperature** – The temperature of the platform onto which the ejected droplet lands, in degrees Celsius. This could affect the adhesion of the impinging droplet onto the platform.

4. **Pulse length** -The duration of the electrical pulse that results in the droplet ejection in µs. This affects the velocity of the ejecting droplet, and it has a modest effect on drop volume.

5. **Pulse voltage** – The voltage of the electrical pulse that results in the droplet ejection in Volts. This affects the velocity of the ejecting droplet.

6. **Pulse frequency** – The number of pulses generated per second in Hz. This affects the solidification behavior of the deposited droplets and thereby the quality of printed features.

7. **Standoff distance** – The distance between the outer tip of the orifice and the upper surface of the underlying material. This affects the solidification of the ejected droplets and the stability of the droplet stream.

8. **Droplet overlap fraction** - The amount of overlap between adjacent droplets that are deposited. This affects the solidification behavior of the deposited droplets and thereby the quality of printed features.

In order to accurately print a feature, it is imperative to precisely predict quality of printed features based on machine input parameters. Hence, a statistical model that relates the input parameters of the MMJ process to the dimensional properties of the fabricated features is required.

3.3 Characterization tools

The following tools were used to characterize the printed features for the experimental studies performed.

1. Hirox KH 7700 digital microscope: This optical microscope was used for measuring the lateral dimensions of features deposited using the MMJ process.

2. Nanovea profilometer: This profilometer based on the technique of white light interferometry was employed to characterize the surface topography of the tracks printed using the MMJ process.

3. Struers grinding and polishing apparatus: This grinding and polishing tool was employed for grinding the printed features to reveal their internal microstructure for characterization studies.

4. Fluke multimeter: This multimeter was employed for characterizing the electrical performance (voltage and electrical resistance) of printed features.

5. A variable angle bending test setup was built completely in house to evaluate the electrical performance of printed features subjected to bending fatigue.

3.4 Materials

We have employed aluminum alloy 4043 for all experimental studies. The MK1 system used in this research is restricted to temperatures below 1000°C. Therefore, copper cannot be printed with the existing setup. However, successful fabrication of aluminum circuits could serve as a proof of concept for deposition of high temperature metal droplets on polymer substrates. The insights obtained in deposition of molten aluminum would provide considerable insight for future deposition of molten copper onto flexible substrates.

High-performance polymers have been prominently used in the microelectronic industry since the 1980's as interdielectric and passivation layers [130]. This is due to their ease of processability and excellent physical, chemical, and thermal properties. Various high-performance polymers such as Polyetheretherketone (PEEK), Polysulfone (PSU), Polyethersulfone (PES), Polyphenylene sulfone (PPSU), and Polyimide (PI) have been employed as dielectric substrates for printed electronic components [64]. Among the high-performance polymers, polyimides have found considerable interest for fabrication of devices due to their high thermal stability, excellent chemical resistance, good adhesion behavior with metals and good mechanical properties [64, 130, 131]. In this study, we have employed 125 μm (5mil, 0.005in) thick polyimide (Kapton® HN, DuPont) film as the flexible polymer substrate. All the experiments were done with as received polyimide film, and no other surface treatments were performed.

Chapter 4: Determination of jetting parameters for printed conductive traces

The demand for feature quality from the electronic industry necessitates the ability to produce uniform, smooth lines of fine resolution for printed electronic devices. Electrically conductive traces are at the heart of all electronic devices as they provide low resistance interconnections for the flow of electrical current. As we intend to study the feasibility of employing metal droplet deposition in fabrication of electronic circuits, it is crucial to understand the process conditions that would enable us to achieve high resolution printed traces with a given nozzle size. We have performed three studies to identify the key process conditions that would enable fabrication of high-resolution printed lines. The first study focuses on the impact of various key printing conditions on the diameter of the deposited droplets. Building off of the first study, the second study focuses on the impact of various printing conditions on the surface topology of the printed traces. The third study looks the impact of some key process conditions on the uniformity of the printed traces.

As discussed in Section 3.2, various process conditions including orifice size, droplet temperature, platform temperature, pulse length, pulse voltage, pulse frequency, standoff distance, and droplet overlap fraction can affect the quality of printed features. Among the process conditions, the pulse length (μs) and pulse voltage (V) have a significant effect on the quality of the droplet stream ejected from the nozzle. For a given nozzle size, relatively small changes in the pulse length and/or the pulse voltage can either enhance jet quality (i.e. produce a stable and consistent stream of drops with uniform diameter) or can make a stable jet stream unstable. A poor droplet jet stream may include satellite droplets, an unstable wavering jet with non-uniform drop sizes, or a jet that is not perpendicular to the platform. Poor-quality jets will adversely affect quality of the fabricated features of course. The pulse length and the pulse voltage that would result in a stable stream of droplets were found from experimental investigations. The exact values are considered

proprietary to the machine manufacturer and are hence not disclosed in this document. For all the experimental studies mentioned in this dissertation, the voltage and pulse length were kept constant to ensure jetting stability.

The typical orifice diameter employed for MHD molten metal jetting is 500μm. This provides a reasonable balance between layer resolution of the 3D printed metal components and throughput. However, achieving finer resolution than 500μm is highly desirable for printed electronics applications. Magnetohydrodynamic jetting of 3D printed structures with smaller diameter nozzles has already been demonstrated. Simonelli *et al.* reported silver droplet diameters as small as ~80 μm in a 3D printing setup [132]. Various orifice diameters, including 75μm, 100μm, 150μm, 200μm and 250μm, were initially explored in this research to evaluate the possibility of achieving finer resolution droplet streams and thereby finer resolution features. For our particular apparatus, the jet quality obtained from the 250μm orifice diameter was found to be the most stable for the longest duration of time and was the most repeatable. Hence an orifice size of 250μm was employed in the experimental studies.

In all the experimental studies in this chapter, the standoff distance between the nozzle and substrate was fixed at a distance of 15mm. This was chosen based on observations from preliminary studies. Lowering the standoff distance below 10mm was noted to result in significant warping of the polymer substrate due to the excessive heat transmitted from the nozzle to the substrate through convection and radiation. Having a higher standoff distance than 15mm was noted to result in significant deviation in the droplet placement accuracy even with very slight variations in the jet perpendicularity. The 15mm standoff distance was hence chosen because it was experimentally found to work very well for maintaining the droplet placement accuracy on the substrate and in reducing the substrate distortion due to excessive heat transmission from the nozzle.

4.1 Impact of process conditions on deposited droplets

One of the key factors that governs the ability to achieve high resolution features using a droplet-based deposition system is the diameter of the deposited droplets. Studying the effect of the process parameters on the diameter of the deposited droplets can help in identifying the conditions that would provide the finest droplet resolution with minimal deviation in drop diameter for a given nozzle size. This study is needed for conducting further parametric experimentation to achieve uniform printed feature morphology. In order to understand the impact of various key process conditions on the diameter of the deposited droplets, we have chosen to perform a design of experiments (DOE) study with the droplet diameter as the response variable.

Droplet temperature, substrate temperature and droplet ejection frequency were chosen as the factors that would be varied for the current DOE. The reason for choosing the current factors as the key parameters for our DOE is based on insights gathered from preliminary experimental studies and from published literature on inkjet printing of metal-based inks [41, 103, 133]. Studies based on inkjet printing of metal-based inks have shown that droplet temperature, substrate temperature and droplet ejection frequency play a crucial role on the morphology of deposited droplets [41, 48, 103, 133]. As we are also investigating a droplet-based deposition system, we chose to study the impact of droplet temperature, substrate temperature and droplet ejection frequency on the diameter of the deposited droplets. The goal of the study is to find the process conditions that would be suitable for achieving the finest droplet resolution with minimal deviation in droplet size for a given nozzle size.

Voltage and pulse length are the other two factors that can have a significant impact on the droplet ejection velocity and thereby the deposited droplet diameter. However, it was observed in our preliminary experiments that modifying the voltage and pulse length can significantly affect the quality of the jet and sometimes result in the formation of an unstable jet or a jet with satellite droplets. Hence, the voltage and pulse length were held constant at the conditions that provided the most stable jet. Based on the preliminary

experiments, 3 levels of each of the 3 factors were chosen for performing the experimental study. Table 4.1 shows the factors their respective levels and the definition of the factors.

Table 4.1: Factors and Levels used for the drop morphology study.

Factor	Definition	Levels		
		Level 1	Level 2	Level 3
Frequency	The number of droplets ejected from the nozzle per second.	50Hz	100Hz	200Hz
Droplet temperature	Temperature of the molten metal in the print head.	800°C	850°C	900°C
Substrate temperature	The temperature of the substrate during the printing process.	25°C	75°C	150°C

The temperature of the molten metal in the print head is measured using a thermocouple. The platform of the printer can be heated, and this heating capability was used to heat the substrate. The substrate was left on the platform for 10 min to attain equilibrium temperature of the substrate. A thermocouple was used to measure the temperature on the top of the substrate at 4 different locations to check whether the substrate was at the desired temperature. The metal droplets were only deposited onto the substrate after the validation of the substrate temperature was performed using a thermocouple.

A full factorial design of experiments with was employed to determine the effect of ejection frequency, droplet temperature and substrate temperature on the diameter of the deposited droplets. The diameter of the deposited droplets was measured using a Hirox digital microscope. Figure 4.1 shows the top view of

droplets deposited on a Kapton substrate and the measurement of diameter of the two droplets using the Hirox digital microscope.

Figure 4.1: Microscopic image of droplet diameter being measured on the Hirox microscope.

10 measurements were chosen at each experimental condition (i.e. diameter of 10 droplets is measured at each condition). The full factorial design was analyzed using MINITAB 18 statistical analysis software. Table 4.2 shows the analysis of variance.

Table 4.2: Analysis of variance for average droplet diameter.

Analysis of Variance

Source	DF	Seq SS	Contribution
Model	26	705376	63.38%
Linear	6	695788	62.52%
Ejection frequency	2	454543	40.84%
Droplet temperature	2	22602	2.03%
Substrate temperature	2	218642	19.65%
2-Way Interactions	12	9264	0.83%
Ejection frequency*Droplet temperature	4	1348	0.12%
Ejection frequency*Substrate temperature	4	6985	0.63%
Droplet temperature*Substrate temperature	4	931	0.08%
3-Way Interactions	8	325	0.03%
Ejection frequency*Droplet temperature*Substrate temperature	8	325	0.03%
Error	243	407560	36.62%
Total	269	1112936	100.00%

Source	Adj SS	Adj MS	F-Value
Model	705376	27130	16.18
Linear	695788	115965	69.14
Ejection frequency	454543	227271	135.51
Droplet temperature	22602	11301	6.74
Substrate temperature	218642	109321	65.18
2-Way Interactions	9264	772	0.46
Ejection frequency*Droplet temperature	1348	337	0.20
Ejection frequency*Substrate temperature	6985	1746	1.04
Droplet temperature*Substrate temperature	931	233	0.14
3-Way Interactions	325	41	0.02
Ejection frequency*Droplet temperature*Substrate temperature	325	41	0.02
Error	407560	1677	
Total			

Source	P-Value
Model	0.000
Linear	0.000
Ejection frequency	0.000
Droplet temperature	0.001
Substrate temperature	0.000
2-Way Interactions	0.936
Ejection frequency*Droplet temperature	0.938
Ejection frequency*Substrate temperature	0.387
Droplet temperature*Substrate temperature	0.968
3-Way Interactions	1.000
Ejection frequency*Droplet temperature*Substrate temperature	1.000
Error	
Total	

Model Summary

S	R-sq	R-sq(adj)	PRESS	R-sq(pred)
40.9537	63.38%	59.46%	503161	54.79%

At a 95% confidence interval, it can be observed from the ANOVA that all the three individual factors have a significant impact on the drop diameter as their P-values are < 0.05. ANOVA also reveals that none of the higher order interactions have a significant impact on the drop diameter as their P-values are all > 0.05. The Pareto chart in Figure 4.2 illustrates this effect, as the individual factors of ejection frequency, droplet temperature, and substrate temperature are shown to be significant.
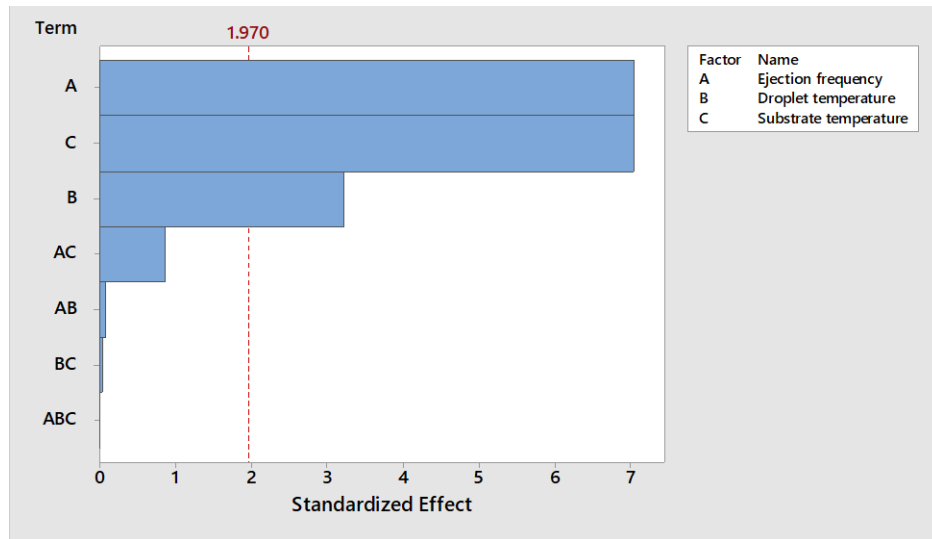
Figure 4.2: Pareto chart of the standardized effects for average droplet diameter.

The fits and diagnostics for the unusual observations, as shown in Table 4.3 reveals that 14 out of the 17 measurements with unusually high standard residuals were printed at the frequency of 200Hz. The cells highlighted in green are the observations made for 200Hz ejection frequency. This reveals that there is a significant variation in the size among the droplets deposited at the high frequency condition of 200Hz. The significant variation in the droplet size may be explained by the necking of the metal droplets in an erratic fashion at the high frequency conditions.

Table 4.3: Fits and diagnostics for unusual observations.

				Fits and Diagnostics for Unusual Observations									
Obs	Ejection Frequency	Drop temperature	Substrate temperature	Drop diameter	Fit	SE Fit	95% CI	Resid	Std Resid	Del Resid	HI	Cook's D	DFITS
19	200	800	25	106	238.1	13	(212.6, 263.6)	-132.1	-3.4	-3.48	0.1	0.05	-1.15893
20	200	800	75	182	280.6	13	(255.1, 306.1)	-98.6	-2.54	-2.57	0.1	0.03	-0.85562
86	50	850	75	429	347.9	13	(322.4, 373.4)	81.1	2.09	2.1	0.1	0.02	0.70068
93	100	800	150	275	378.6	13	(353.1, 404.1)	-103.6	-2.67	-2.7	0.1	0.03	-0.90028
96	100	850	150	257	360	13	(334.5, 385.5)	-103	-2.65	-2.68	0.1	0.03	-0.89491
102	200	800	150	219	304.1	13	(278.6, 329.6)	-85.1	-2.19	-2.21	0.1	0.02	-0.73592
104	200	850	75	349	267.6	13	(242.1, 293.1)	81.4	2.1	2.11	0.1	0.02	0.70332
105	200	850	150	185	293.2	13	(267.7, 318.7)	-108.2	-2.78	-2.82	0.1	0.03	-0.94154
107	200	900	75	356	251.8	13	(226.3, 277.3)	104.2	2.68	2.72	0.1	0.03	0.90565
108	200	900	150	165	283.4	13	(257.9, 308.9)	-118.4	-3.05	-3.1	0.1	0.04	-1.03367
131	200	850	75	172	267.6	13	(242.1, 293.1)	-95.6	-2.46	-2.49	0.1	0.02	-0.82891
161	200	900	75	157	251.8	13	(226.3, 277.3)	-94.8	-2.44	-2.47	0.1	0.02	-0.8218
183	200	800	150	221	304.1	13	(278.6, 329.6)	-83.1	-2.14	-2.15	0.1	0.02	-0.71829
209	200	800	75	360	280.6	13	(255.1, 306.1)	79.4	2.04	2.06	0.1	0.02	0.68573
211	200	850	25	324	229.7	13	(204.2, 255.2)	94.3	2.43	2.45	0.1	0.02	0.81735
240	200	850	150	376	293.2	13	(267.7, 318.7)	82.8	2.13	2.15	0.1	0.02	0.71564
262	200	800	25	329	238.1	13	(212.6, 263.6)	90.9	2.34	2.36	0.1	0.02	0.78719
266	200	850	75	389	267.6	13	(242.1, 293.1)	121.4	3.12	3.18	0.1	0.04	1.06095

Figure 4.3 shows top view micrographs of droplets deposited on the substrate at each jetting frequency. The droplets deposited at 200Hz frequency can be seen to have a significant variation in the size in comparison to droplets printed at 50 and 100 Hz.
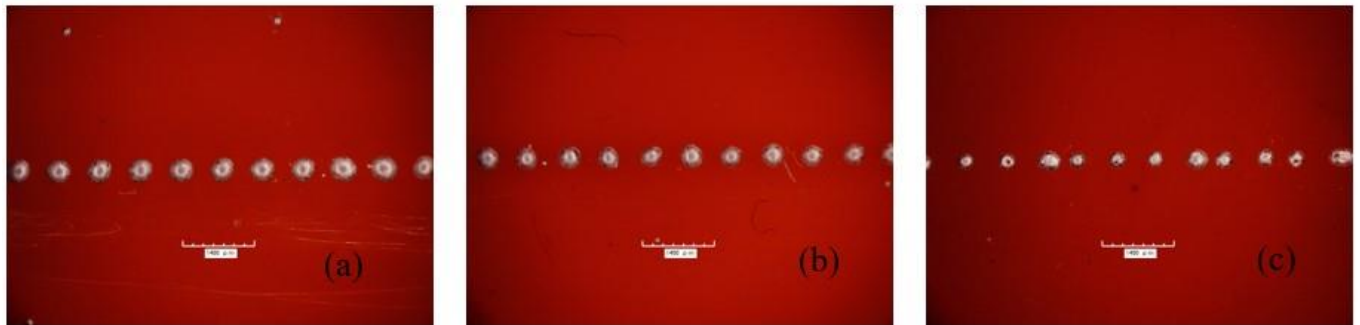
Figure 4.3: Micro graphs of droplets printed at (a) 50Hz, (b) 100Hz and (c) 200 Hz.

The Normal Probability Plot shown in Figure 4.4 reveals the presence of a few outliers corresponding to the highly variable droplet diameters obtained at the high frequency condition of 200 Hz. Below 200 Hz, it

54

can be said that the normality assumption is valid. From the Versus Fits plot in Figure 4.4 it can be observed that the residuals do not show any specific pattern, so the assumption of constant mean and constant variance can be concluded as satisfied. From the Versus Order plot it can be observed that there are no patterns of the residuals with respect to time, so the independence assumption can also be termed as valid.
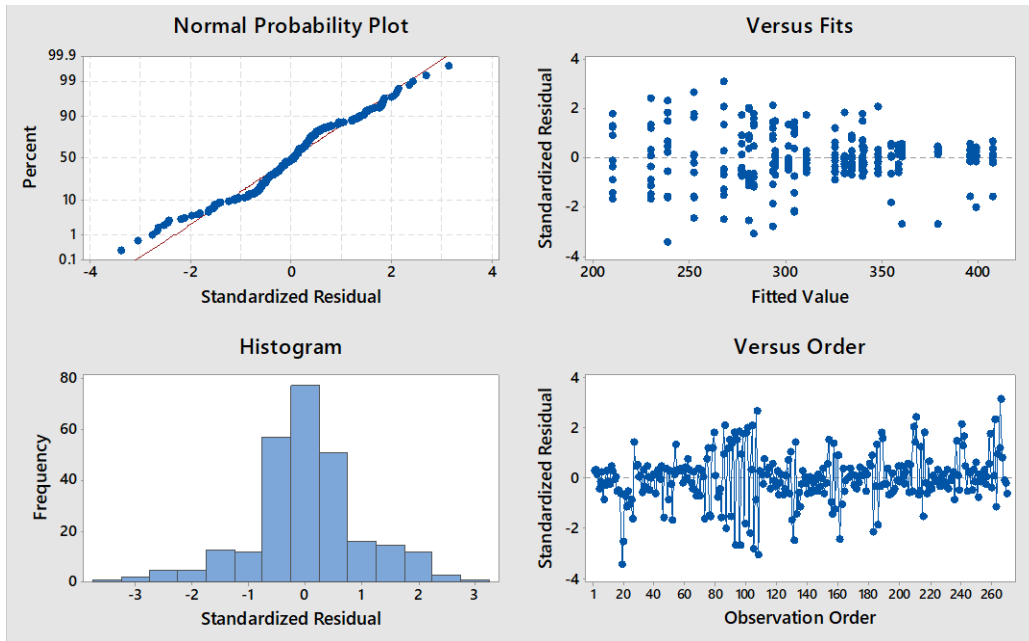
Figure 4.4: Residual plots for average drop diameter.

The Main Effects Plot shown in Figure 4.5 reveals that the increase in ejection frequency and droplet temperature results in a decrease in the diameter of the deposited droplets. Whereas an increase in substrate temperature results in an increase in the deposited drop diameter. The interaction plot shown in Figure 4.6 no interaction between the three factors.
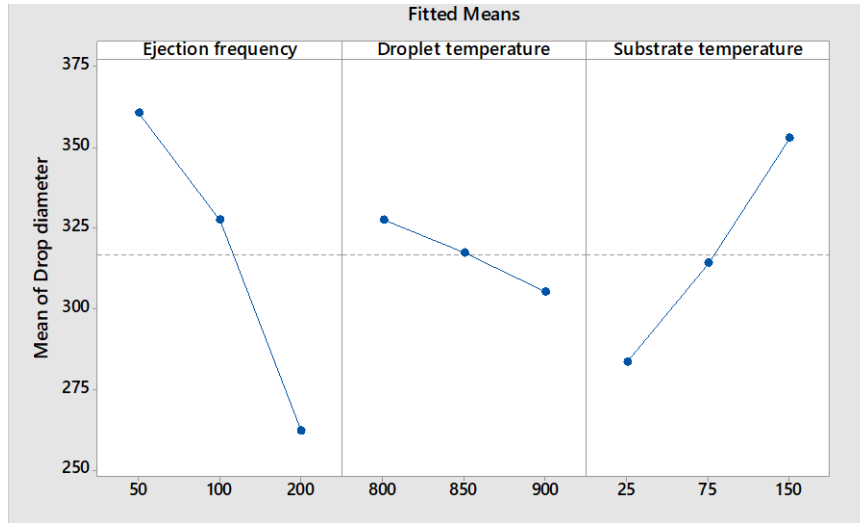
Figure 4.5: Main effects plot for average drop diameter.

From the main effects plot in Figure 4.5 it can be seen that the mean droplet diameter decreases with the increase in frequency. This phenomenon could be explained by the meniscus oscillation at the orifice. After a droplet has separated from the fluid in the nozzle, the meniscus retracts and oscillates for a certain duration. This is a well-documented phenomenon in inkjet printing [134]. At higher frequency conditions, the subsequent droplet is likely being ejected before the meniscus oscillations have dampened out. This could lead to droplet ejection in some cases where the meniscus is retracting and thereby leading to smaller sized droplets.

The increase in droplet temperatures affects the viscosity and the surface tension of the molten metal. This could potentially contribute to creation of smaller droplet diameters at higher temperatures. The increase in drop diameter with the increase in substrate temperature is likely attributed to the increase in surface energy of the substrate which in turn affects the spreading of the deposited droplet and thereby the droplet diameter.
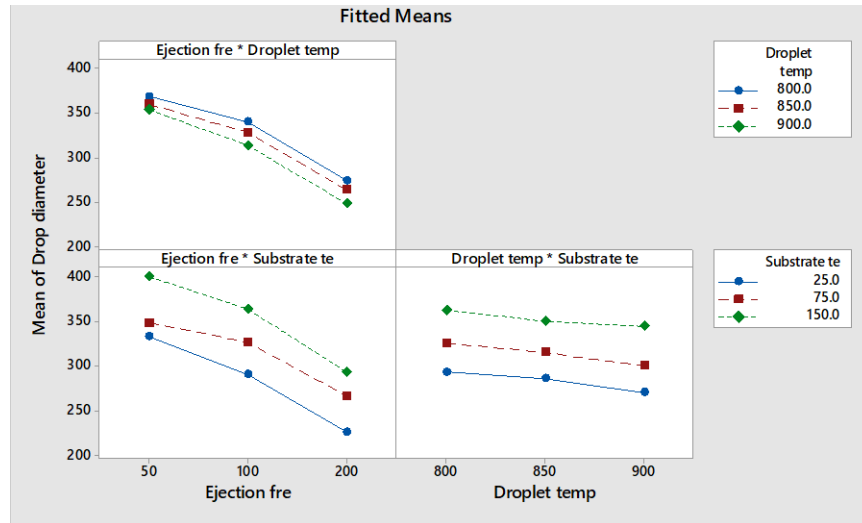
Figure 4.6: Interaction plot for average drop diameter.

The details of response optimization are shown in Table 4.4 and the optimization plot is shown in Figure 4.7. The ejection frequency of 200 Hz was not considered for calculating the optimal conditions for obtaining the minimal drop dimeter because of the significant variability in the droplet size generated at the 200 Hz frequency. The optimization plot reveals that the ejection frequency of 100 Hz, droplet temperature of 900 ᵒC and substrate temperature of 25 ᵒC provides the minimal droplet size with the current setup.

Table 4.4: Response optimization for average droplet diameter.

Parameters

Response	Goal	Lower	Target	Upper	Weight	Importance
Drop diameter	Minimum		106	434	1	1

Variable Ranges

Variable	Values
Ejection frequency	50, 100
Droplet temperature	800, 850, 900
Substrate temperature	25, 75, 150

Solution

Solution	Ejection frequency	Droplet temperature	Substrate temperature	Drop diameter Fit	Composite Desirability
1	100	900	25	276.7	0.479573

Multiple Response Prediction

Variable	Setting
Ejection frequency	100
Droplet temperature	900
Substrate temperature	25

Response	Fit	SE Fit	95% CI	95% PI
Drop diameter	276.7	13.0	(251.2, 302.2)	(192.1, 361.3)
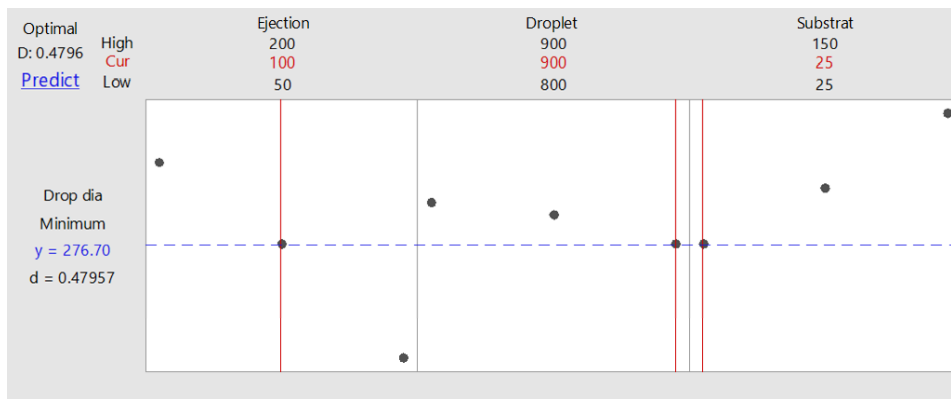
Figure 4.7: Optimization plot for average droplet diameter.

In order to test the validity of the model within the design space, intermediate parameter settings were used that were not part of the original experiment. The settings used for validation are tabulated in Table 4.5.

The other experimental conditions were the same as the conditions employed for the original set of experiments.

Table 4.5: Levels of the factors used for the validation study.

Factor	Level 1	Level 2
Ejection frequency (Hz)	75	150
Droplet temperature (^{o}C)	825	875
Substrate temperature (^{o}C)	50	112.5

Droplets were printed with the settings mentioned above and were compared with the predicted values from the regression analysis. The comparison is tabulated in Table 4.6.

Table 4.6: Predicted and Actual droplet diameter for the validation study.

Run	Ejection frequency (Hz)	Droplet temperature (^{o}C)	Substrate temperature (^{o}C)	Predicted value (µm)	Actual value (µm)
1	75	825	50	331.27	328
2	75	825	50	331.27	346
3	75	825	50	331.27	334
4	150	875	112.5	305.31	291
5	150	875	112.5	305.31	312
6	150	875	112.5	305.31	295

The validation experiment shows a less than 2% error between the predicted and actual values. It was observed that the error was within the prediction interval (standard error, ±6.274) of the regression model. As this observed error lies within the prediction space of the model, it was concluded that there was no

evidence to support curvature, and the regression model for the droplet diameter is deemed valid. The insights gathered from this experimental study will guide the next batch of experiments.

4.2 Impact of process conditions on surface roughness of printed traces

The strict demand on feature quality from the electronic industry necessitates uniform, smooth traces of fine resolution for printed electronic devices. In order to fabricate uniform and smooth features, it is crucial to study the process conditions that would influence the surface texture of the printed features. Similar to the prior study, we have chosen to perform a design of experiments (DOE) study looking at the surface texture so that we can identify the suitable process conditions for achieving the smoothest possible features.

The center-to-center distance between adjacent droplets deposited onto a substrate is typically referred to as drop spacing. An illustration of the top view of droplets deposited onto a surface is provided in Figure 4.8, showing the drop diameter and drop spacing. Prior studies on droplet-based deposition processes have shown that drop spacing could have a major impact on the quality of the fabricated features [26]. Jetting frequency is chosen as one of the factors that would be varied in this study. This was chosen because screening experiments have revealed that it plays an influential role on surface topology. From the drop morphology study presented in the previous section, we have noted that the diameter of the deposited droplet (D_d) varies with changes in jetting frequency. In order to normalize drop spacing (d_s) for any given droplet diameter (D_d), a droplet overlap fraction (O_d) relative to the droplet size is used rather than an absolute drop spacing distance. The numerical relationship between O_d, D_d, and d_s is shown in Eq. (1). An overlap fraction of 0.0 would indicate that adjacent droplets tangentially touch each other but do not overlap prior to liquid spreading. An overlap fraction of 1.0 would indicate that droplets land directly on top of each other. A negative overlap fraction would indicate that the drop spacing is larger than the drop diameter,

thus resulting in discrete isolated drops rather than a continuous line. It is important to emphasize that the drop spacing is relative to the drop diameter and does not account for droplet spreading, coalescence, or surface tension effects after the drops land.

$$d_s = D_d(1 - O_d) \qquad (1)$$
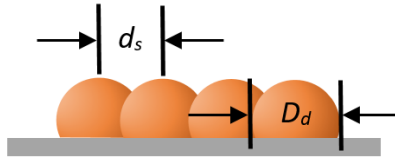
Figure 4.8: Illustration of drop spacing and drop diameter.

For this study, we have chosen not to employ any parameters that are specific to our apparatus. All parameters varied in this study would play a key role regardless of the ejection method used for deposition of metal droplets. The parameters that were varied as part of our experimental study include ejection frequency, substrate temperature, and droplet overlap fraction (O_d). The levels chosen for each factor are shown in Table 4.7. These parameters were selected based on data from screening experiments and prior studies related to droplet deposition techniques for fabricating printed electronics [41, 48, 103, 133, 135]. Droplet temperature is another factor that could influence the line morphology. However, the droplet temperature was not considered for this study as our prior experimental study on drop morphology revealed that effect of droplet temperature on the drop diameter is relatively low.

Based on the preliminary experiments, 4 levels of each of the 3 factors were chosen for performing the experimental study. Although the drop morphology study indicated that the high frequency condition of 200 Hz resulted in significant variation in the drop dimeter size, we have chosen to include 200 Hz and 400 Hz conditions in the current experimental study. This was done to get a comparative picture on the impact of higher frequency on the track topology.

Factor	Levels			
	Level 1	**Level 2**	**Level 3**	**Level 4**
Substrate temperature (^{o}C)	25	75	150	200
Ejection frequency (Hz)	50	100	200	400
Overlap fraction (O_d)	0.10	0.25	0.50	0.75

Polyimide (Kapton® HN, DuPont) film with a 125 µm thickness (5 mil, 0.005 in) was used as the flexible polymer substrate for all experiments. Polyimide was selected for its high temperature resistance, its structural integrity, and because it is widely used in the electronics industry as a flexible dielectric substrate. All printing experiments were done with as-delivered Kapton film. No special cleaning or surface treatments were performed, and a single pass was used for all the prints. Separate substrates were used for each temperature, these were removed immediately after printing. The substrates were held down on the heated build platen in the MK1 machine using Kapton tape and left on the platform for 10 minutes to attain equilibrium temperature of the platform. The substrate temperature was monitored using a thermocouple. To prevent significant variation in the jet quality, the print time was kept to a minimum.

To measure the surface topology of the printed tracks, we have chosen to measure the height of the printed tracks at several locations along the center of the printed tracks, over a length of 3 mm using a Nanovea optical profilometer. A height measurement was made along the center of the track at 10 µm intervals. The most common statistical descriptors of surface roughness are the roughness average R_a (Eq (2)), and the RMS roughness R_q (Eq (3)). In these equations, y_i is the height of the measured point from the bottom of the feature, and N is the total number of points at which the measurements were made.

$$R_a = \frac{\Sigma(y_i)}{N} \tag{2}$$
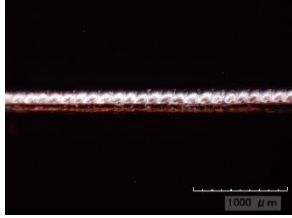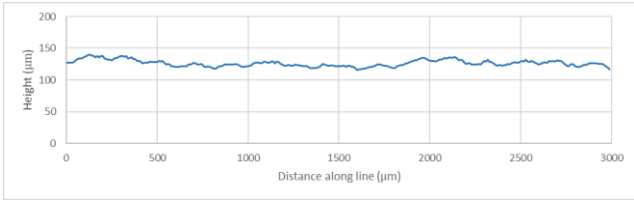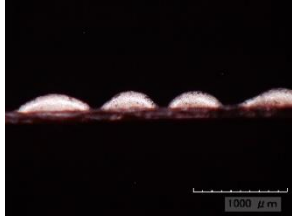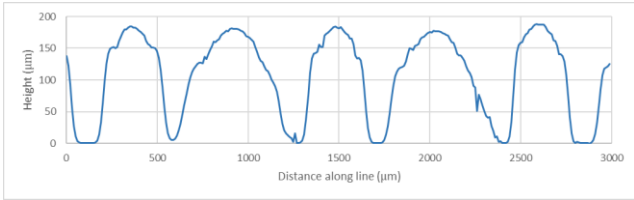
$$R_q = \sqrt{\Sigma(y_i)^2 / N} \tag{3}$$

Both descriptors employ the measurement of the height from the bottom of the printed features. For our application, we have noted that there can be conditions where the R_q value for two of the printed features can be very close, but their top surface roughness can vary significantly. As we are interested in the topology of the top surface of the printed features regardless of the absolute height of the line, we have chosen to use the standard deviation of the heights (R_{sd}). The standard deviation of the roughness is given by the formula in Eq (4).

$$R_{sd} = \sqrt{\Sigma(y_i - \bar{y})^2 / N} \tag{4}$$
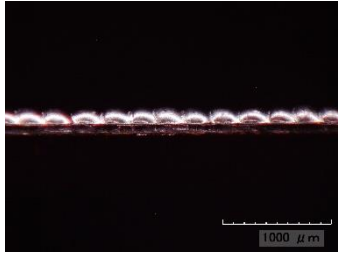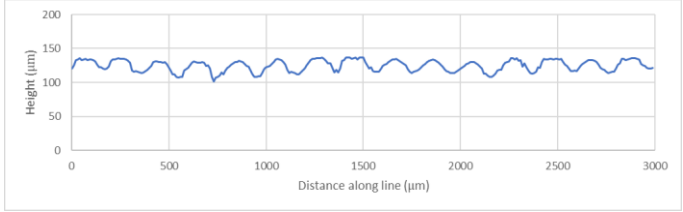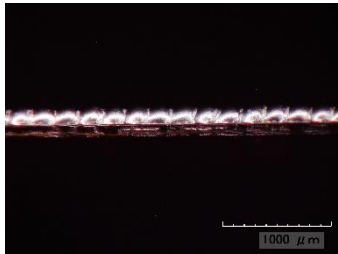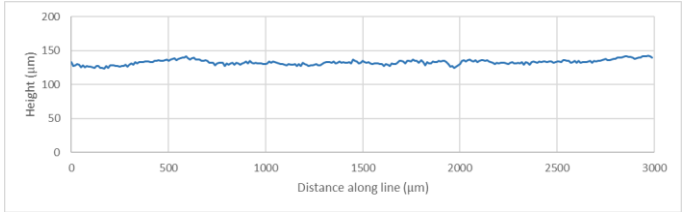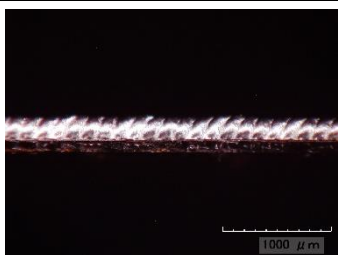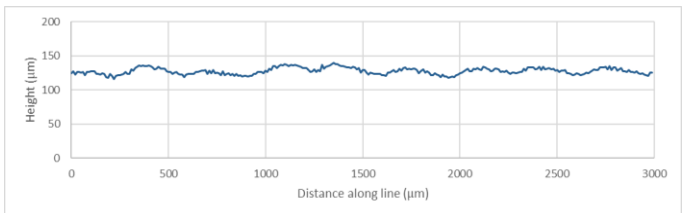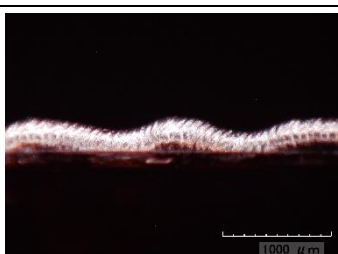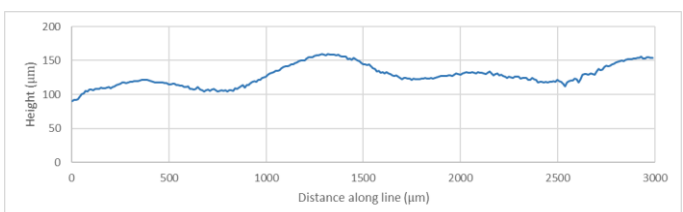
This R_{sd} would give us the deviation of the height of each point from the average height of all the points measured along the center line on the top surface. The higher standard deviation for the measured points from the average will indicate a rougher surface whereas a standard deviation close to zero would indicate a smoother surface. Table 4.8 shows the height profiles of two of the printed lines, their RMS roughness (R_q), and the standard deviation roughness (R_{sd}). The R_q for surface of track (a) is 5.39 µm whereas the R_q of track (b) is 6.56 µm. While the R_{sd} of the track (a) is 6.14 µm and the R_{sd} of track (b) is 56.907 µm. The R_{sd} roughness can be seen to provide a better distinction between the two profiles and was therefore employed to perform the design of experiments (DOE) study.

Table 4.8: R_q and R_{sd} of height for tracks with different surface topology.

	Micrographs of side view	Top profile height	R_q	R_{sd}
(a)			5.39	6.14
(b)			6.56	56.907

In Table 4.9, the top surface profile data for different overlap fraction (O_d) levels at the frequency condition of 50 Hz and substrate temperature of 25 ºC, together with the microscope images of the side view of the printed lines are reported. As expected, changes in O_d can be seen to result in a substantial difference in the R_{sd} height of the profile. A decrease in the R_{sd} can be noted with an increase in the O_d from 0.10 to 0.25. This reduction in the R_{sd} could be because of a better coalescence of the adjacent droplets at the O_d of 0.25. At an O_d of 0.10, the droplets are spaced farther apart, thereby resulting in distinctive individual droplets and increased R_{sd}. However, the R_{sd} increases from the O_d of 0.25 to 0.75. An increase in overlap beyond a certain point result in building of droplets on top of precedent droplets, and the deposited droplets actually lift up off of the substrate and grow upwards. After some droplets are deposited, they collapse due to their own gravity. This explains the larger peaks and the peak-to-peak distance for the surface profile measured for O_d of 0.75.

O_d	Micrographs of side view	Top profile height	R_{sd} (µm)
10			16.03
25			5.15
50			8.28
75			26.84

Changes in jetting frequency were also noted to result in a substantial difference in the R_{sd} height of the profile. Table 4.9 shows the micrographs and surface profiles of traces fabricated at various overlap fraction

conditions. Like the case of change in O_d, a decrease in the R_{sd} was noted with an increase in the frequency from 50 to 100 Hz. This reduction in the R_{sd} could be because of a better coalescence of the adjacent droplets at the higher frequency of 100 Hz. The change in substrate temperature was noted to result in only a minor variation in the R_{sd} height of the profile. The R_{sd} was noted to increase slightly as substrate temperature was increased from 25°C to 200°C. This increase in the R_{sd} is likely due to a slight increase in the solidification time of the deposited droplets with the increase in substrate temperature. However, the increase in the R_{sd} with the substrate temperature was noted to be very minimal and not statistically significant.

A full factorial design of experiments was employed to analyze the effects of the three parameters and their interactions on the R_{sd} roughness of the printed tracks. Because of the constraints with time with respect to the profilometry measurements, no replication was employed in the current study. The full factorial design was analyzed using MINITAB 18 statistical analysis software. Table 4.10 shows the analysis of variance (ANOVA).

Table 4.10: Analysis of variance.

Analysis of Variance

Source	DF	Adj SS	Adj MS	F-Value	P-Value
Model	36	77546	2154.1	3.34	0.001
Linear	9	56099	6233.2	9.65	0.000
Substrate temperature	3	4359	1452.9	2.25	0.105
Overlap fraction	3	11150	3716.7	5.76	0.004
Frequency	3	40590	13530.0	20.96	0.000
2-Way Interactions	27	21447	794.3	1.23	0.297
Substrate temperature*Overlap fraction	9	5694	632.6	0.98	0.478
Substrate temperature*Frequency	9	4718	524.2	0.81	0.610
Overlap fraction*Frequency	9	11036	1226.2	1.90	0.096
Error	27	17432	645.6		
Total	63	94978			

Model Summary

S	R-sq	R-sq(adj)	R-sq(pred)
25.4092	81.65%	57.17%	0.00%

At a 95% confidence interval, it can be observed from the ANOVA that overlap fraction and ejection frequency have a significant impact on the R_{sd} roughness, as their P-values are < 0.05. The substrate

temperature does not have a significant impact on the response variable. ANOVA also reveals that none of the higher order interactions have a significant impact on the R_{sd}, as their P-values are all > 0.05. The Pareto Chart shown in Figure 4.9 also illustrates this effect, as the individual factors of frequency and overlap percentage are shown to be significant.
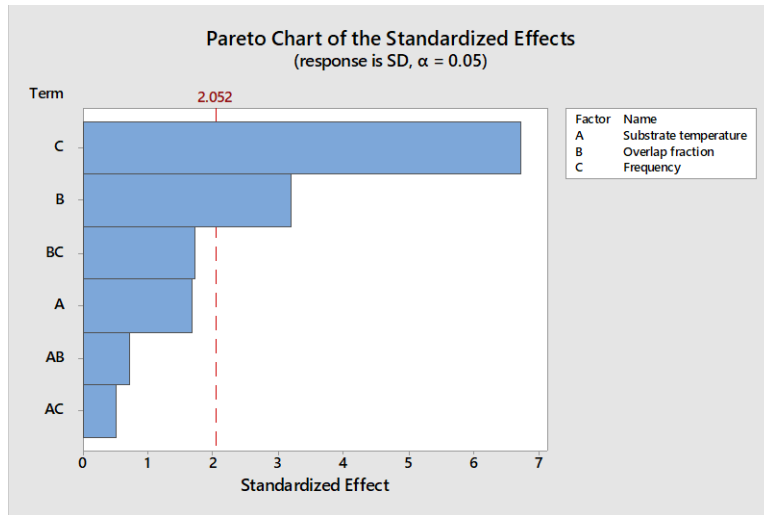
Figure 4.9: Pareto chart of the standardized effects for R_{sd} roughness.

The fits and diagnostics for unusual observations, as shown in Table 4.11 reveals that all measurements with unusually high standard residuals were printed at frequencies of 200 Hz and 400 Hz. This is similar to the result obtained for the droplet diameter study. The significant variation in the surface roughness may be explained by the high variation in the drop diameter at higher frequency conditions.

				Fits and Diagnostics for Unusual Observations			
Obs	Substrate temperature	Overlap fraction	Frequency	SD	Fit	Resid	Std Resid
4	25	10	400	97.8	53.7	44.1	2.67
31	75	75	200	31.5	66.1	-34.6	-2.1
32	75	75	400	152.3	115.6	36.8	2.23
63	200	75	200	136.3	102.3	34	2.06

The Normal Probability Plot and the Histogram shown in Figure 4.10 reveal the normality of residuals, validating the normality assumption. The Versus Fits plot did not indicate abnormalities in the variance, so there was not enough evidence to suspect non-constant variance. The assumption of constant mean and constant variance can be concluded as satisfied. From the Versus Order plot, it can be observed that there are no patterns of the residuals with respect to time, so the independence assumption can also be termed as valid.
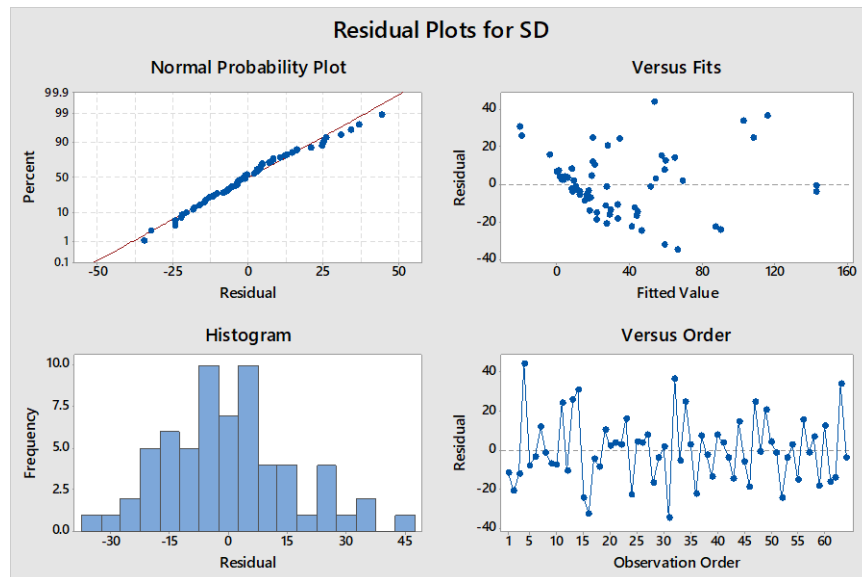
Figure 4.10 Residual plots for SD roughness.

The Main Effects Plot shown in Figure 4.11 reveals that the surface texture with the lowest R_{sd} roughness can be obtained when the substrate temperature is at the lowest level. In terms of the overlap fraction and frequency, the surface finish improves from the first level to the second level and deteriorates with further increase in the levels. This is consistent with the observations in the micrographs from Table 4.9.
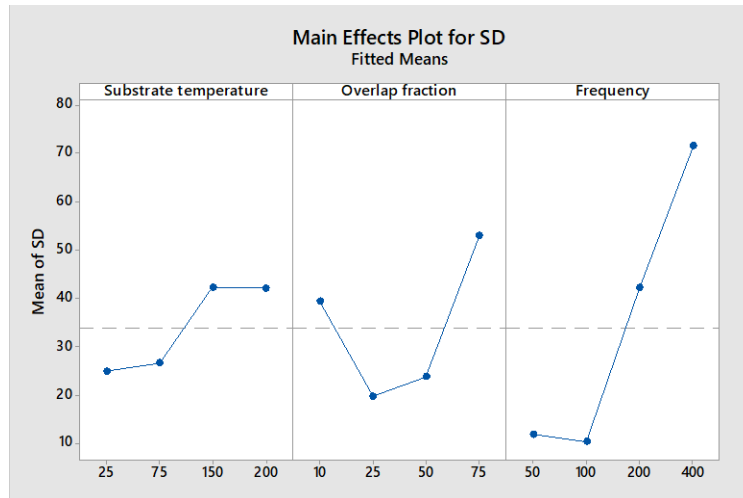
Figure 4.11: Main effects plot for SD roughness.

From the main effects plot in Figure 4.11, it can be seen that the surface roughness shows a modest increase with an increase in substrate temperature. This could be due to the fact that surface energy increases with an increase in substrate temperature. This could, in turn, affect droplet spreading and hence surface roughness of the printed traces. However from the Pareto chart shown in Figure 4.9, it can be seen that the effect of substrate temperature on the surface roughness is relatively low, hence the increase in the surface roughness with the substrate temperature is not statistically significant.

In the case of droplet overlap fraction, there is a decrease in the surface roughness from overlap fraction of 10 to 25. The high surface roughness of tracks with an overlap fraction of 10 could be due to the fact that the drops are significantly farther apart, thus leading to distinct droplet shapes and therefore high surface

roughness. Many of the traces printed at overlap fraction of 25 would have been relatively uniform traces with lower surface roughness. The surface roughness, however, increases as overlap fraction increases from 25 to 75. The increase in the surface roughness from 25 to 50 is relatively small, whereas the increase in the surface roughness from the overlap of 50 to 75 is quite large. This could be due to that fact many of the traces printed at an overlap of 75 would have resulted in lift off of the trace from the substrate leading to wavy surfaces and therefore higher surface roughness. This phenomenon can be seen in the micrographs provided in Table 4.9.

The increase in frequency from 50 to 100 Hz was noted to result in a slight decrease in the surface roughness of printed features. This could be because of the fact that the shorter time between droplet arrivals leads to better coalescence between adjacent droplets and a smoother surface. The surface roughness was noted to increase dramatically when the frequency was increased from 100 to 400Hz though. This is presumed to be connected to the larger droplet size variation seen at higher frequency conditions as discussed in Section 4.1. The surface roughness variation shows that higher frequency conditions may not be suitable for printing features with smooth surfaces.
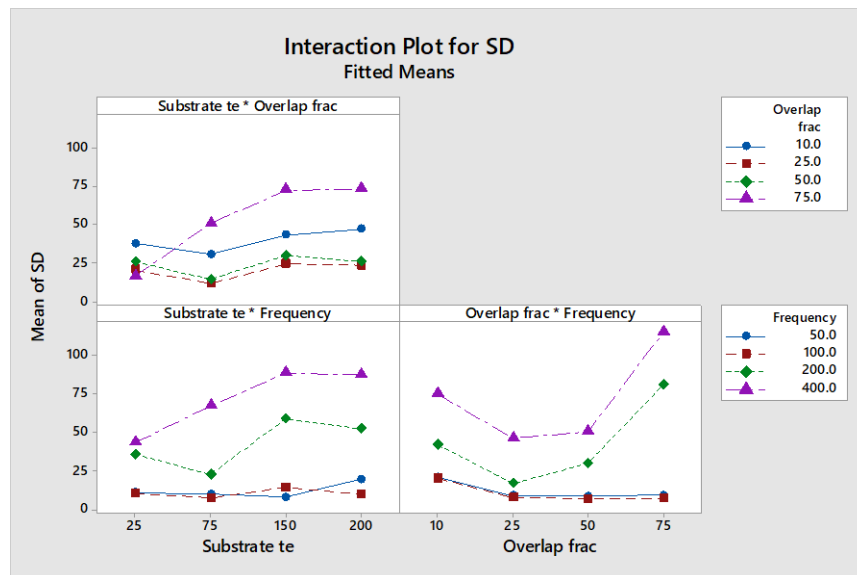
Figure 4.12: Interaction plot for SD roughness.

The optimization plot is shown in Figure 4.13. The optimization plot reveals that a substrate temperature of 25 °C, overlap fraction of 0.25, and frequency of 100Hz provide the minimal R_{sd} surface roughness with the current setup.
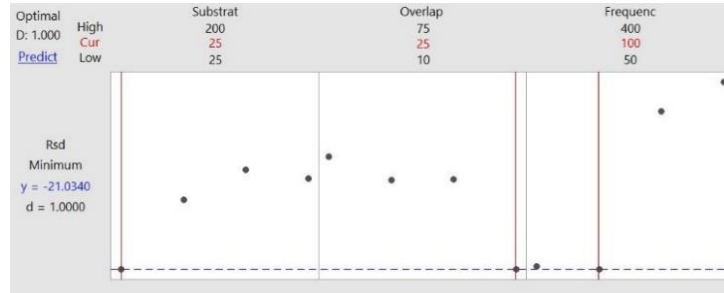
Figure 4.13: Response optimization for SD roughness.

The R_q value for the line with the lowest R_{sd} roughness is calculated to be about 5µm. This study illustrates the feasibility of fabricating features with R_q surface roughness values in the range of 5µm using molten metal droplet deposition systems. R_q values for standard electrically conductive copper foils used in printed circuit boards is typically about 2µm [136]. This shows that with further efforts it is feasible to fabricate functional circuitry with surface roughness close to the surface roughness of electrically conductive features currently used in PCB's, using molten metal deposition processes.

4.3 Impact of process conditions on morphology of printed traces

The demand for high feature quality from the electronic industry requires the ability to produce uniform, smooth traces of fine resolution for printed electronic devices. Soltman *et al*. have demonstrated the importance of process conditions such as drop spacing and drop deposition frequency on uniformity of traces printed using inkjet printing with an electrically conductive polymer-based ink [133]. In this study, a similar approach is taken to characterize the morphologies of traces printed with molten metal droplets as

a function of printing process conditions. This is intended to classify and obtain a better understanding of the process conditions that lead to uniform printed lines.

The independent variables used in this experimental study were the overlap fraction (O_d) and drop ejection frequency. Overlap fraction was adjusted between 0.0 to 0.7 in increments of 0.1. The droplet deposition frequency was varied from 25 Hz to 125 Hz in increments of 25 Hz. Jetting frequency affects the time that a droplet has to cool down and start solidifying before the subsequent droplet arrives. Likewise, drop overlap fraction directly affects the amount of molten metal deposited per unit length of a conductive trace. At one extreme, printing with low overlap fraction and low frequency will result in drops that are spaced apart and which have time to cool and solidify prior to impingement of subsequent droplets. At the opposite extreme, printing with a large droplet overlap fraction at high frequency will result in large overlap between droplets, and the droplets will also not have time to solidify prior to arrival of the next drop.

The droplet overlap-fraction and jetting frequency values used in this study were chosen to avoid complete melting through the 125 μm thick Kapton film. Screening experiments revealed that charring and substrate distortion occurs at overlap fractions > 0.8 and frequency conditions >150 Hz. The combination of high overlap fraction, with modest or high droplet jetting frequency results in sufficiently high thermal flux to damage the substrate. Other parameters, such as the drop size, droplet temperature, substrate material, and substrate thickness, can also have an effect on substrate damage. For example, the thermal energy within each droplet varies as a function of the droplet volume. The droplet volume, in turn, varies as a function of the cube of the diameter. Therefore, as drop diameter decreases, the risk of thermal damage to a given substrate rapidly decreases. Substrates with low glass transition temperatures, such as polyethylene terephthalate (PET), are more susceptible to thermal damage. For example, we have noted from screening experiments that at the same jetting conditions, 125 μm thick PET completely melted, where as a polyimide substrate of 125 μm thickness experienced no noticeable damage. Substrate thickness can also affect the amount of damage to the substrate. At the conditions where no substrate damage was noted for a 125 μm thick polyimide, significant warping was observed in 75 μm thick polyimide.

Lastly, substrate temperature can also have a significant effect on print quality. It was noted that large, entrapped gas pores, or pinholes, were observed within metallic traces printed on room temperature (unheated) polyimide substrates. In some cases, the pinholes extended through the top edges of printed traces. This would be undesirable for flexible electronic applications because the pinholes would likely lead to crack initiation, crack propagation and failure during flex cycles. When the polyimide was sufficiently heated, the printed traces were essentially free of these pinholes. Polyimide is known to be highly hygroscopic, and the hypothesis behind the presence of pinholes in unheated substrates is that the molten metal upon impact heats the absorbed moisture in the polyimide beyond the boiling point of water and releases water vapor into the solidifying droplet. This phenomenon is discussed in detail in the next chapter. A 200 °C substrate temperature was experimentally found to be sufficiently high to virtually eliminate pinholes without causing any visually apparent damage to the polyimide, hence it was employed for all the experimental runs.

In order to keep the experimental matrix at a reasonable size, the drop size, substrate material, and substrate thickness were fixed. Not surprisingly, the morphology of printed traces changes as the combination of overlap fraction and jetting frequency moves from one extreme (low overlap at low frequency) to the other (high overlap at high frequency). Five distinctly different regimes were observed and are described as follows.

Scalloped Lines: At very low jetting frequency (i.e. 25 Hz), each drop will have more time to cool and solidify prior to arrival of the next drop. When the drop overlap fraction is also very low (i.e. 0 – 0.3), it results in a distinct semi-spherical drop volumes connected by small necks. An example of a scalloped printed trace is shown in Figure 4.14. The trace is printed at an overlap fraction of 0 and a frequency of 25 Hz.
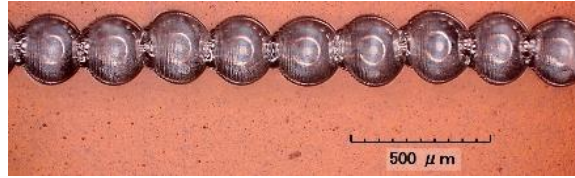
Figure 4.14: Scalloped traces resulting from an overlap fraction of 0.0 and a jetting frequency of 25 Hz.

Lift-Off Lines: At very low jetting frequency (i.e. 25 Hz) and medium to high overlap fractions (i.e. 0.5 – 0.7), the printed traces began to vertically lift up off of the substrate. When there is a reasonable amount of overlap between successively deposited droplets at a low frequency, droplets landing on a fully solidified drop will also begin to solidify before the drop rolls over and touches the substrate. Consequently, there is a vertical lift off of the printed trace above the substrate until the mass of material is sufficiently large to cause the trace to droop back down towards the substrate. Figure 4.15 showcases this behavior produced at a droplet overlap fraction of 0.6 and a jetting frequency of 25 Hz through the top and side views.

(a)
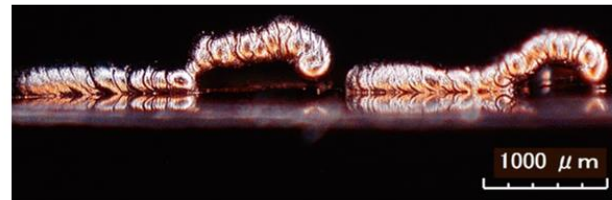
(b)

Figure 4.15: (a) Top view and (b) front view of raised traces resulting from an overlap fraction of 0.6 and a jetting frequency of 25 Hz.

Discontinuous Lines: At intermediate frequencies (i.e. 125 Hz), drops arrive before the deposited drop(s) have sufficient time to cool down and at least solidify partially. At low droplet overlap fractions (i.e. 0 – 0.2) with high jetting frequency, liquid surface tension effects play a prominent role and result in discontinuous beads. Similar behavior is known to occur in inkjet printing at larger line widths with slow-

drying inks. Discontinuous lines printed at a droplet overlap fraction of 0.1 and a jetting frequency of 125 Hz are shown in Figure 4.16.
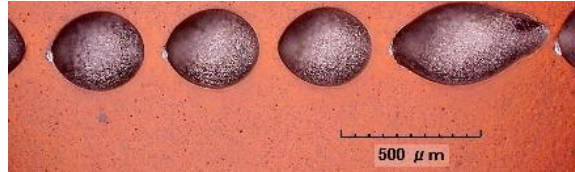
Figure 4.16: Discontinuous traces resulting from an overlap fraction of 0.1 and a jetting frequency of 125 Hz.

Straight Lines: As jetting moves to intermediate overlap fractions (i.e. 0.3 – 0.5) and low or medium frequency (i.e. ~75 Hz), the line quality improves substantially. Figure 4.17 illustrates a trace printed with a drop overlap fraction of 0.4 and a jetting frequency of 75 Hz. This trace can be noted to be straight and with a uniform line width. However, ridges corresponding to partially overlapping droplet are evident. A trace printed at a slightly higher drop overlap fraction of 0.7 and a jetting frequency of 75 Hz is shown in Figure 4.18.
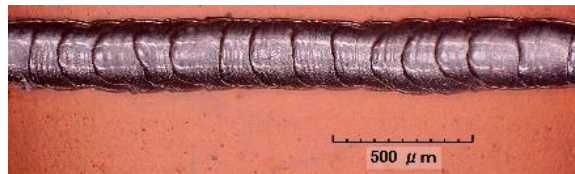
Figure 4.17: Straight trace resulting from an overlap fraction of 0.4 and a jetting frequency of 75 Hz.
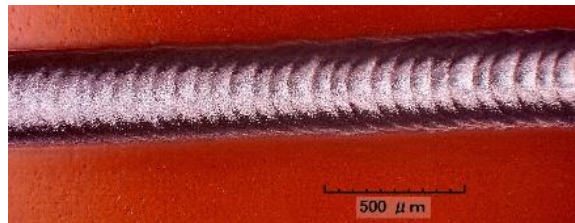
Figure 4.18: Straight trace resulting from an overlap fraction of 0.7 and a jetting frequency of 75 Hz.

Bulging Lines: When intermediate to high droplet overlap fractions (i.e. 0.5 – 0.7) are combined with intermediate jetting frequency (125 Hz), sufficient heat and material deposition is expected to result in the puddling and bulging of lines due to surface tension effects prior to solidification. A trace printed at a drop overlap fraction of 0.5 and a jetting frequency of 125 Hz is provided in Figure 4.19, showcasing this behavior.
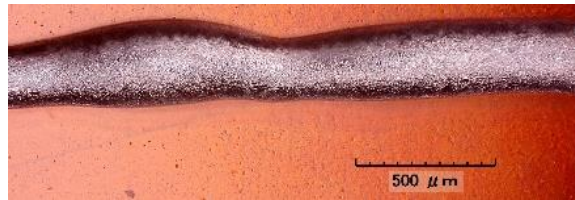
Figure 4.19: Bulging traces resulting from an overlap fraction of 0.5 and a jetting frequency of 125 Hz.

Figure 4.20 conceptually showcases a process map for each of these morphologies when considering overlap fraction and jetting frequency. However, it should be noted that these results are specific to 4043 aluminum alloy deposited at a temperature of 900 °C through a 250 µm diameter nozzle onto a 200 °C heated Kapton polyimide film. With different process parameter conditions and/or materials (e.g. molten copper or PET substrate), similar process parameter maps would be needed through experimental investigation. For example, the volume of each drop decreases as a function of the cubed root of the nozzle diameter with usage of smaller diameter nozzles. It is reasonable to expect that higher jetting frequencies will be needed for smaller drop volumes to obtain desired fusion between adjacent droplets for fabricating high quality conductive traces.
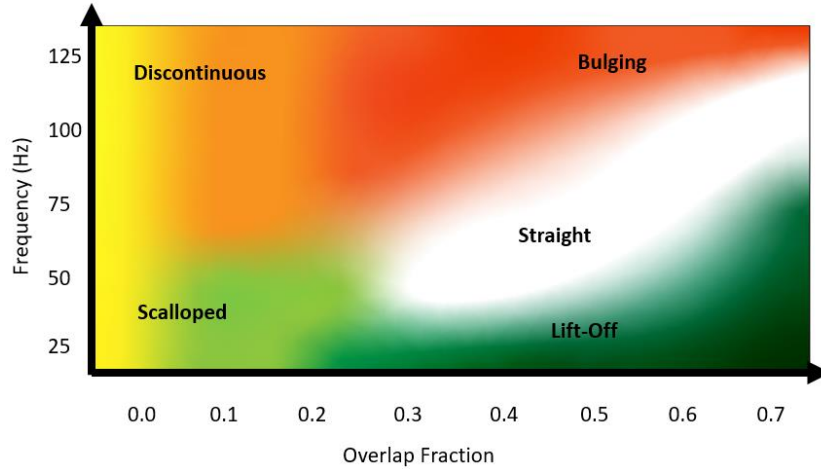
Figure 4.20: Process map for printed line behavior as a function of overlap fraction and frequency.

Equivalent wire gauge of uniform lines: Unlike printed electronic features fabricated through metal-based inks, traces printed via liquid metal droplet jetting produce very high aspect ratio conductive traces which have the capacity to carry high currents. The behavior of these printed traces would be similar to solid core wires. For high current carrying applications where in the user provides a wire gauge specification, mapping the cross-sectional area of printed traces to the cross-sectional area associated with standard wire gauges would be very useful.

To obtain an accurate estimate of the jetted drop diameter, a calibration routine is run prior to each print job where in 10000 drops are jetted into a weighing pan placed on a digital scale. The calibration mass (m_c) in grams per 10000 drops is then recorded. Using m_c with the density (ρ) of the metal alloy being deposited in g/cm^3, the volume (V_d) per drop in cm^3 can be calculated from Eq (5):

$$V_d = \frac{m_c}{10000\rho} \tag{5}$$

Equating the volume of a spherical droplet to the empirically measured drop volume V_d and solving for the diameter of the drop (D_d) in cm, we have Eq (6).

$$D_d = \left(\frac{6V_d}{\pi}\right)^{1/3}$$

(6)

The center-to-center distance between adjacent droplets deposited onto a substrate is typically referred to as drop spacing (d_s). In printing regimes that result in uniform traces, the volume of material deposited per unit length can be used to estimate the average cross-sectional area (A_t) of a printed trace in cm^2. This holds true regardless of the cross-sectional shape of the printed trace. Using V_d from Eq (5) and d_s from Eq (1), A_t is determined as Eq (7).

$$A_t = \frac{V_d}{d_s}$$

(7)

To obtain the axial cross-sectional area of printed traces, selected samples were mounted, ground and polished to reveal their horizontal cross-section. Figure 4.21 shows the straight-line cross-sections. It can be noted the cross sections resemble a truncated cylinder on the substrate. As expected, the cross-sectional area of printed traces increases with increase in overlap fraction.

(a)   (b)
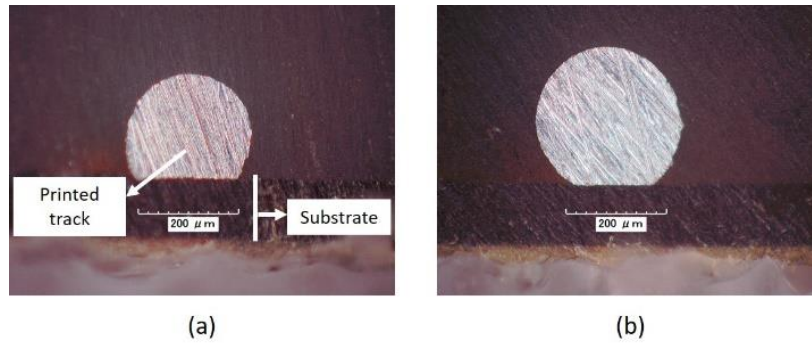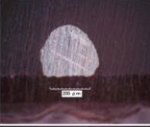
Figure 4.21: Axial cross-sections of uniform lines printed using (a) 0.40 overlap fraction 75 Hz frequency; (b) 0.60 overlap fraction and 100 Hz frequency.

The mass of 10000 droplets (m_c) jetted using a 250 µm diameter nozzle was measured before conducting the experiments by jetting the droplets into a weighing pan placed on a digital scale. The density of 4043 aluminum alloy is 2.69 g/cm^3. Using Eq (5), the volume per drop (V_d) was calculated as 6.5741 x 10^6 µm^3. This corresponds to a drop diameter of 232 µm, calculated through Eq (6). Using Eq (7) with V_d and considering the various drop spacing values used to print straight lines, the expected cross-sectional areas of printed traces produced using different drop spacing (d_s) values were computed. With cross-sectional images obtained for each drop spacing value, the actual cross-sectional areas of printed traces were measured using the area function in ImageJ software. Figure 4.21 shows predicted and measured cross-sectional areas of the straight traces printed at different overlap fractions. The estimated and measured cross sectional areas are rounded down to the nearest American Wire Gauge (AWG) cross sectional area for being conservative when estimating current carrying capability. From Figure 4.22, it can be noted that the predicted cross-sectional areas from Eq (7) are in reasonably good agreement with measured cross-sectional areas. Thus Eq (7) can be used as an indicator of the expected wire gauge for maximum current calculation purposes in high power electronics. It is notable that the height-to-width aspect ratio of the printed traces is 1-2 orders of magnitude greater than one would normally see with printed metal-based ink traces which are typically a few microns thick. The large aspect ratio highlights the potential to carry high currents in these printed traces.

Overlap Fraction	Frequency (Hz)	Horizontal cross-section Micrograph	Predicted X-Sectional Area (x10^{-2} mm²)	Measured X-Sectional Area (x10^{-2} mm²)	Nearest AWG for Predicted Area	Nearest AWG for Measured Area
0.4	75		4.76	4.55	31	31
0.5	75		5.72	5.72	30	30
0.6	100		7.14	6.52	29	29
0.7	100		9.53	10.06	28	28

American Wire Gauge	Area (x10^{-2} mm²)
31	4.04
30	5.09
29	6.42
28	8.10

Figure 4.22: Wire gauge predicted and measured through the volume of droplet over drop spacing formulation.

This study showed the feasibility of fabricating uniform features on polymer substrates using the molten metal droplet jetting approach. The process conditions of overlap percentage and deposition frequency were noted to have a significant impact on the morphology of the printed traces. At low deposition frequencies, the printed traces transitioned from a scalloped line to a wave-like morphology with an increase in overlap fraction. At high deposition frequencies, the isolated droplets were noted to transition into pairs and then into bulging traces as the overlap increases. Intermediate deposition frequency and overlap conditions were identified to be suitable for printing uniform lines. A simple formulation that considers the volume of individual deposited droplets and drop spacing between adjacent droplets is suggested and validated to predict the equivalent wire gauge of the uniform printed traces. This could be useful for knowing the current carrying capabilities of the printed features in high power electronics applications.

4.4 Summary

Electrically conductive traces are a major part of almost all electronic devices. It is highly desirable to fabricate uniform, smooth traces of fine resolution so as to meet the high standards of the electronics industry. The goal of the three studies presented in this chapter was to understand the process conditions that would help in achieving high resolution, uniform, and smooth printed traces with a given nozzle size. Furthermore, the studies would also indicate the capabilities of the molten metal jetting process in fabricating high quality printed traces.

The first study showcased the impact of several key process conditions on the diameter of the deposited droplets. The goal of the study was to identify process conditions that would lead to the finest resolution droplets with minimal deviation in the size of deposited droplets. This would be important in achieving uniform and smooth printed traces. Using a full factorial design of experiments approach, we identified the process conditions that would lead to the finest droplet resolution with minimal deviation in drop diameter for a 250μm diameter nozzle size.

The second study presented in this chapter discussed the impact of various key process conditions on the surface roughness of the printed traces. Based on the insights gathered from the prior study on droplet diameter, the factors of substrate temperature, ejection frequency and droplet overlap fraction were chosen to be modified in the study. A full factorial design of experiments approach was employed. This study indicated that it is feasible to fabricate traces with R_q surface roughness values in the range of 5μm. The typical R_q values for standard copper foils used in printed circuit boards is typically about 2μm. This indicated the potential of molten metal jetting to fabricate features whose surface roughness values are reasonably close to those of features currently being employed in functional printed circuit boards.

The third study presented in this chapter discussed the impact of droplet overlap fraction and droplet ejection frequency on the uniformity of deposited traces. Five distinctly different regimes were observed, and a process map showcasing the conditions that would lead to uniform printed features was presented. A

simple formulation to predict the equivalent wire gauge of the uniform printed traces was presented and validated by taking the volume of individual deposited droplets and drop spacing into consideration. This formula could be useful for knowing the droplet overlap fraction and droplet deposition frequency conditions that would help in fabricating a uniform printed trace of desired wire gauge.

Chapter 5: Evaluation of electrical and mechanical performance

5.1 Pinhole formation in deposited droplets

Air entrapment inside deposited droplets after impingement onto a solid substrate is a very well-documented issue which has been studied theoretically and experimentally since the early 1990's [137-140]. The current scientific consensus about the phenomenon is that a creeping flow of a thin gas layer between the bottom of the droplet and the solid surface is formed immediately prior to the droplet impact [138, 141-146]. Gas buildup leads to a deformation in the liquid droplet, and the gas layer gets entrapped by a circular contact line. As the droplet recoils, the contact line contracts, and the trapped gas takes the shape of a bubble. When solidification of the droplets is also a part of the impingement process, the trapped bubbles in the solidified droplets are generally referred as pinholes. Figure 5.1 provides an illustration of the bubble evolution in the droplet during impact and formation of a pinhole.
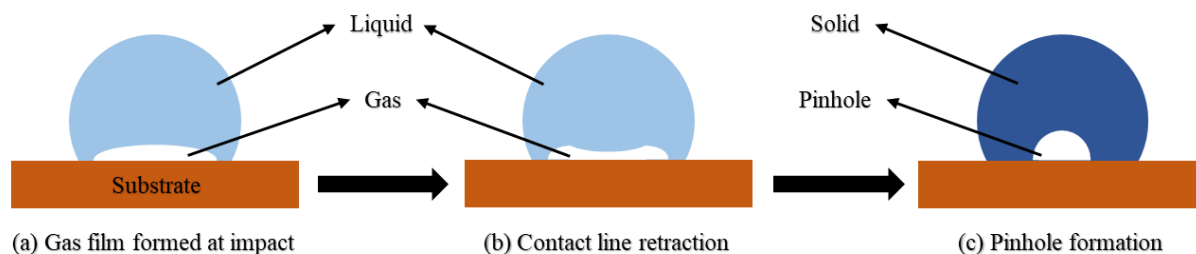
Figure 5.1: Schematic of bubble evolution during droplet impact.

Relatively few publications have explored gas entrapment when solidification is involved, such as studies involving low Weber numbers [147], thermal spray forming [148] and nano pore formation [149]. Qu *et al*. investigated the formation mechanism of nano scale bubbles in nickel droplets deposited onto stainless steel substrates [149]. They interpreted the pinhole evolution as entrapment of gas during the impingement

process and subsequent freezing to a porous solid [149]. Work done by Yi *et al.* has demonstrated that the surface roughness of the substrate and the size of the droplet has a significant influence not only on the size but also on the number of pinholes formed in aluminum molten metal droplets deposited on a room temperature brass substrate [150]. Xiong *et al.* discuss a numerical investigation of air entrapment when a molten droplet impacts and solidifies on a cold and smooth substrate using the 3D lattice Boltzmann method [146]. They showcased that the trapped gas pocket could form either a single air bubble or multiple air bubbles depending on the surface wettability of the substrate. Numerical modelling studies done by Shukla *et al.* demonstrated the effect of wettability of the substrate on pinhole formation after molten metal droplet impingement and solidification [151, 152]. Research on the observation of air pockets inside droplets deposited onto polymeric surfaces has been limited to liquids that do not undergo a phase change from liquid to solid [153]. To the best of our knowledge, there have not yet been published studies that investigated the pinhole formation in molten metal droplets deposited onto polymer substrates.

The presence of pinholes could be detrimental to the performance of printed flexible electronic features. This is because the pinholes would serve as stress concentrators and increase the chance of failure when the features are subjected to bending. In this study, we report the observation of significantly large pinholes in printed aluminum traces deposited on polyimide (PI) substrates for the purpose of fabricating flexible electronic devices. The two major aims of this study, therefore, are (1) to present a hypothesis that explains the pinhole formation mechanism when high temperature molten metal drops are deposited onto polyimide substrates, and (2) to find approaches for reducing or eliminating these large pinholes in printed conductive traces.

In this experimental study, the melt pool temperature was set at 850 °C for printing all the samples. The orifice size employed in the experiments was 500 μm, hence the diameter of ejected droplets was approximately 500 μm. To investigate the presence of pinholes, we chose to observe the cross-sectional view of the printed droplets from the side and the bottom as illustrated in Figure 5.2. To obtain the cross-sectional images of the printed droplets, the printed samples were placed at the bottom of a mold and a

mixture of a resin and hardener in the ratio of 10:1 was poured into the mold. The mixture of resin and hardener was left to solidify overnight. To observe the pinholes from the side view, a Struers grinding and polishing tool was used to grind the metal droplets that are now embedded in the solidified resin and hardener mixture, until approximately the halfway point from the side of the droplet was reached. To observe the pinholes from the bottom, the samples were ground and polished until the substrate was removed, and the bottom of the solidified metal droplet was exposed. A Hirox microscope was used to observe the microstructure of the droplet cross section.
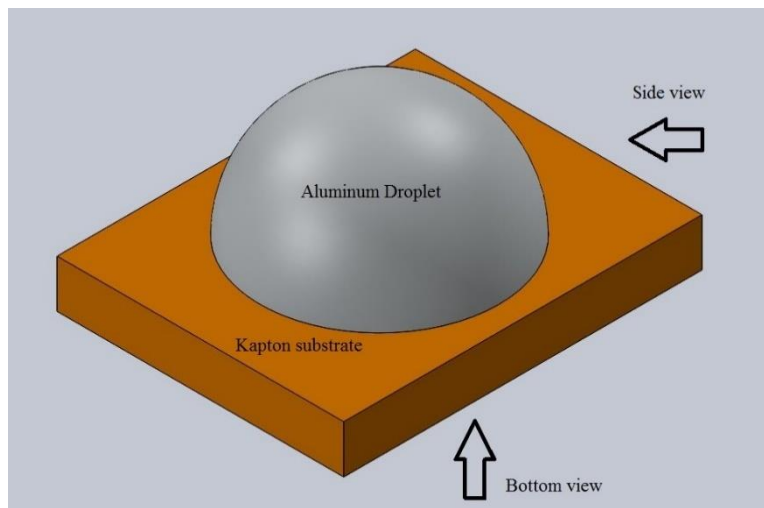
Figure 5.2: Illustration of the aluminum droplet on Kapton substrate.

Figure 5.3 shows micrographs of the bottom and side cross sections of solidified Al4043 droplets deposited onto a Kapton substrate. The presence of multiple pinholes can be clearly observed from the micrographs. The side view also shows the presence of a considerably large pinhole. Surface profiles of the cross sections were taken using a Nanovea white light interferometry profilometer. The surface profiles confirmed that the observed features inside the solidified metal droplets are indeed voids.

Figure 5.3: (a) Bottom view of a printed droplet (b) Side view of the droplet cross-section. Scale bar = 250 µm.

The approximate diameter of a pinhole was measured using a Hirox KH-7700 optical microscope as illustrated in Figure 5.4. The diameter of the pinhole was approximately 245 µm for a 500 µm diameter droplet. The pinhole size was also highly reproducible from numerous samples printed at similar experimental conditions.
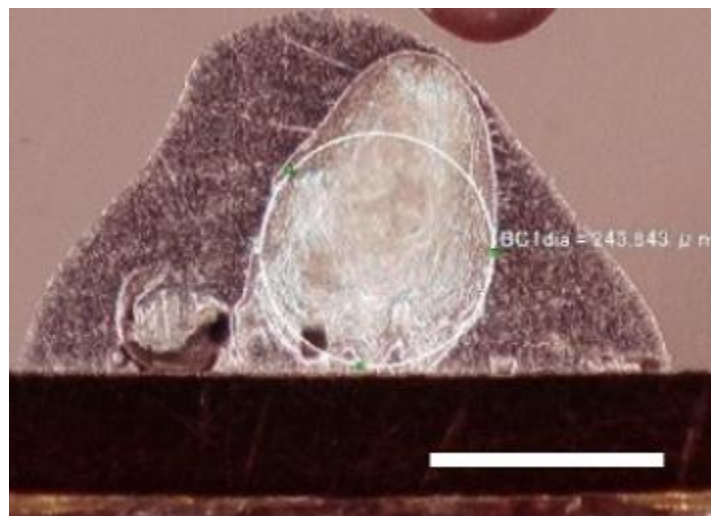
Figure 5.4: Approximate 245 µm diameter of a pinhole being measured on a Hirox microscope. Scale bar = 250 µm.

Yi *et al.* studied the impact of surface roughness of the substrate on pinhole formation when molten aluminum droplets were deposited onto a brass substrate [150]. Based on their experimental observations, they proposed a mathematical formulation to predict the size of a pinhole that could form in a molten metal droplet after impingement and solidification onto a solid substrate. Eq (8) predicts the radius of the pinhole (R_p) by considering the gas dynamic viscosity (μ_g) of the gas surrounding the droplet, surface tension of the droplet (σ), the droplet radius before impact (R), the liquid mass density (ρ_l), and Stokes number defined by $S_t = \rho_l R U / \mu_g$, wherein (U) is the droplet impact velocity.

$$R_p \sim R \left(\frac{\mu_g^2}{\sigma \rho_l R} S_t \right)^{1/3} \qquad (8)$$

For the experimental conditions used in this study, R = 250 μm, ρ_l = 2700 kg.m^{-3} and U =1 – 10 m/s [154, 155]. The gas dynamic viscosity μ_g = 5.04 x 10^{-5} Pa.s., and surface tension σ = 0.77 N/m. These values were considered based on the assumption that the temperature of the argon gas surrounding the droplet is approximately 700 °C [156, 157]. Substituting these values in Eq. (8), the predicted radius of pinholes in the droplet impact velocity range of 1-10 m/s is calculated to be in the range of 10-22 μm. However, the measured value of the pinhole radius in our case was ~122 μm. Hence Yi *et al.*'s formulation does not adequately explain the formation of the large pinholes in our current study in which molten metal drops are jetted onto a polymeric, rather than metallic, substrate.

An experimental study was devised to identify the most likely process conditions which could contribute to formation of the large pinholes. The droplet temperature, substrate temperature and frequency were chosen as the process conditions that would be investigated. These factors were chosen based on some evidence gathered from screening experiments and on published literature [146, 150]. Three levels of each of the factors was chosen. The response variable was the approximate diameter of the largest pinhole

measured from the side view of the cross-sectional image. A 500 μm diameter nozzle orifice was used in the experimental studies. The Hirox digital microscope was used to measure the diameter of the pinholes. The process of measuring the pinhole size is illustrated in Figure 5.4. The factors employed and their chosen levels are provided in Table 5.1.

Table 5.1: Factors and levels used for pinhole diameter DOE.

Factor	Definition	Levels		
		Level 1	Level 2	Level 3
Droplet temperature	Temperature of the molten metal in the print head	800°C	850°C	900°C
Substrate temperature	This is the temperature of the substrate during the printing process	25°C	75°C	150°C
Frequency	This is the frequency of the ejected droplets	50Hz	100Hz	200Hz

A full factorial design of experiments with was employed to determine the effects of ejection frequency, droplet temperature and substrate temperature on the diameter of the pinholes in the deposited droplets. Three measurements were chosen at each experimental condition. The full factorial design was analyzed using MINITAB 18 statistical analysis software. Table 5.2 shows the analysis of variance.

Table 5.2: ANOVA for the pinhole diameter.

Analysis of Variance

Source	DF	Adj SS	Adj MS	F-Value	P-Value
Model	26	628454	24171	189.79	0.000
Linear	6	626905	104484	820.40	0.000
Droplet temperature	2	95	47	0.37	0.692
Substrate temperature	2	626764	313382	2460.64	0.000
Frequency	2	47	23	0.18	0.833
2-Way Interactions	12	668	56	0.44	0.941
Droplet temperature*Substrate temperature	4	184	46	0.36	0.835
Droplet temperature*Frequency	4	382	96	0.75	0.562
Substrate temperature*Frequency	4	102	26	0.20	0.937
3-Way Interactions	8	880	110	0.86	0.552
Droplet temperature*Substrate temperature*Frequency	8	880	110	0.86	0.552
Error	54	6877	127		
Total	80	635331			

Model Summary

S	R-sq	R-sq(adj)	R-sq(pred)
11.2853	98.92%	98.40%	97.56%

At a 95% confidence interval, it can be observed from the ANOVA that the substrate temperature is the only factor that has a significant impact on the pinhole diameter, as it's P-value is < 0.05. The rest of the factors as well as the two- and three-way interactions can be noted to have no significant impact on the pinhole diameter at a 95% confidence interval. The Pareto chart shown in Figure 5.5 illustrates this effect, as only the substrate temperature is shown to be significant.
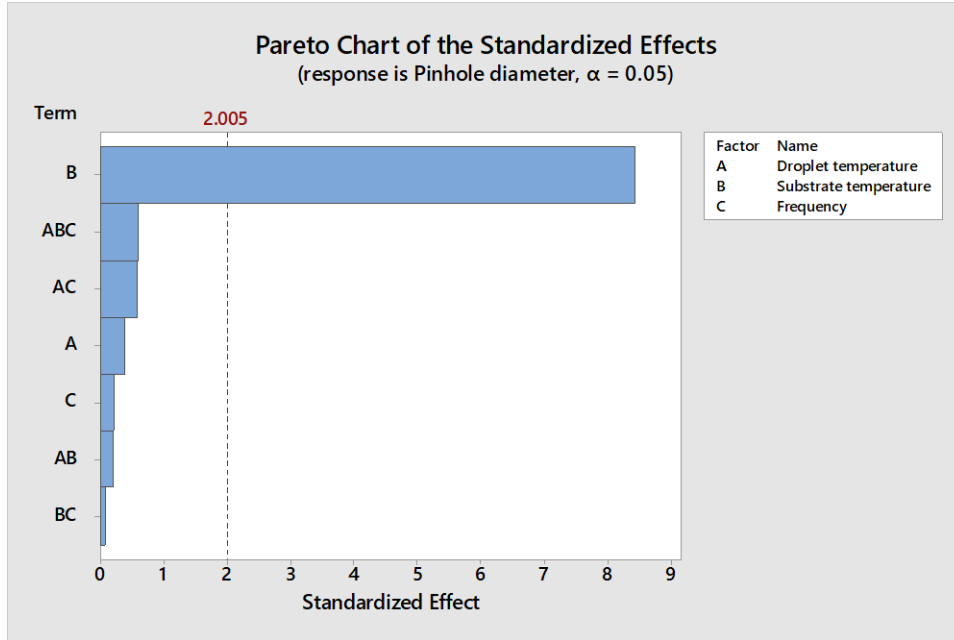
Figure 5.5: Pareto chart of the standardized effects for pinhole diameter.

The experimental investigation showcased that the size of the pinholes can be reduced considerably when droplets are deposited onto heated substrates rather than room temperature substrates. Figure 5.6 and Figure 5.7 show side and bottom views of droplets printed on polyimide substrates which were at temperatures of 25 °C, and 150 °C respectively. The size of the pinholes is dramatically smaller when the droplets are deposited onto the heated substrate. The average radius of the pinholes in droplets deposited onto heated polyimide substrate was ~ 22 μm. This lies within the range of pinhole diameter that is predicted by the formulation in Eq (8) suggested by Yi *et al*. [150]
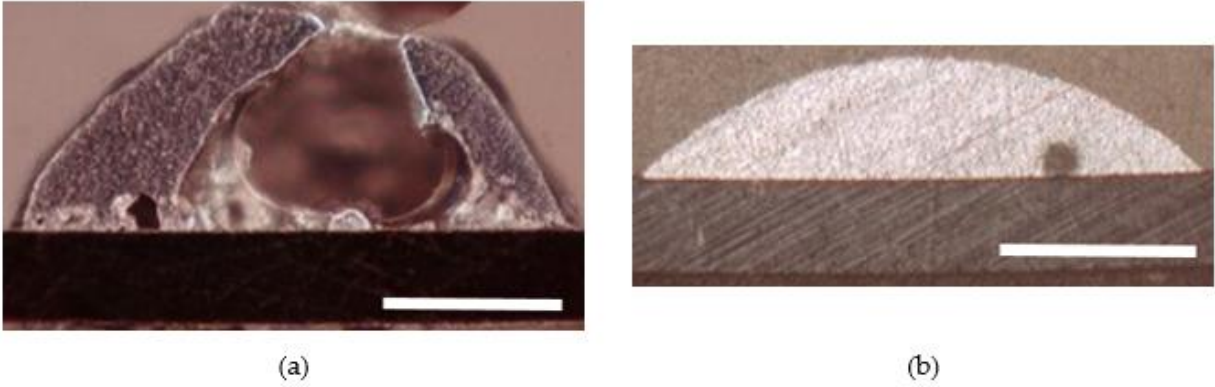
Figure 5.6: Side view of the deposited droplet printed at substrate temperature of (a) 25 ℃, (b) 150 ℃. Scale bar = 250 µm.
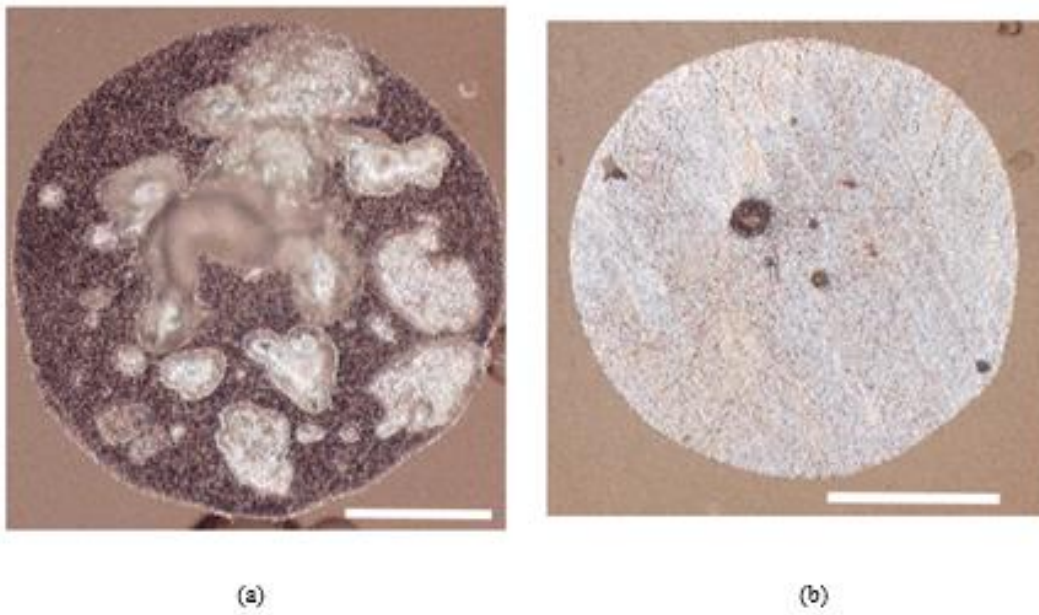
Figure 5.7: Bottom view of the deposited droplet printed at substrate temperature of (a) 25 ℃, (b) 150 ℃. Scale bar = 250 µm.

We hypothesize that the presence of significantly larger pinholes in droplets deposited on room temperature substrates is due to the release of absorbed moisture from the substrate into the solidifying droplet. Polyimide is a hygroscopic material with a moisture absorption percentage of 1.8% at 50% RH and 23 °C [158]. As liquid aluminum droplets land on the polyimide substrate, the temperature of the substrate is expected to increase beyond the boiling point of water. This most likely leads to the absorbed moisture in

the polyimide to vaporize. The large pinholes are expected to form as the droplet solidifies around the water vapor escaping from the substrate.

When the substrate is heated to 150 °C, the absorbed moisture is removed from the substrate due to the heating process. Haghighi *et al.* have shown that heating Kapton HN beyond 100 °C for a few minutes can remove a significant portion of absorbed moisture [159]. Any pinholes formed when droplets are deposited onto the heated substrate are most likely due to the entrapment of surrounding gas beneath the impinging droplet as proposed by earlier studies on air bubble entrapment [141-143]. The size of the pinholes observed when droplets are deposited onto the heated substrates also correlates well with the size of pinholes observed when metal droplets are deposited onto metallic substrates. This further corroborates the hypothesis.

The effectiveness of pre-drying the substrate to remove the moisture and possibly reduce the pinhole size was tested in a follow-up experiment by printing onto a pre-dried substrate without substrate heating. Kapton HN polyimide substrate was dried in a vacuum oven for 12 hours at 250 °C to remove any absorbed moisture. Droplets of aluminum alloy at 850 °C were deposited on the dried substrate which was placed on the unheated print bed. Figure 5.8 shows the pinholes when droplets were directly deposited onto undried and dried polyimide substrates, respectively. Interestingly, pinholes in droplets deposited onto the pre-dried substrates were comparable in size to the pinholes in the undried substrate.
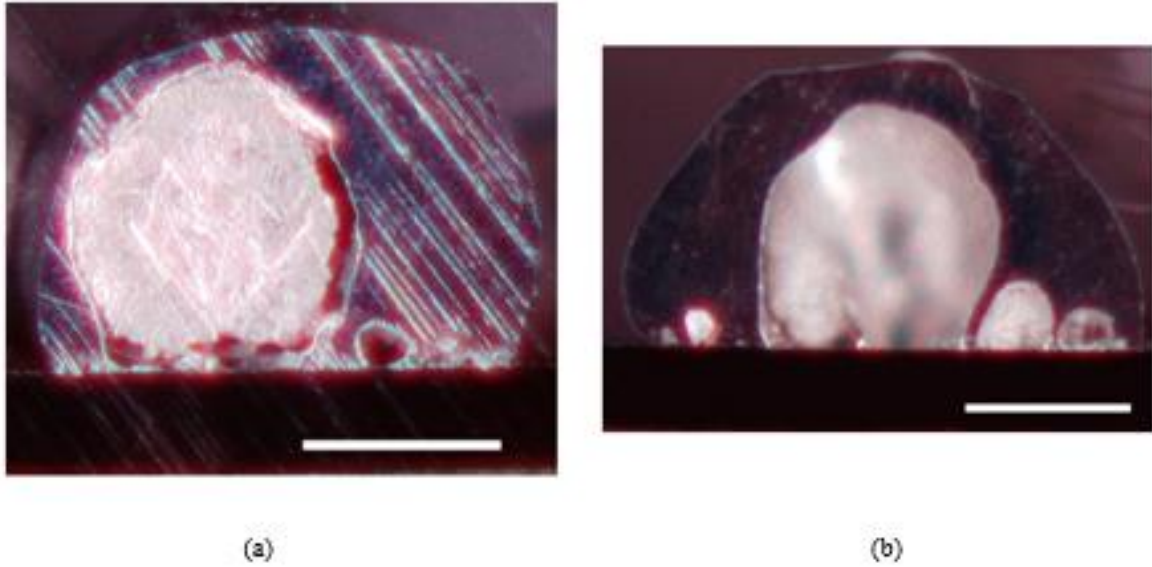
Figure 5.8: Pinholes in (a) undried and (b) dried substrate. Scale bar = 250 μm.

Studies by Yang *et al.* and Akram *et al.* have shown that dried polyimide exposed to atmospheric conditions can adsorb atmospheric moisture at a fast rate [160, 161]. In our case, the dried polyimide substrate was transported from the vacuum oven to the printer in a desiccator with desiccant in it. However, there was a delay of ~15 minutes between the time the dried substrates were mounted on the printing platform in the printer and the time the droplets were deposited. During this time, the substrates were exposed to open atmosphere. To assess the amount of moisture that might be gained during that time span, the masses of 10 polyimide samples were measured immediately after drying. The same samples were then weighed after 15 minutes of exposure to open atmosphere. The mass of the samples increased by an average of 0.6% after 15 minutes of exposure to open atmosphere. The presence of pinholes in dried substrates could therefore be explained by the likelihood of atmospheric moisture being reabsorbed onto/into the substrates between drying and printing. This study highlights the importance of substrate heating with hygroscopic substrates.

After the experiments involving the interaction of individual droplets with heated and unheated substrates, continuous linear electronic traces were printed onto unheated and heated polyimide substrates at a

deposition frequency of 40 Hz and drop spacing of 300 μm to investigate the presence of pinholes in printed traces. Figure 5.9 shows the cross-sectional images of linear traces printed onto unheated (~25 °C) and heated (150 °C) substrates. Compared to the unheated substrate, there are far fewer pinholes in the traces printed on the heated substrate. Also the pinholes in the heated substrate are much smaller in size. The thickness of trace printed on the heated substrate is also considerably smaller than the thickness of the trace printed on the unheated substrate. Both traces were printed at identical jetting parameters and therefore have the same volume of metal per unit length. However, the large pinholes in traces printed on the unheated substrate occupy considerable volume and therefore greatly increase the overall height of the traces.

(a)   (b)
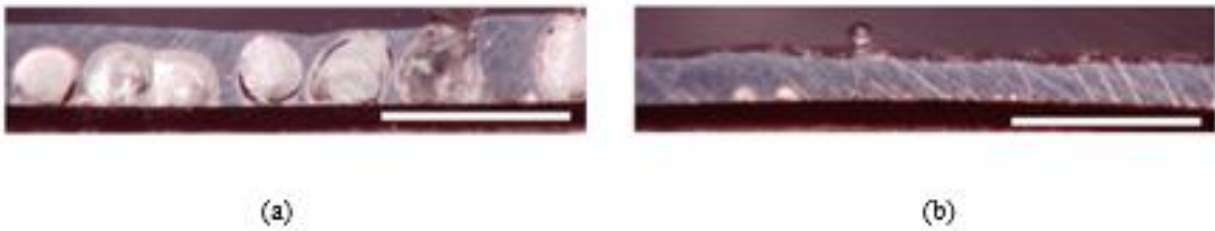
Figure 5.9: Longitudinal cross-section of tracks printed on substrate at (a) 25 ℃ (b) 150 ℃. Scale bar = 1000 μm.

As the printed features are intended to be used in printed flexible electronics, minimization of pinhole quantity and size is highly desirable. Lack of pinholes could improve adhesion of the printed traces to the substrate due to the higher contact area of the metal with the substrate. The presence of pinholes can also make printed traces highly prone to crack formation around the pinholes when the substrate is flexed. Smaller pinholes can greatly improve the performance of the printed features when they are subjected to bending due to the reduced number of regions where crack propagation could initiate. However, no significant variation in electrical resistivity was noticed between the samples with and without pinholes. This is most likely because the amount of aluminum is same in both the tracks with and without pinholes.

This study has shown the presence of large pinholes when droplets of molten aluminum were deposited onto room temperature polyimide substrates. The formation mechanism behind the pinholes was

hypothesized to be the release of absorbed moisture from the polyimide into the solidifying droplet. Heating of the substrate above the boiling point of water was shown to dramatically reduce the number and size of pinholes due to the removal of absorbed moisture through the heating process. However, depositing molten metal droplets onto a pre-dried substrate is not recommended if the substrate is exposed to open atmosphere for a period after drying, as there is a chance of reabsorption of moisture. Employing high performance polymers with low moisture absorption coefficients could be a potential way of reducing the size of pinholes when molten metal jetting is used for printed electronics applications. Substrate heating to beyond 100 °C is shown to be an effective approach for reducing the quantity and size of pinholes.

5.2 Characterization of electrical conductivity and adhesion of printed traces

As the printed features are intended to be employed as functional electronic circuits, it is crucial to characterize their electrical and adhesive performance. Uniform traces printed at the appropriate conditions identified in the previous section were ground and polished parallel to their longitudinal axes to check for any defects that might affect electrical conductivity. Figure 5.10(a) shows the longitudinal cross-section of a trace printed at a frequency of 100 Hz and an overlap fraction of 0.60. A radiograph shown in Figure 5.10 (b) indicates continuous material that is free of pores or other discontinuities.
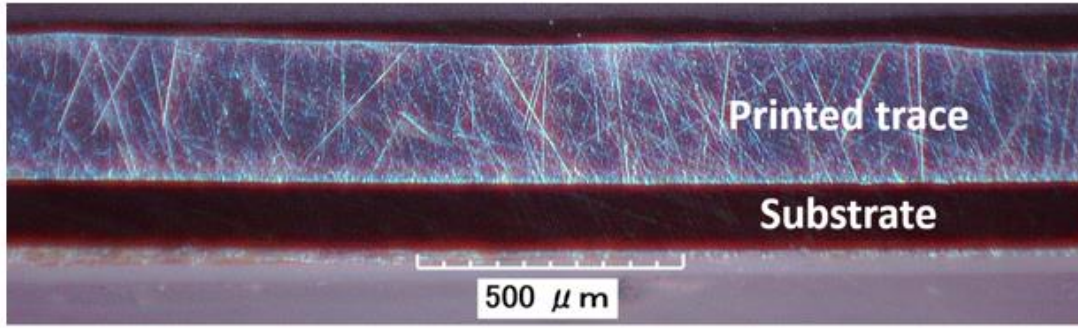
(a)
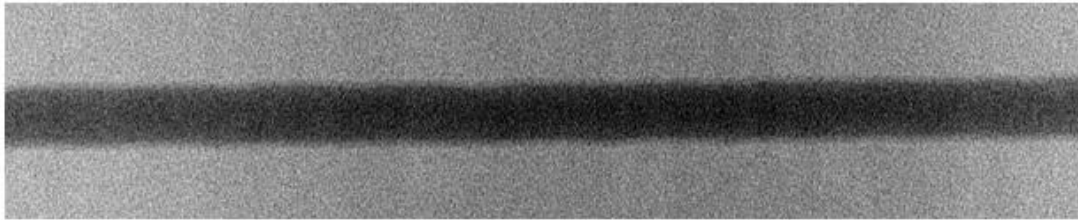
(b)

Figure 5.10: (a) Longitudinal cross-section of a uniform printed line printed at 0.60 overlap fraction and 100 Hz frequency; (b) radiograph of printed trace showing dense material.

A 4-point conductivity measurement approach as shown in Figure 5.11 was employed to characterize the electrical conductivity of the printed traces. A current of 6A was passed through the printed traces over a path length of 10 mm, and the voltage was measured using a multimeter. The resistivity of the tracks was calculated using Eq (9)

$$\rho = \frac{R.A}{L} \tag{9}$$

where ρ is the electrical resistivity, R is the electrical resistance, A is the cross-sectional area of the printed trace, and L is the length of the measured conductive line.
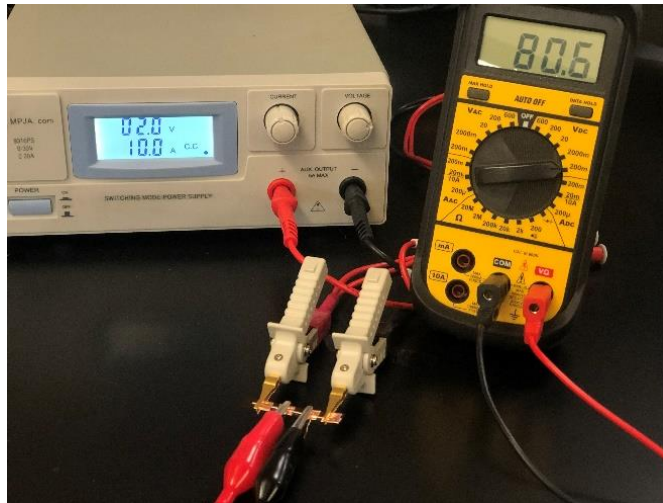
Figure 5.11: 4-point probe conductivity test in which a constant current is being passed through a printed trace.

As the longitudinal cross-section of the traces revealed no significant porosity, the cross-sectional areas of the printed traces were determined from the micrographs shown in Figure 4.22. The resistivity of the aluminum wire feedstock material used for printing was measured to be 4.178 µΩ-cm using the 4-point probe approach. This value was used as the baseline bulk metal electrical resistivity for comparison with electrical resistivities of the printed traces. Table 5.3 shows the electrical resistivity values of uniform traces printed at eight different combinations of overlap fraction and jetting frequency. The resistivity of the printed traces relative to the resistivity of the bulk metal used for printing is shown in the final column in Table 5.3. The electrical resistivity values ranged from 1.07 to 1.23 times the resistivity of the bulk metal. These results indicate that MMJ processes can achieve near bulk conductivity over a reasonably wide range of processing conditions. It is also notable that the large cross-sectional area and high electrical conductivity of the printed traces enables them to carry significantly higher current than would normally be the case with metal nanoparticle printed traces. This indicates that these features could be very well suited for high power electronics.

Overlap Fraction	Jetting Frequency (Hz)	Applied Current (A)	Measured Voltage (mV)	Measured Resistance (mΩ)	Measured Cross Sectional Area (μm²x10⁴)	Computed Resistivity (μΩ-cm)	Resistivity Relative to Bulk Metal
0.30	50	6	78	13.0	3.655	4.753	1.13x
0.30	75	6	61	10.1	4.416	4.490	1.07x
0.40	75	6	67	11.2	4.547	5.078	1.22x
0.50	75	6	50	8.3	5.438	4.532	1.08x
0.50	100	6	54	9.0	5.717	5.145	1.23x
0.60	75	6	45	7.5	6.273	4.704	1.12x
0.60	100	6	41	6.8	6.524	4.458	1.07x
0.70	100	6	28	4.7	10.206	4.763	1.14x

The adhesion of the printed traces onto polyimide substrates was measured using a standard tape test commonly used for characterizing adhesion of nanoparticle based printed electronics. Pressure sensitive tape was firmly attached to the printed area and was then removed quickly. The dashed rectangle Figure 5.12 (a) shows the pressure sensitive tape while it was attached to the printed traces. The completeness of the printed feature after the removal of the tape – as shown in Figure 5.12 (b) - indicates good adhesion to PI substrate.

(a)   (b)
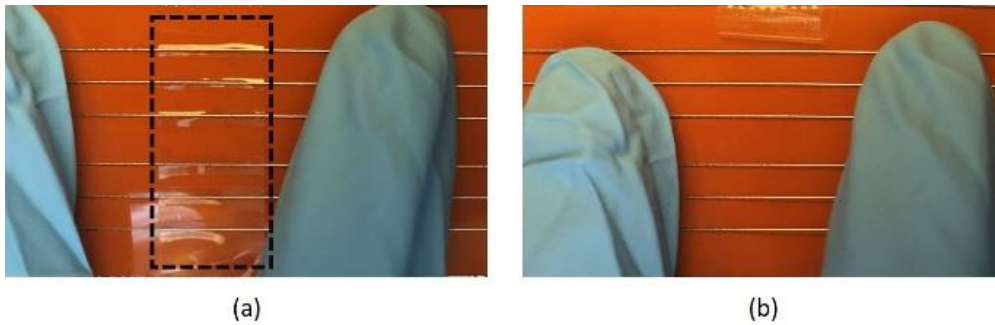
Figure 5.12: Tape test for testing the printed line adhesion on PI substrate (a) with the tape attached and (b) tape removed.

A uniform trace printed at an overlap fraction of 0.6 and jetting frequency of 100 Hz was bent on a mandrel with a radius of 20 mm. Electrical resistance of the trace was measured using a 2-point probe approach

before the sample was bent and when the sample was in the bent state on the mandrel. The experimental setup is shown in Figure 5.13. No change in electrical resistance was observed as the sample was flexed over the mandrel.
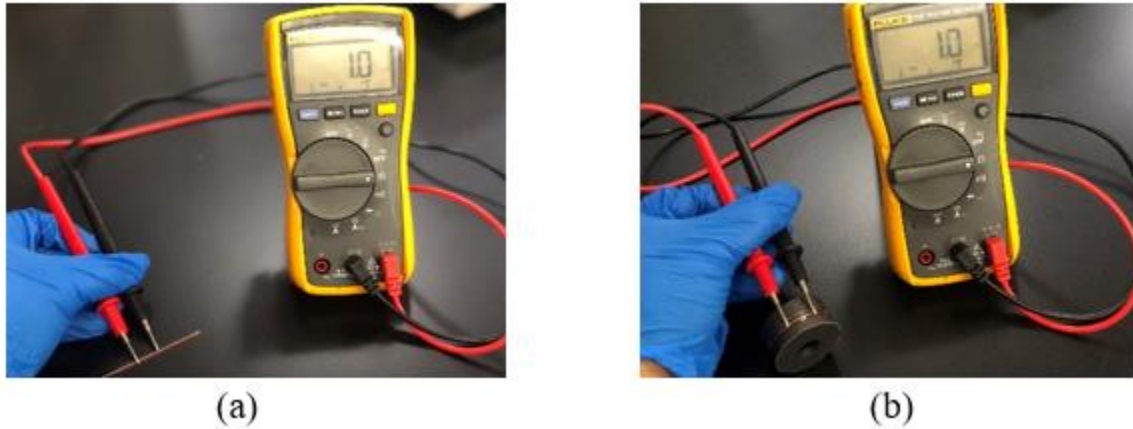
Figure 5.13: (a) 2-point probe conductivity measurement on an as-printed flat sample; (b) conductivity of sample bent over a mandrel with a 20 mm radius.

Visually inspecting the samples flexed over the 20 mm radius mandrel indicated no delamination of the printed trace anywhere along its length. This indicates that the printed traces behave very much like a ductile solid core wire. Longitudinal cross-sections of an unflexed trace and a trace that was bent over the 20 mm radius mandrel were prepared to assess whether or not any micro cracks or local delamination could be detected. The longitudinal cross-sectional micrographs are shown in Figure 5.14. No macroscopic cracks were noted in the trace after bending. Furthermore, no delamination of the trace from the substrate was detected.
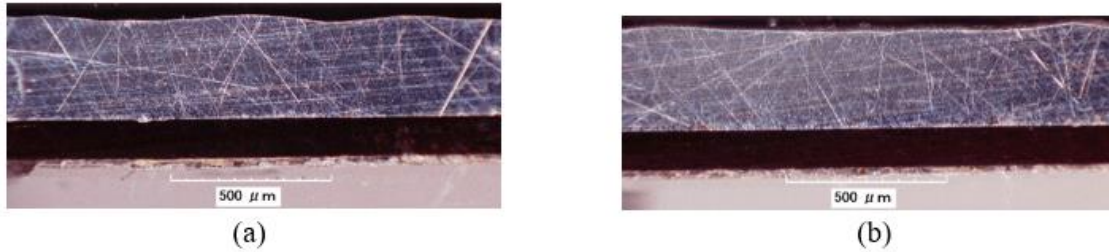
Figure 5.14: Longitudinal cross section of (a) a trace that has not been flexed, and (b) a trace that has been flexed on a mandrel of 20 mm radius. Both traces were printed with an overlap fraction of 0.6 and a jetting frequency of 100 Hz.

Based on the characterizations performed in this section, it can be noted that the traces printed at suitable process conditions demonstrated excellent electrical conductivity and adhesion to polyimide substrate. The characterization studies demonstrate the feasibility of employing MMJ processes in fabricating functional electronic traces. Given the large cross-sectional area and high conductivity of the printed traces, this process is ideally suited for high power electronics applications wherein large currents must be carried. Examples could include power distribution, solar panel bus bars, and certain antenna applications.

5.3 Effects of bending fatigue on electrical performance of printed features.

The implementation of the features fabricated using an MMJ process in functional applications necessitates the study of the fatigue behavior of printed traces. As the field of printed flexible electronics is still in its infancy, there are currently few standardized flexibility tests for evaluating the electrical performance of flexible electronics when they are subjected to bending fatigue. Several conceptually different bending tests have been proposed by different groups [162-168]. Research related to fatigue testing of electrical features of printed electronics to date has been extensively focused on metal-based inks [162-168]. In this study, we investigated the change in electrical resistance of uniform traces printed on polyimide substrates as a

function of the number of bending fatigue cycles. We employed an in-house built variable angle test setup for performing tensile, compressive, and full bending at various predefined radii of curvature.

Bending fatigue tests are typically done using a push-to-flex apparatus where lateral movement is used to induce bending in the sample [164, 165, 167, 169]. However the bending in this approach is unguided and unidirectional, so both tensile and compression bending tests cannot be done simultaneously. The other widely employed approach is to bend the samples on cylinders to provide a controlled bending radius and allow for simultaneous execution of tensile and compressive testing [168]. However the deposited conductive feature comes into contact with the cylinder during compression and could potentially damage the feature. Variable angle test setups have been explored to incorporate tensile/compressive bending simultaneously [170-172]. These setups also enable the bending test to be conducted without the need for bending the printed feature on a mandrel thereby avoiding any additional force on the sample.

In this study, we chose to evaluate the electrical performance of printed features subjected to bending fatigue through a variable angle bending test apparatus. Although variable angle bending testers are commercially available, they tend to be relatively expensive. A variable angle bending test setup was therefore built completely in house. The test setup is shown in Figure 5.15. The test samples are fastened to the setup using clamps on either side. The clamps are mounted onto 3D printed arms. The right arm is in a fixed position and the left arm is mounted on the shaft of a stepper motor. Using the horizontal plane as reference, the left arm can be rotated in a circular arc from -90$^\text{o}$ to +90$^\text{o}$ using a stepper motor (RB-SOY-03; 12V 0.4A unipolar stepper motor). The stepper motor is driven by a motor driver (L298N motor drive controller board module dual H bridge) and controlled by a microcontroller (Arduino Mega 2560 microcontroller). The minimum rotational resolution of the setup is 1.8°, as the stepper motor in the current setup uses 200 steps per rotation.
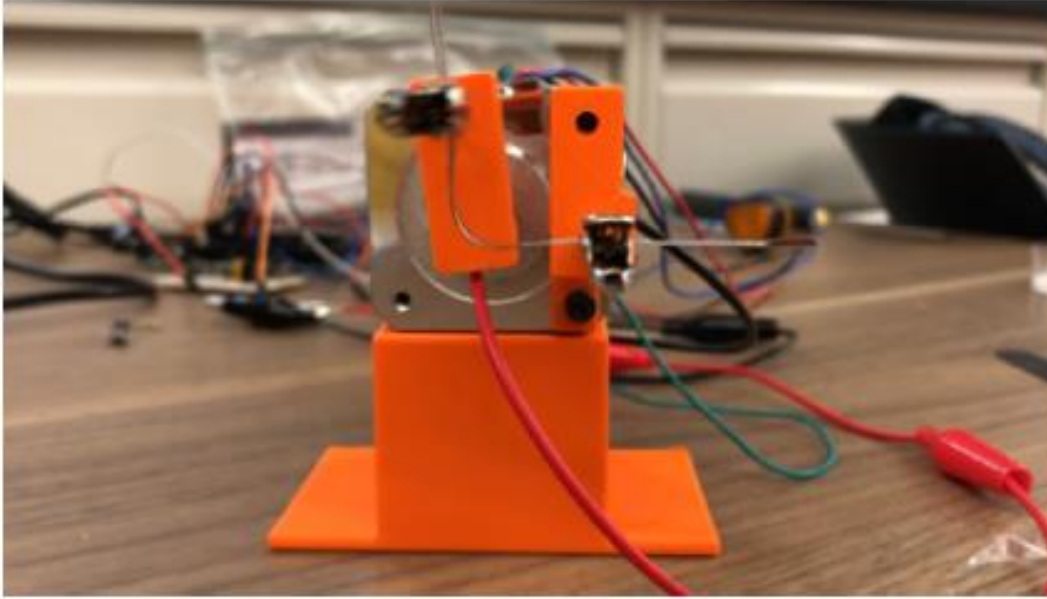
Figure 5.15: The variable angle test setup with a fixed arm on the right side and rotatable arm on the left side.

The angle of rotation and the distance between the clamps determines the radius of curvature at the apex of the test sample. Huber *et al.* proposed the following formula shown in Eq (10) to derive the bending radius at the apex for a particular bending angle and the length of the feature subjected to bending [171].

$$r(\beta) = \frac{L}{2\pi \sqrt{\left(1 - sin\left(\frac{180° - |\beta|}{2}\right)\right) - \frac{\pi^2 d^2}{12L^2}}} \tag{10}$$

In this equation, *r(β)* is the bending radius at the neutral axis of the test feature when it's subjected to an angle of rotation *β*. The angle of rotation *β* is positive for tensile loading on the printed trace and negative for compressive deformation. *L* is the length of the feature subjected to bending. *d* is the thickness of the feature being bent. For all tests performed in this study, we have employed a bending radius of 10 mm. This was chosen because a 10 mm bending radius is a reasonable benchmark for most flexible electronics

applications. Uniform traces were printed using an overlap fraction of 0.7, a frequency of 100Hz, a substrate temperature of 200 °C, and a 250 μm nozzle orifice diameter on a 125μm thick polyimide substrate. The thickness of the entire feature (d), i.e. the trace + substrate thickness, measured using an optical microscope was approximately 425μm as most of the traces printed at the conditions were ~300μm thick. As the features are bent from -90° to +90° in the setup, the angle of rotation (β) is 90°. To obtain a bending radius ($r(\beta)$) of 10mm, the length of the feature to be bent was calculated as 34 mm from Eq (10).

The resistance of the samples was measured and documented using the Arduino micro controller and a very simple circuit. The setup consists of a voltage divider with a known and unknown resistor. The voltage between the resistors is measured with the Arduino. The unknown resistor in our case is the printed track being tested. The Arduino program calculates the resistance of the unknown resistor (the printed trace) from Ohm's Law. The resistance measurements provided by the setup were validated using a Fluke digital multi meter across 20 samples. A maximum error of about 1.5% was observed between the resistance measurements provide by the Arduino and the multi meter. This indicated that bending setup performs well enough for assessing the electrical performance of the printed features.

Static bending: Static bending is a significant aspect of flexible electronics performance. Static bending typically involves bending printed electronic components around cylinders of different radii to evaluate their electrical performance. Electrical performance of the features when subjected to static bending becomes an important factor when the features are intended to be used in applications that involve static bending, such as conformally wrapping a printed circuit over a non-planar object.

We used the variable angle test setup for conducting static bending tests at a maximum bending radius of 10 mm. The test sample was mounted in the bend testing rig with a distance between the arms at 34 mm. The test sample was then bent over a range of -90° to +90°. Electrical resistance of the feature was recorded every 1.8° of rotation (i.e. 1 step) of the stepper motor. A total of 20 electrical resistance measurements were made at each step. The average of the 20 resistance measurements was taken as the electrical resistance of the sample at a particular step. This was done to capture potential voltage fluctuation.

Figure 5.16 (a) shows the normalized resistance change of uniform Al4043 traces subjected to static bending from -90° to +90° with a 10 mm bending radius. Essentially no variation in electrical resistance was noted for static bending across the test samples. The micrograph of a printed trace after static bending is shown in Figure 5.16 (b). The micrograph illustrates that there were no noticeable cracks in the printed features after bending. This indicates that the printed traces behave similar to a ductile wire.

(a)   (b)
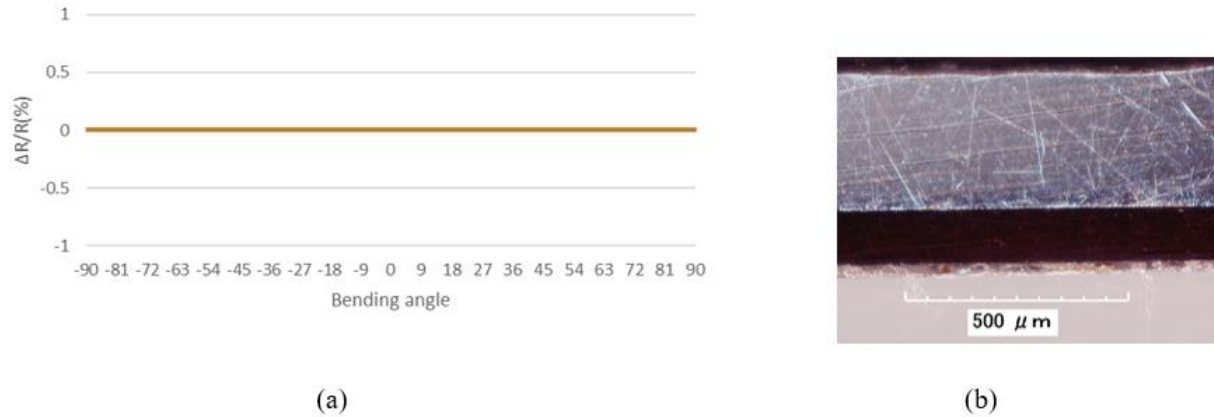
Figure 5.16: (a) Normalized resistance change of Al4043 traces subjected to static bending at 10mm bending radius, (b) Micrograph of a printed trace after static bending.

Figure 5.17 illustrates the normalized resistance change of Ag nanoparticle traces printed on a polymer substrate subjected to static bending from the study published by Huber *et al.*[171]. It can be noted from Figure 5.17 that features printed through metal-based inks show considerable variation in normalized electrical resistance change at higher bending strains. This behavior is typically attributed to the crack onset strain, where cracking occurs in the printed metal feature when the sample is no longer in the elastic regime [173].
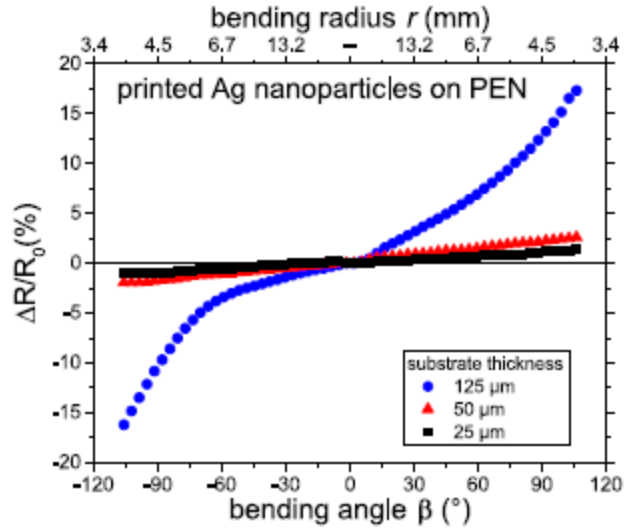
Figure 5.17:Normalized resistance change of Ag nanoparticle traces subjected to static bending (used with permission from [171]).

Comparing the normalized resistance change of MMJ traces with those of metal-based inks, the MMJ traces experience essentially no electrical resistance change at high bending strains. This can be attributed to the ductile nature of what are essentially thick solid core aluminum printed traces in comparison to traces fabricated via sintering of metal nanoparticle inks. The results from this study indicate that MMJ printed traces could be well suited to be employed in application involving static bending.

Compressive vs tensile bending: Prior studies on metal-based inks have shown that printed electronic features can sometimes show different electrical resistance change behavior based on whether they are subjected to tensile or compressive bending strain [171]. In this study, we investigated the behavior of electrical resistance change in MMJ printed traces based on the direction in which the bending strain is applied. Figure 5.18 shows an illustration of the printed traces being subjected to compressive and tensile bending. The "compression" or "tension" is relative to the substrate's location. In case of compression the printed trace is compressed along the substrate. In the case of tension it is stretched over the substrate.
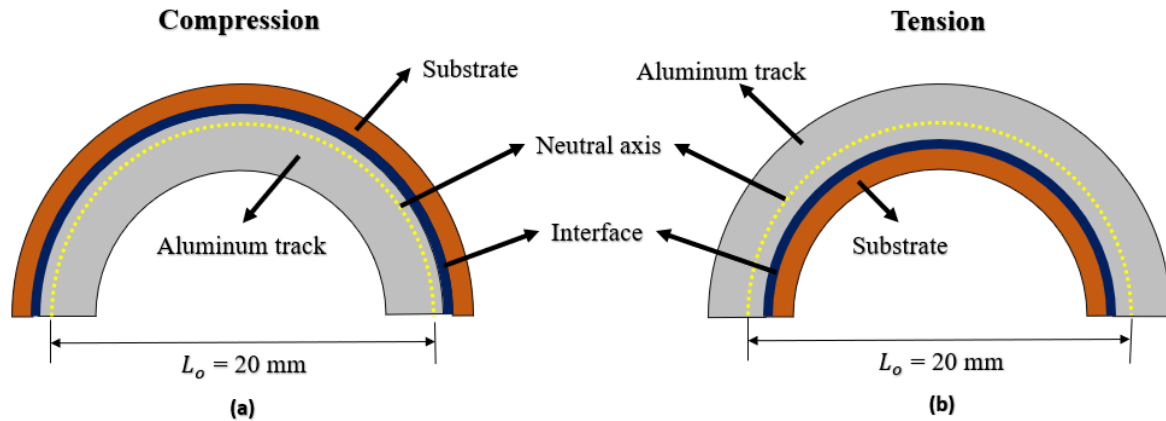
Figure 5.18: Illustration of a printed track in (a)tension (b)compression.

The variable angle test setup allows either compressive or tensile bending to be performed. 20 uniform tracks were bent from 0° to $+90^{\circ}$ for compression and 0° to -90° for tension. The resistance measurements were made in the neutral (flat) position and the flexed position. A crack in the at either the flat or the bent position would be indicated by infinite electrical resistance measurement. Measurements were made in flexed position to avoid the possibility of the cracks in the printed trace to close back up and touch when its flattened and identify the actual cycle when the trace failed.

A total of 20 tracks printed using an overlap fraction of 0.7 and a frequency of 100 Hz were subjected to compressive and tensile bending. The box plot shown in Figure 5.19 showcases the number of bending cycles after which the track completely failed (i.e. the number of cycles after which infinite resistance was measured with the Arduino based ohmmeter, thus indicating loss of electrical continuity in the printed trace). The average and standard deviation of cycles to failure for tensile bending can be noted to approach double that of the average in compression.
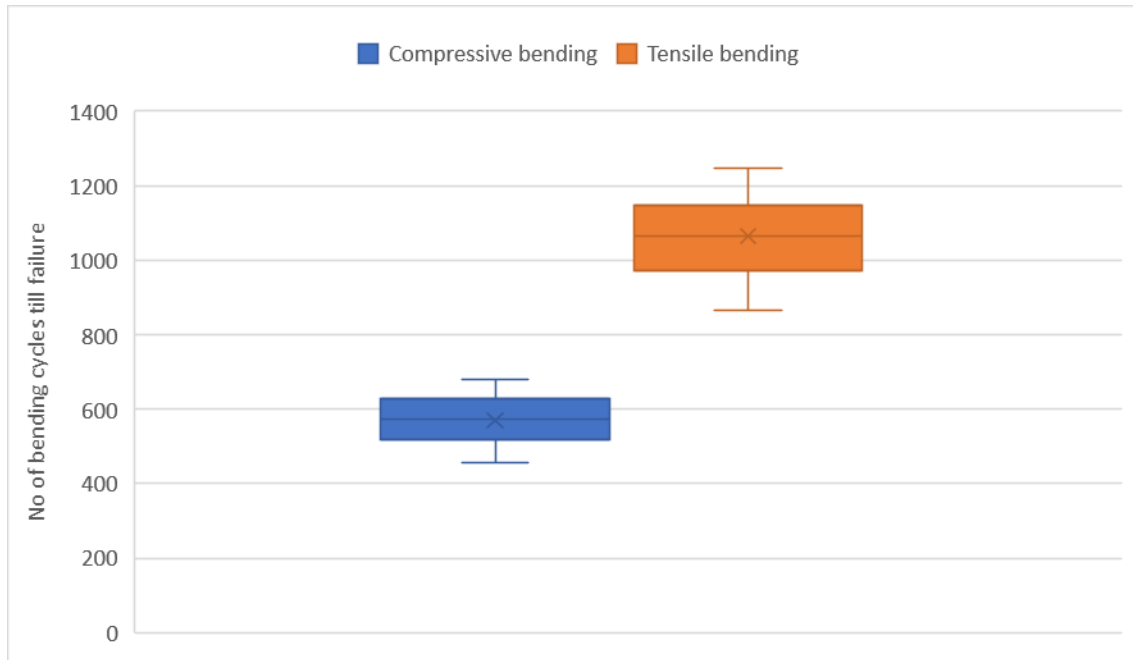
Figure 5.19: Box plot showing the number of cycles after which traces subjected to compression and tensile bending failed.

Figure 5.20 (a) shows a side view micrograph of a uniform trace subjected to compressive bending cycles. The track subjected to compressive bending has peeled off of the substrate. Figure 5.20 (b) shows a side view micrograph of a uniform trace subjected to tensile loading. The micrograph was taken with the substrate slightly bent to clearly show the break in the printed trace. The track subjected to tensile bending can be seen to have a clean break without any significant delamination from the substrate.

(a)

(b)
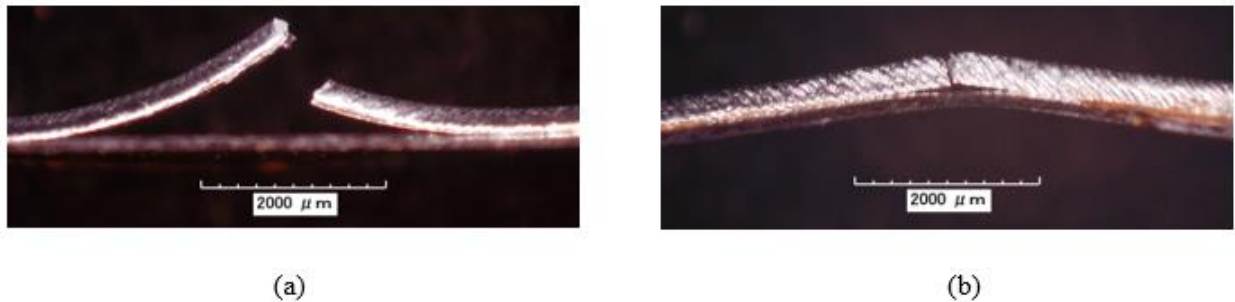
Figure 5.20: Micrographs - taken from the side view - of tracks subjected to (a) compressive bending cycles (b) tensile bending cycles.

Compressive bending most likely leads to earlier failure of the tracks due to the fact that the printed features delaminate from the substrate earlier. This could cause more stress to concentrate in the delaminated trace during the bending process, leading to its failure after fewer bending cycles. When the traces are subjected to tensile bending, the printed trace is in contact with the substrate during most of the bending cycles. This could lead to the stress being distributed through both the track and substrate leading to failure after a greater number of bending cycles. This study illustrates that the features fabricated through molten metal jetting may be more suitable to be employed in cases requiring tensile bending than compressive bending. This could be an important issue to consider when designing electronic devices with preferential bending.

Features with and without pinholes: We also studied the effect of full bending cycles on the electrical performance of traces with and without pinholes. Traces with and without substrate heating (and hence with and without pinholes) were printed at an overlap fraction of 0.7 and frequency of 100 Hz. For features printed with a heated substrate, a temperature of 150 °C was used. For the sake of simplicity, the phrase "with pinholes" is used to mean that those samples were printed without substrate heating and are therefore known to contain significant pinholes per earlier discussion.

20 traces with and without substrate pinholes were subjected to full fatigue bending cycles at a maximum bending radius of 10 mm calculated from Eq (10) based off the combined thickness of the track and the substrate. The plot in Figure 5.21 shows the number of cycles after which the features with and without pinholes completely failed. As expected, the samples with pinholes failed long before the samples without pinholes.
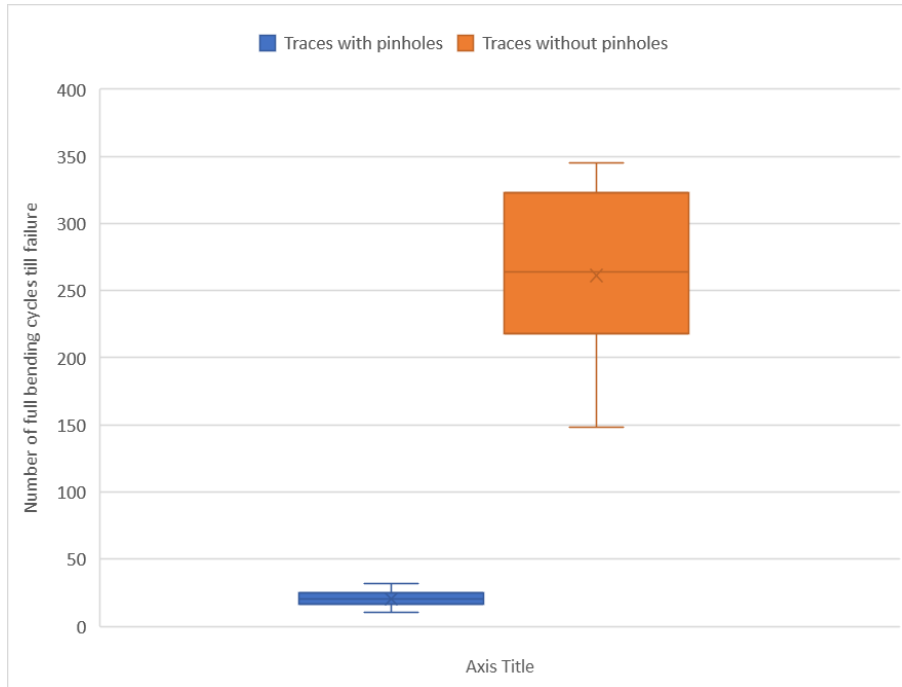
Figure 5.21: Number of full bending cycles after which the features with and without pinholes completely fail.

A trace with pinholes subjected to bending cycles was ground and polished to check for the presence of cracks. Figure 5.22 shows the cross-sectional image of a trace with pinholes subjected to bending fatigue. It can be seen from Figure 5.22 that a macroscopic crack in the trace occurred around the pinhole. This is most likely because the region around the pinhole acts as a stress concentrator as the amount of material around the pinhole is much lower than the amount of material in regions of the trace without pinholes. This shows that the presence of pinholes is indeed detrimental to the performance of the printed traces when they are subjected to fatigue bending.
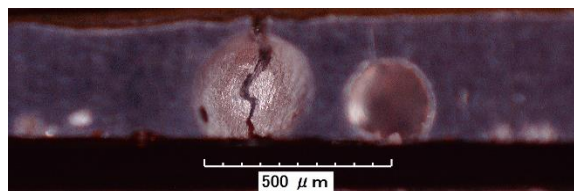
Figure 5.22: Cross-sectional micrograph of a trace with pinholes subjected to bending fatigue.

109

The studies discussed in this section illustrate the fact that the traces printed through molten metal jetting show considerable promise in static bending applications, as there is essentially no increase in electrical resistance. The printed features, however, may not be very suitable to be employed in applications that require bending for over 1000 cycles. The study also shows that compressive bending shows faster degradation of the printed traces than tensile bending. This could be a factor to consider for applications which involve bending in a preferential direction.

5.4 Summary

Three studies conducted for evaluating the performance of the printed features in terms of their electrical and mechanical properties are presented in this chapter. The goal of the characterization studies was to assess whether the features printed using molten metal jetting could be employed as functional electronic circuitry.

Large pinholes which could be detrimental to the performance of printed features have been experimentally observed in the solidified molten aluminum metal droplets deposited on polyimide substrate. In the first study discussed in this chapter, we showed that subjecting the polymer substrate to elevated temperature during droplet deposition considerably reduces the number and size of pinholes. The formation mechanism behind the large pinholes is hypothesized as the release of the adsorbed/absorbed moisture from the polymer substrate into the solidifying droplet due to the rapid rise in temperature of the substrate upon droplet impact. The presence of pinholes was also shown to be detrimental to the electrical performance of the printed traces when they are subjected to fatigue bending.

The electrical conductivity of the printed features was characterized using a four-point probe approach. The electrical resistivity of printed features was found to be close, if not equal, to the bulk metal resistivity of the aluminum alloy used as the raw material. This is highly significant, as resistivity values achieved with

metal nanoparticle inks is typically several times higher than the bulk material resistivity. Electrical currents as high as 10 amps could be passed through the printed traces. This indicates that the features printed using this approach could be ideally suited for high power electronics applications in which large currents must be carried. Examples could include power distribution, solar panel bus bars, and certain antenna applications. The printed traces also showed excellent substrate adhesion when subjected to a standard tape test and static bending.

An inexpensive variable angle bending test setup was completely built in-house to evaluate the performance the printed traces when they are subjected to bending fatigue. A maximum bending radius of 10mm was chosen, as it's a reasonable benchmark for most flexible electronics applications. The printed traces showed no increase in electrical resistance when they are subjected to static bending. This indicated that the features printed through molten metal jetting show considerable potential for being employed in applications that involve static bending. Dynamic bending tests indicated that the printed features may not be very suitable to be employed in applications that require bending for over 1000 cycles, as most of the printed traces completely failed before that. The study also showed that traces subjected to compressive bending showed faster degradation than traces subjected to tensile bending. This could be an important issue for the design of flexible electronic devices with preferential bending.

Chapter 6: Numerical modeling of droplet impingement

The formation mechanism of large pinholes in molten aluminum droplets deposited onto polyimide substrates was discussed in the previous chapter. We hypothesized that the presence of large pinholes in droplets deposited on room temperature Kapton is due to vaporization of absorbed moisture in the substrate. However, this hypothesis relies on two assumptions, (a) the substrate underneath the deposited droplet is heated above the boiling point of water, and (b) the deposited droplet has not completely solidified before the substrate temperature exceeds the boiling point of water. However, quantifying the temperature rise in the substrate as a single 500 µm diameter droplet impinges onto it, and observing the solidification in the interior of the droplet is impossible via physical experimentation. A numerical model that would consider the droplet and substrate properties can provide a reasonably accurate description of the thermodynamics as a metal droplet impacts the substrate.

Hence, the third objective of this research is to develop a numerical model and simulate the process of aluminum droplet impact, flattening, and solidification onto a polyimide substrate to quantify the temperature rise in the substrate during this process. Significant research efforts have been made over the years to develop accurate metal droplet impingement simulation models [174-183]. However the research efforts have been mostly focused on simulating metal droplet impingement onto metal substrates. To the best of our knowledge, there hasn't been research efforts made in studying metal droplet impingement onto polymer substrates. This section discusses the methods employed for simulating aluminum droplet impact onto a polyimide substrate and the results obtained from the model.

6.1 Description of numerical model

We employed ANSYS FLUENT® numerical modeling software to simulate the process of aluminum droplet impact, flattening, and solidification on a polyimide substrate. The simulations were performed by solving fluid flow, energy, and solidification equations on a 2D grid. The schematic of the computational domain used to study droplet impingement is shown in Figure 6.1. The droplet is assumed to be spherical and completely in the liquid form before it impacts vertically on the stationary polyimide substrate. The droplet then flattens, rebounds, and solidifies according to the computational model. The gaseous domain was 3 mm wide (x), 0.6 mm long (y) and the substrate was 125 μm thick. Data from the experimental observations has been used for the initialization of droplet temperature, velocity, and size.
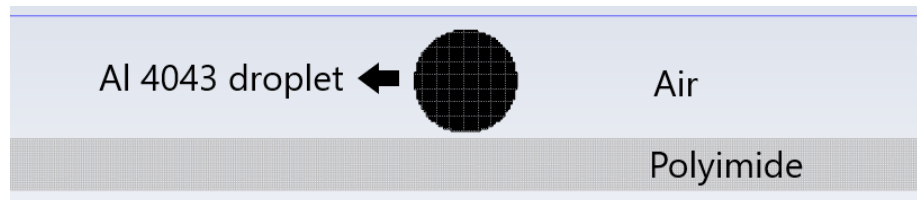
Figure 6.1: Computational domain for the impingement model.

The following assumptions have been made in the numerical model and they dictate the limitations of the model:

1. The flow inside the molten droplet was treated as incompressible and laminar.

2. The material properties of the metal droplet were temperature dependent.

3. The material properties of the polyimide substrate were held constant.

113

4. The heat transfer is dominated by conduction and to a lesser extent, convection modes, ignoring radiation from the droplet surface to the surroundings.

5. Convection to the outside gas is approximated with a constant heat transfer coefficient since the solidification is dominated by conduction to the substrate.

6. Droplet was assumed to be free of oxidation.

7. Material properties were assumed to be isotropic and homogeneous.

8. The shape of the droplet impinging upon the substrate was assumed to be spherical.

9. The droplets have a uniform initial temperature distribution before the impingement.

10. The velocity of the solid phase is zero.

11. Impinge velocity of the droplet is perpendicular to the plane of the substrate and there is no rotation of the droplet along the axis.

12. Walls of the domain are assumed to be at ambient temperature.

Taking the above assumptions into account the equations of mass, momentum, and energy conservation for the binary solid–liquid phase change system of an incompressible droplet is presented as below. Numerical simulations of the droplet deposition processes will be conducted by solving the two-dimensional (x–y) continuity, Navier–Stokes and energy equations. The surface of the impinging droplet will be tracked on a fixed Eulerian structured mesh, using a volume of fluid (VOF) [184] approach coupled with Navier–Stokes and energy equations. The continuity equation or the conservation of mass equation is given by Eq (11) [185].

$$\frac{1}{x}\frac{\partial}{\partial x}(ru) + \frac{\partial v}{\partial y} = 0 \tag{11}$$

where u and v are velocity components in the x and y directions, respectively. The conservation of momentum equation in x and y directions is given by Eq (12).

$$\frac{\partial u}{\partial t} + u\frac{\partial u}{\partial x} + v\frac{\partial u}{\partial y} = -\frac{1}{\rho}\frac{\partial P}{\partial x} + v\left(\frac{\partial^2 u}{\partial y^2} + \frac{1}{x}\frac{\partial}{\partial x}\left(x\frac{\partial u}{\partial x}\right) - \frac{u}{x^2}\right) + g_x + S_x \tag{12}$$

The conservation of energy equation in x and y directions is given by Eq (13).

$$\frac{\partial v}{\partial t} + u\frac{\partial v}{\partial x} + v\frac{\partial v}{\partial y} = -\frac{1}{\rho}\frac{\partial P}{\partial x} + v\left(\frac{\partial^2 v}{\partial y^2} + \frac{1}{x}\frac{\partial}{\partial x}\left(x\frac{\partial v}{\partial x}\right)\right) + g_y + S_y \tag{13}$$

where P, ρ and v are pressure, density, and kinematic viscosity of the fluid, respectively, g is the gravitational force per unit mass and S is any other source term or body force term. The interfacial tension was incorporated in the Navier–Stokes's equation as a body force term. Enthalpy–porosity formulation [186] was incorporated in the solution scheme to handle the effects of solidification. In this technique, a variable named liquid fraction is calculated instead of tracking the melt interface explicitly. The liquid fraction β indicates the volume fraction of the cell in liquid form and is associated with each cell in the domain. The liquid fraction is computed at each iteration based on an enthalpy balance. The mushy zone is modelled as a pseudo porous medium in which the porosity decreases from 1 to 0 as the material solidifies [187]. Solidification results in latent heat generation and a modified form of the energy equation incorporating latent heat, will be used. The modified energy equation is given by Eq (14) [185].

$$\frac{\partial(\rho H)}{\partial t} + \nabla.(\rho u H) = \nabla.(k\nabla T) + S_h \tag{14}$$

where H is the enthalpy per unit volume, k is thermal conductivity and S_h is the rate of energy generation per unit volume. The enthalpy of the material was computed as the sum of the sensible enthalpy h, and the latent heat ΔH from Eq (15) [185].

$$H = h + \Delta H \tag{15}$$

Where sensible enthalpy h is calculated from Eq (16) [185].

$$h = h_{ref} + \int_{T_{ref}}^{T} c_p dT \tag{16}$$

The liquid fraction β, is defined as.

$$\beta = 0 \qquad \text{if} \qquad T < T_{solid} \tag{17}$$

$$\beta = 1 \qquad \text{if} \qquad T > T_{liqud}$$

$$\beta = \frac{T - T_{solid}}{T_{liquid} - T_{solid}} \qquad \text{if} \qquad T_{solid} < T < T_{liqud}$$

The numerical method that is employed in this study is a segregated solution algorithm with a control volume based technique [188]. The pressure and velocity are coupled with semi-implicit method for pressure linked equations (SIMPLE) algorithm which uses a guess-and-correct procedure for the calculation of pressure on the staggered grid arrangement [189]. The quadratic upwind interpolation (QUICK) scheme [190] is employed for the discretization of the model equations. QUICK method can minimize false diffusion errors at the cost of computational stability, as a higher order scheme.

In this model, 4043 Al alloy droplets is initially circular with diameter of 500 μm It falls through gaseous medium at a predefined velocity and impinges on a substrate at a pre-defined temperature. The initial temperature and velocity of the droplet were patched at 700 °C and 2 m/s, respectively. The entire domain is computed with a very fine grid for all the regions where impact, spreading and solidification occur. The mesh is chosen to be uniform square grid of 20 μm side length which equals 1/25th of the droplet diameter. All zones were initialized with a temperature of 30 °C. The surface tension model of continuum surface

force (CSF) proposed by Brackbill *et al.* has been employed [191]. With this model, the addition of surface tension to the VOF calculation results in a source term in the momentum equation. The physical properties of the Al 4043 droplet used in the model are provided in Table 6.1.

Table 6.1: Properties of 4043 Aluminum alloy and polyimide substrate used in the simulation.

Property	Value
Density of Al4043	2350 kg.m^{-3}
Viscosity of Al4043	1.05×10^{-3} N·s/m^2
Surface tension coefficient of Al4043	0.77 N·m^{-1}
Thermal conductivity of Al4043	85.6 W·m^{-1}·K^{-1}
Specific heat capacity of Al4043	1006.43 J·kg^{-1}·K^{-1}
Solidus temperature of Al4043	555 °C
Liquidus temperature of Al4043	615 °C
Latent heat of fusion of Al4043	3.21×10^5 J·kg^{-1}
Static contact angle	100°
Thermal conductivity of polyimide	0.12 W·m^{-1}·K^{-1}
Density of polyimide	1420 kg.m^{-3}
Specific heat of polyimide	1090 J/Kg.K

The polyimide substrate temperature is set as 30 °C. The simulation starts when the droplet is 300 μm from the substrate. The model inputs are provided in Table 6.2.

Table 6.2: Inputs used in the simulation model.

Property	Symbol	Value
Droplet diameter	D	500 μm
Velocity	Y	2.0 m·s^{-1}
Droplet temperature	T_d	700 °C
Substrate temperature	T_{sub}	30 °C
Mushy zone constant	A_m	1.19×10^{11} Kg·m^{-3}·s^{-1}
Solid. Drag coefficient	C	5×10^7 s^{-1}
Critical solid fraction	f_s^*	0.6

6.2 Numerical model results and discussion

Figure 6.2 shows the phase profile of the aluminum droplet solidifying on the substrate at T=0.1 seconds. The droplet spreads on the substrate in the radial direction immediately after impact. The droplet flattens on the substrate for ~400 μs and stops spreading. The simulated drop has a similar morphology to solidified drops observed via physical experimentation as illustrated in Figure 5.6 (b). The solidification starts to occur from the edge of the droplet at about ~13ms. This in line with physical intuition.
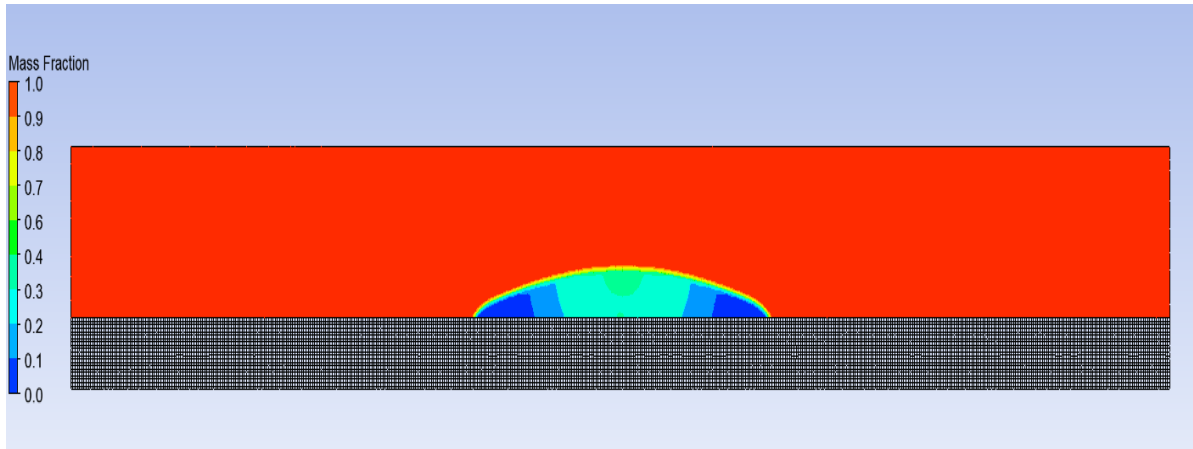
Figure 6.2: Phase profile of the aluminum droplet solidifying at T=0.1s.

Figure 6.3 shows the temperature of the substrate as a function of its thickness under the solidifying droplet 0.1 seconds after the drop impinges on the substrate. It can be noted that almost the entire substrate thickness underneath the droplet experiences an increase in temperature to well over 100 °C. Figure 6.2 illustrates that a significant portion of the droplet is still in liquid phase at T=0.1 seconds after the simulation starts.
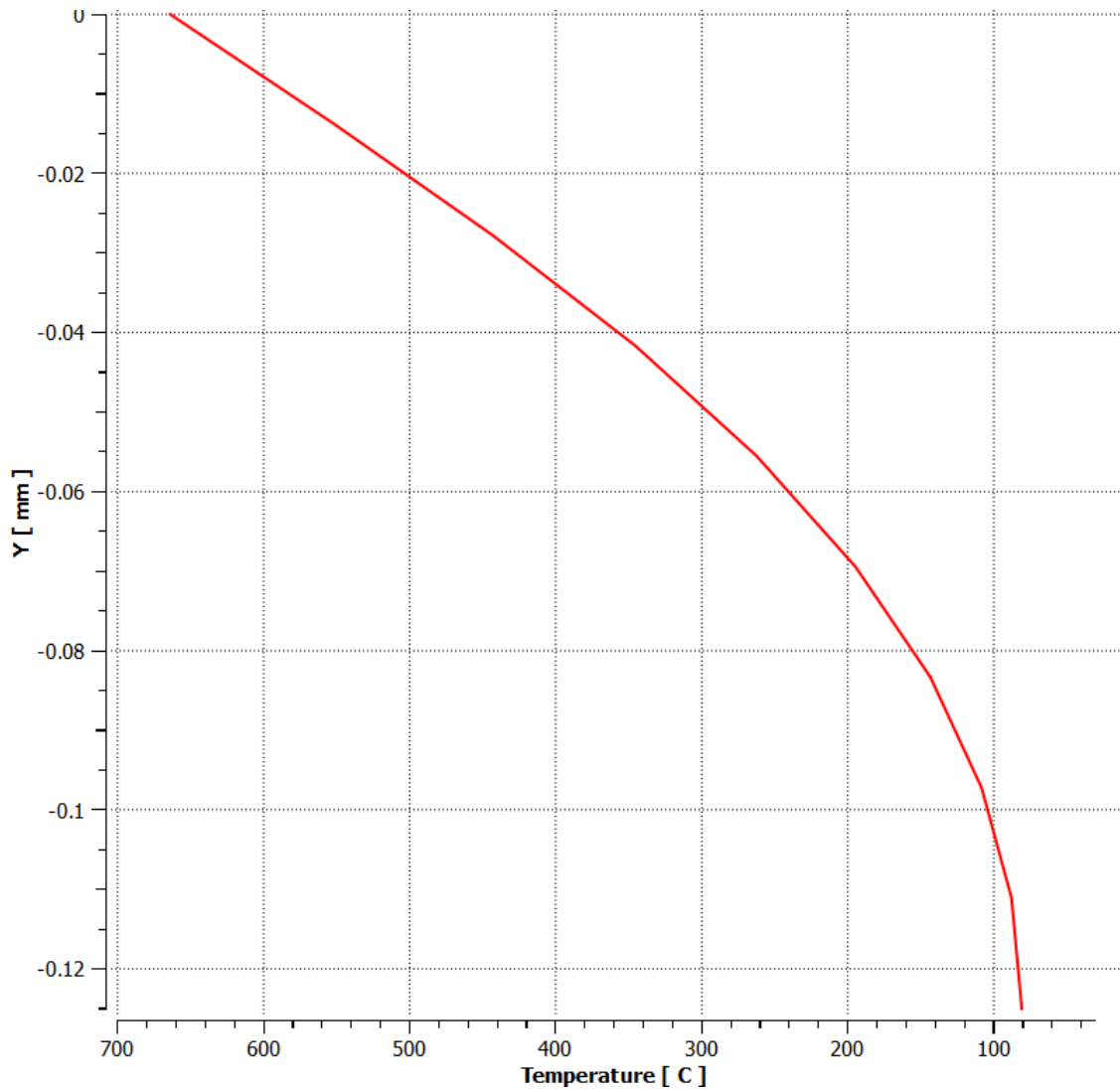
Figure 6.3: Plot showing the temperature of the substrate which is at room temperature as a function of its thickness, 0.1 seconds after the drop impinges on the substrate.

So a significant portion of the polyimide substrate under neath the droplet experiences a temperature of over 100 °C (i.e. the boiling point of water) while a significant portion of the droplet is still in liquid phase. This indicates the feasibility of adsorbed moisture in the substrate vaporizing and escaping into the droplet which is still in the liquid phase.

6.3 Summary

The formation mechanism behind the formation of large pinholes in aluminum droplets deposited onto room temperature polyimide substrates, as discussed in Section 5.1, is hypothesized to be the release of adsorbed moisture from the polymer substrate into the solidifying droplets. However, this hypothesis relies on the assumption that the substrate underneath the solidifying droplet experiences a temperature rise beyond the boiling point of water. Experimentally verifying the temperature rise in the substrate as a single 500μm diameter droplet impinges onto it can be extremely difficult. Hence a numerical model that would consider the droplet and substrate properties was developed to obtain a better understanding of thermodynamics as a metal droplet impacts the substrate. This chapter provided a discussion of the numerical model details and the results obtained from the numerical model.

ANSYS FLUENT® was employed to simulate the process of aluminum droplet impact, flattening, and solidification on a polyimide substrate. The fluid flow, energy, and solidification equations were solved using a 2D grid. The simulation of the droplet deposition process was conducted by solving the 2D (x–y) continuity, Navier–Stokes and energy equations. The surface of the impinging droplet was tracked on a fixed Eulerian structured mesh, using a volume of fluid (VOF) approach coupled with Navier–Stokes and energy equations.

The results from the numerical model revealed that almost the entire polyimide substrate thickness underneath the deposited metal droplet experiences an increase in temperature to well over 100°C when the droplet is still in a liquid phase. As a significant portion of the polyimide substrate underneath the droplet experiences a temperature exceeding the boiling point of water, it is likely that the adsorbed moisture in the substrate vaporizes. Within the time scale of the substrate's temperature rise, a significant portion of the deposited droplet is in the liquid phase. The vaporized moisture could escape into the molten droplet leading to the large sized pinholes. This supports the hypothesis that the large pinholes are likely to have formed in metal droplets deposited onto room temperature substrate due to the release of adsorbed moisture from the polymer substrate into the solidifying droplets.

Chapter 7: Conclusions and recommendations

7.1 Summary

The aim of this research was to explore a novel droplet-based metal additive manufacturing process referred as molten metal jetting for fabricating highly conductive printed electronic circuits. Several key challenges with the existing direct writing approaches have been addressed. We chose to explore the potential of molten metal jetting in fabricating functional electronic components by pursuing three major objectives. The first objective was to determine ideal process parameters for printing uniform metal features on polymer substrates. This is intended to provide the process conditions that would be suitable for fabricating high quality metal traces on polymer substrates. The second objective was to evaluate the performance of printed features in terms of their electrical and mechanical properties to assess the viability of using the features as functional electronic circuitry. The third objective was to develop a numerical model of metal droplet impingement process onto polymer substrate to provide insights into the thermodynamic behavior of the polymer substrate with metal droplet impingement.

Experimental and numerical modeling details corresponding to each of these three objectives have been presented. Through this research, we showed that molten metal jetting is a novel and cost-effective approach for fabricating highly conductive electronic circuit patterns. Figure 7.1 shows some directly printed electronic circuits on a polyimide substrate.
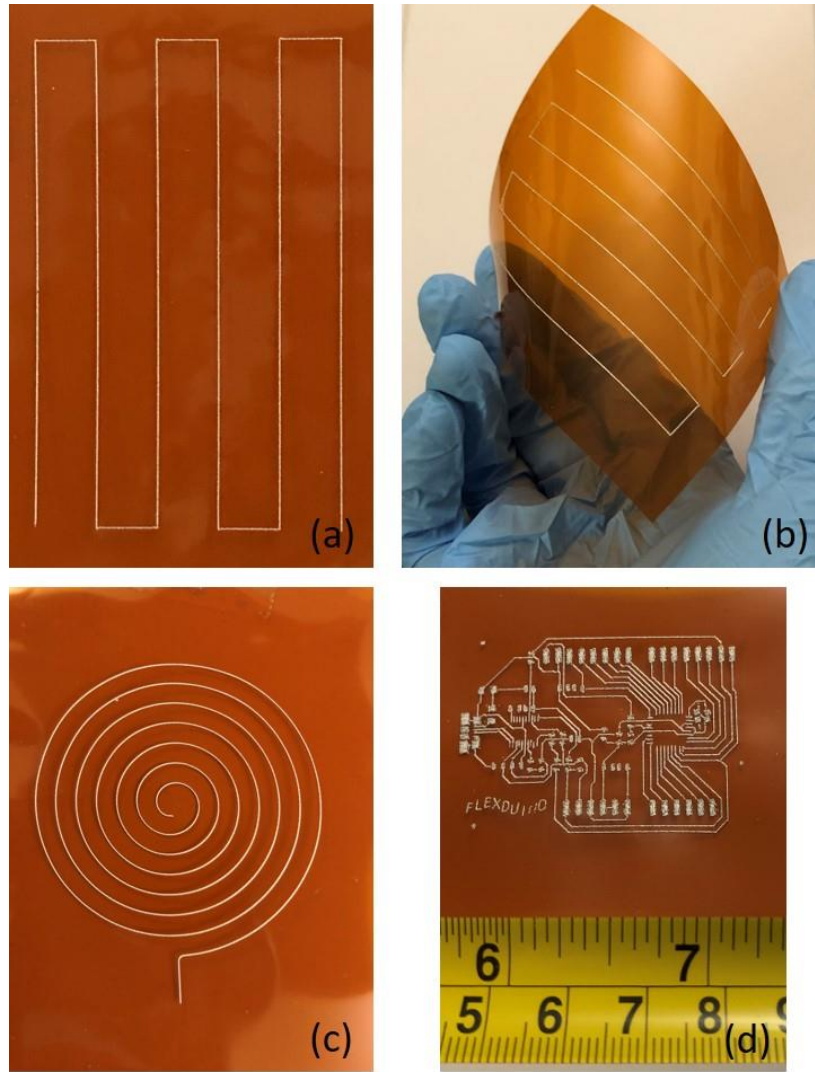
Figure 7.1: Electronic circuits printed using molten metal jetting process (a) serpentine circuit containing regular bends (b) serpentine structure being subjected to bending (c) inductor (4) microcontroller circuit.

The electrical conductivity of the printed features was found to be close, if not equal, to the bulk metal resistivity of the aluminum alloy used as the raw material. This is very significant, as electrical resistivity values typically achieved using metal-based nanoparticle inks is several times higher than the bulk conductivity of the metal used as the raw material. The raw material used in molten metal jetting is in the form of a wire, so it is several orders of magnitude cheaper than the equivalent weight of metal nanoparticles. This makes the process significantly more economical than the conventional approach

employed for printing electronics using solvent-based metal inks. The molten metal jetting approach also doesn't require any post processing steps after printing such as drying, curing, or sintering in order to make the fabricated circuitry electrically conductive. This is extremely desirable because it reduces the installation cost, fabrication time and thereby the final product cost.

7.2 Key contributions

Through experimental studies, we identified the process conditions that would help achieve high quality printed features using a molten metal jetting approach. We demonstrated the feasibility of fabricating features with Rq surface roughness values in the range of 5µm using this approach. This indicated that with further efforts, it is feasible to fabricate functional circuitry with surface roughness close to the surface roughness of electrically conductive features currently used in PCB's. Through experimental investigation, we suggested and validated a simple formulation that considers the volume of individual deposited droplets and drop spacing between adjacent droplets to predict the equivalent wire gauge of the uniform printed traces. This could be useful for knowing the current carrying capabilities of the printed features in high power electronics applications.

We observed large pinholes inside droplets deposited onto room temperature polyimide substrates. We hypothesized that the formation mechanism behind the pinholes was due to the release of adsorbed moisture from the polyimide into the solidifying droplet. We validated this hypothesis through experimental investigation and numerical modelling. We found that heating of the substrate above the boiling point of water dramatically reduces the number and size of pinholes due to the removal of adsorbed moisture through the heating process.

Through characterization studies, we identified that the electrical conductivity of the printed features was close, if not equal, to the bulk metal resistivity of the aluminum alloy used as the raw material. We found

that current as high as 10 amps could be successfully passed through printed traces. We showed that the features fabricated with the MJP process demonstrate excellent substrate adhesion. We developed a variable angle bending test apparatus to study the electrical performance of the printed features when they are subjected to static and fatigue bending. We found no change in electrical resistance when printed features were subjected to static bending. This indicated that the features fabricated through molten metal jetting process could be well suited to be employed in applications involving static bending up to a bending radius as low as 10 mm. However most of the printed traces were noted to fail after about 1000 full bending cycles at a bending radius of 10mm, indicating that the features printed through molten metal jetting may not be ideal in applications involving bending over thousands of cycles. We also found that that the printed features tend to fail earlier when they are subjected to compressive fatigue bending than tensile fatigue bending. This could be an important issue to consider for the designing electronic devices with preferential bending.

7.3 Recommendations for future research

The work presented in this dissertation showcased the potential of molten metal jetting for fabricating functional electronic circuits. There are several directions in which this work could be extended to fully realize the potential of molten metal jetting for printed electronics applications. Some of the potential directions in which this research could be extended in the future are presented in this section.

Fabricating features with sub 100μm feature resolution

There is very high demand from the electronics industry to fabricate features with finer resolutions than those achieved during the course of this research using 250 µm diameter nozzle openings. The lateral resolution that can be currently achieved through established direct writing processes is between 5-100 µm [5]. The research presented in this dissertation showed the feasibility of printing highly conductive traces

with print resolution of ~ 250 μm. Achieving sub 100 μm feature resolution with molten metal jetting processes would make the approach favorable in terms of both electrical performance and achievable feature size compared with established direct write processes. Simonelli *et al.* have reported the feasibility of jetting silver droplet diameters as small as ~80 µm using a molten metal droplet jetting approach [132]. Future research could be directed towards experimental studies investigating the feasibility of fabricating sub 100 μm features onto polymer substrates through molten metal jetting. It is noted that jetting of molten metals has both similarities and differences with jetting of aqueous or solvent based inks. A primary difference is that the surface tensions of jetted aqueous or solvent inks are typically on the order of 30 dynes/cm, whereas the surface tensions of molten metals is often above 1,000 dynes/cm. A consequence of ultra-high surface tension is that it may take considerably more energy to successfully eject droplets of molten metal from very small nozzle openings than it would with aqueous or solvent based inks. Careful selection of high wetting nozzle materials capable of withstanding the temperature of molten metals as well as potential corrosive attack of molten metals is needed, and study of the achievable ejection forces produced via Lorenz forces in this process must be studied to determine the practical lower limit of droplet size for a given hardware setup.

Fabricating electronic circuits with copper

The research presented in this dissertation has been focused extensively on aluminum alloy 4043. Through the research presented in this dissertation, the feasibility of depositing high temperature melting point metal, such as aluminum, onto polymer substrates for fabricating electronic circuits has been demonstrated. However metals such as silver, copper, and gold are more electrically conductive than aluminum. Among these metals copper is the most widely used metal for fabricating electrical circuits due to its high electrical conductivity, high thermal resistance, low cost and solderability.

Copper has a melting point of ~1085 °C. The high melting point and thereby the high temperature droplets could pose a significant challenge in successfully depositing the metal droplets onto polymer substrates without causing damage to the substrates. Research on pneumatic molten metal jetting indicates the feasibility of jetting copper droplets [192]. Future research in developing printing systems capable of jetting copper droplets in a consistent fashion would enable conducting experimental investigation into the feasibility of fabricating copper circuits onto polymer substrates. Experimentally investigating the feasibility of fabricating copper circuits onto polymer substrates would be highly desirable. Successfully fabricating copper circuits on polymer substrates would be significant as that could enable the fabricated features to be employed in numerous applications. In order to jet copper, careful attention will have to be devoted to selection of wetted materials in the jetting fixture through which electromagnetic energy will pass. For example, some ceramic materials undergo phase changes above ~1200 °C that make them prone to cracking. Cracking of wetted components in this process will lead to catastrophic failure due to leaking of molten metal. Most ceramic materials also require a protective (oxygen free) environment when used at high temperatures. All of these factors must be considered when designing a jetting fixture intended to operate at a jetting temperature of ~1300 °C needed for molten copper.

Fabricating electronic circuits on inexpensive substrates such as PET

The research presented in this dissertation discussed the deposition of high temperature molten metal droplets onto polymer substrates. The substrate used for all the studies mentioned in this research was polyimide. Polyimide was chosen because it has a high glass transition temperature of about 360°C. However the cost of polyimide is ~ $400 per pound [193]. Preliminary experiments conducted by depositing aluminum droplets with diameters of ~ 150 μm onto s PET (polyethylene terephthalate) substrate indicated that it is possible to deposit aluminum droplets onto PET without completely damaging the substrate. Figure 7.2 shows aluminum 4043 traces printed onto a 125 μm thick PET substrate. Although some damage to the

PET substrate can be noted to have occurred around the deposited droplets, the substrates were not completely damaged.
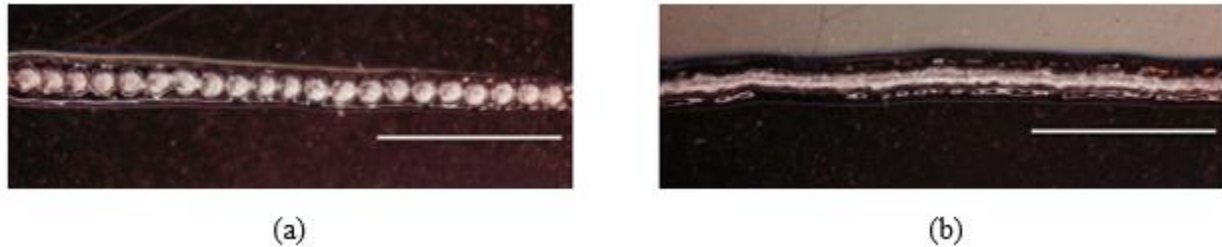
Figure 7.2: 150um diameter aluminum 4043 droplets deposited onto 125um thick PET at overlap fraction of (a) 0 (b)0.5. Scale bar = 1000μm.

Experimental investigation into the possibility of depositing high temperature metal droplets onto inexpensive polymer substrates such as PET would be highly desirable. As PET costs ~ $5 per pound, it is significantly less expensive than polyimide [194]. Studies involving process conditions such as droplet size, droplet temperature, droplet deposition frequency, and substrate temperature could lead to successful use of low-cost temperature sensitive substrates, such as PET, for jetted molten metal electronics. Research in this direction would be highly beneficial as it would enable fabricating functional electronic circuits at a fraction of the cost. The ANSYS models presented earlier in this dissertation will be very useful for this future research thrust. As droplet diameter decreases, the volume of the droplet decreases as a function of the cubed root of the drop diameter. Put another way, the thermal energy per drop decreases rapid as the drop diameter decreases. By carefully studying the heat flux into a substrate as a function of drop size, drop spacing, and jetting frequency, it is possible to identify the approximate conditions under which molten metal traces may be successfully jetted onto thermally sensitive, but low cost, substrates.

Effects of twisting fatigue on electrical performance of printed features

The electrical performance of the printed features when they are subjected to static and dynamic bending are presented in this dissertation. However there are also applications that involve twisting of the printed features. Exploring the electrical performance of the printed features when they are subjected to twisting fatigue could be an interesting avenue for future research. Just as the research presented in Section 5.3 indicated that the traces subjected to compressive bending showed faster degradation than traces subjected to tensile bending, studying the performance of printed features subjected to twisting fatigue could provide novel insights. The insights could be helpful in assessing the feasibility of employing features fabricated with molten metal jetting for application involving twisting of printed features.

Impact of process conditions on quality of printed patches

The research presented in this dissertation showcased the possibility of fabricating electrically conductive traces onto polymer substrates using molten metal jetting processes. However, electrically conductive traces are only one aspect of functional electronic circuitry. Electrically conductive patches are a major element of any functional electronic circuitry. Preliminary research has shown the possibility of fabricating electrically conductive patches on polyimide substrate without causing extensive thermal damage to the substrate. The profilometry images shown in Figure 7.3 show the surface profile of Al 4043 patches printed on polyimide substrate at two different track overlap fractions.
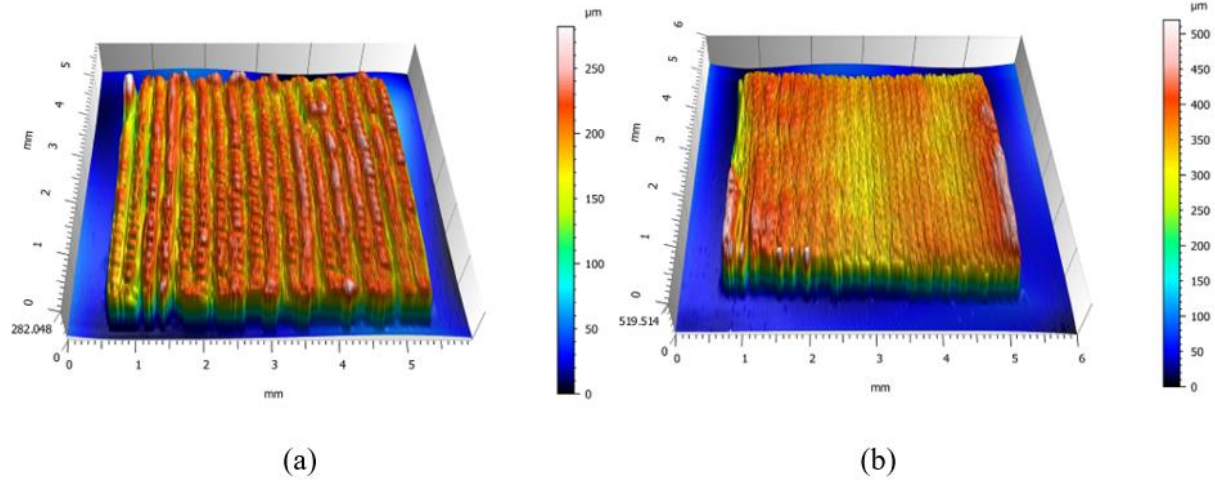
Figure 7.3: Surface profile scans for patches printed at track overlap fraction of (a) 0 and (b) 0.25.

Future research could be focused on experimentally understanding the effect of process conditions such as droplet temperature, deposition frequency, and lateral track overlap fraction on the quality of printed patches. The research could enable fabrication of patches with desired surface roughness and patch thickness.

Numerical modelling of pinhole formation

The numerical model presented in this dissertation helped in understanding the temperature rise in the substrate as a molten metal droplet impinges onto it. The numerical model helped in providing more evidence to the hypothesis that pinholes are formed in the printed droplets due to the escaping vapor into the solidifying droplets. However the model presented in this research is a 2D model which does not simulate the adsorbed moisture release into the solidifying droplet. Future research focused on developing a 3D numerical model that considers the moisture absorption of polymer substrates could provide further evidence in validating the hypothesis. They could provide insights into pinhole formation. Further development of numerical models to study the impact process conditions such as drop spacing and frequency on the thermodynamic behavior of substrates could be of great use as that could help in predicting the suitable process conditions to be employed for different metal and substrate combinations.

References

[1]   A. Fuentes, *The creative spark: How imagination made humans exceptional*. Penguin, 2017.

[2]   K. Schwab, *The fourth industrial revolution*. Crown Business, 2017.

[3]   F. O. Sequeda, "Integrated Circuit Fabrication—A Process Overview," *JOM,* vol. 37, no. 5, pp. 43-50, 1985.

[4]   E. Cantatore, "Applications of organic and printed electronics," *A Technology-Enabled Revolution. New York: Springer Science+ Business Media,* p. 180, 2013.

[5]   J. S. Chang, A. F. Facchetti, and R. Reuss, "A Circuits and Systems Perspective of Organic/Printed Electronics: Review, Challenges, and Contemporary and Emerging Design Approaches," *IEEE Journal on Emerging and Selected Topics in Circuits and Systems,* vol. 7, no. 1, pp. 7-26, 2017, doi: 10.1109/JETCAS.2017.2673863.

[6]   G. Tong, Z. Jia, and J. Chang, "Flexible hybrid electronics: Review and challenges," 2018: IEEE, pp. 1-5.

[7]   Q. Huang and Y. Zhu, "Printing conductive nanomaterials for flexible and stretchable electronics: A review of materials, processes, and applications," *Advanced Materials Technologies,* vol. 4, no. 5, p. 1800546, 2019.

[8]   S. M. F. Cruz, L. A. Rocha, and J. C. Viana, "Printing technologies on flexible substrates for printed electronics," in *Flexible electronics*: IntechOpen, 2018.

[9]   L. Febvre and H.-J. Martin, *The coming of the book: the impact of printing 1450-1800*. Verso, 1976.

[10]   J. Perelaer, A. W. M. De Laat, C. E. Hendriks, and U. S. Schubert, "Inkjet-printed silver tracks: low temperature curing and thermal stability investigation," *Journal of Materials Chemistry,* vol. 18, no. 27, pp. 3209-3215, 2008.

[11]   H. Sirringhaus *et al.*, "High-resolution inkjet printing of all-polymer transistor circuits," *Science,* vol. 290, no. 5499, pp. 2123-2126, 2000.

[12]   X. Wang and J. Liu, "Recent Advancements in Liquid Metal Flexible Printed Electronics: Properties, Technologies, and Applications," *Micromachines,* vol. 7, no. 12, p. 206, 2016.

[13]   V. Zardetto, T. M. Brown, A. Reale, and A. Di Carlo, "Substrates for flexible electronics: A practical investigation on the electrical, film flexibility, optical, temperature, and solvent resistance properties," *Journal of Polymer Science Part B: Polymer Physics,* vol. 49, no. 9, pp. 638-648, 2011.

[14]   A. Hodgson, "The role of paper in the future of printed electronics," *CoPADD 2007,* p. 39, 2007.

[15]   Z. Wang, W. Wang, Z. Jiang, and D. Yu, "Low temperature sintering nano-silver conductive ink printed on cotton fabric as printed electronics," *Progress in Organic Coatings,* vol. 101, pp. 604-611, 2016.

[16]   K. Suganuma, *Introduction to Printed Electronics* (SpringerBriefs in Electrical and Computer Engineering). Springer New York, 2014.

[17]   H. Shirakawa, E. J. Louis, A. G. MacDiarmid, C. K. Chiang, and A. J. Heeger, "Synthesis of electrically conducting organic polymers: halogen derivatives of polyacetylene,(CH) x," *Journal of the Chemical Society, Chemical Communications,* no. 16, pp. 578-580, 1977.

[18]   M. Hilder, B. Winther-Jensen, and N. B. Clark, "based, printed zinc–air battery," *Journal of power Sources,* vol. 194, no. 2, pp. 1135-1141, 2009.

[19]   P. Kopola *et al.*, "Gravure printed flexible organic photovoltaic modules," *Solar Energy Materials and Solar Cells,* vol. 95, no. 5, pp. 1344-1347, 2011.

[20]   T. Sekitani *et al.*, "Stretchable active-matrix organic light-emitting diode display using printable elastic conductors," *Nature materials,* vol. 8, no. 6, p. 494, 2009.

[21]   S. Gamerith, A. Klug, H. Scheiber, U. Scherf, E. Moderegger, and E. J. W. List, "Direct Ink-Jet Printing of Ag–Cu Nanoparticle and Ag-Precursor Based Electrodes for OFET Applications," *Advanced Functional Materials,* vol. 17, no. 16, pp. 3111-3118, 2007.

[22]   R. A. Street *et al.*, "Jet printing flexible displays," *Materials Today,* vol. 9, no. 4, pp. 32-37, 2006.

[23]   V. Subramanian *et al.*, "Progress toward development of all-printed RFID tags: materials, processes, and devices," *Proceedings of the IEEE,* vol. 93, no. 7, pp. 1330-1338, 2005.

[24]   "Printed hydrogen sulfide gas sensor on paper substrate based on polyaniline composite," vol. 534, pp. 621–628, 1 May 2013.

[25]   M. Inoue *et al.*, "A super-flexible sensor system for humanoid robots and related applications," *Journal of The Japan Institute of Electronics Packaging,* vol. 11, no. 2, pp. 136-140, 2008.

[26]   R. Das, X. He, and K. Ghaffarzadeh, "Flexible, printed and organic electronics 2019–2029: forecasts, players & opportunities," *IDTechEx Research,* 2018.

[27]   D. Lupo *et al.*, "OE-A Roadmap for Organic and Printed Electronics," (in en), pp. 1-26, 2014, doi: 10.1007/978-1-4614-3160-2_1.

[28]   H. Jeong *et al.*, "Modular and Reconfigurable Wireless E-Tattoos for Personalized Sensing," *Advanced Materials Technologies,* vol. 4, no. 8, p. 1900117, 2019.

[29]   Y. Khan, A. Thielens, S. Muin, J. Ting, C. Baumbauer, and A. C. Arias, "A new frontier of printed electronics: flexible hybrid electronics," *Advanced Materials,* vol. 32, no. 15, p. 1905279, 2020.

[30]   D. Espalin, D. W. Muse, E. MacDonald, and R. B. Wicker, "3D Printing multifunctionality: structures with electronics," *The International Journal of Advanced Manufacturing Technology,* vol. 72, no. 5, pp. 963-978, 2014/05/01 2014, doi: 10.1007/s00170-014-5717-7.

[31]   F. N. Cane, "Electroless plating process for the manufacture of printed circuit boards," ed: Google Patents, 1997.

[32]   M. L. Green and R. A. Levy, "Chemical vapor deposition of metals for integrated circuit applications," *JOM,* vol. 37, no. 6, pp. 63-71, 1985.

[33]   K. D. Harris, A. L. Elias, and H. J. Chung, "Flexible electronics under strain: a review of mechanical characterization and durability enhancement strategies," *Journal of materials science,* vol. 51, no. 6, pp. 2771-2805, 2016.

[34]   A. a. M. S. Kamyshny, "Conductive Nanomaterials for Printed Electronics," *Small,* vol. 10, no. 17, pp. 3515--3535, 2014, doi: 10.1002/smll.201303000.

[35]   D. Deganello, J. A. Cherry, D. T. Gethin, and T. C. Claypole, "Patterning of micro-scale conductive networks using reel-to-reel flexographic printing," *Thin Solid Films,* vol. 518, no. 21, pp. 6113-6116, 2010.

[36]   M. Pudas, N. Halonen, P. Granat, and J. Vähäkangas, "Gravure printing of conductive particulate polymer inks on flexible substrates," *Progress in Organic Coatings,* vol. 54, no. 4, pp. 310-316, 2005.

[37]   W. J. Hyun, E. B. Secor, M. C. Hersam, C. D. Frisbie, and L. F. Francis, "High-resolution patterning of graphene by screen printing with a silicon stencil for highly flexible printed electronics," *Advanced Materials,* vol. 27, no. 1, pp. 109-115, 2015.

[38]   A. De la Fuente Vornbrock, "Roll printed electronics: Development and scaling of gravure printing techniques," 2009.

[39]   E. Kunnari, J. Valkama, M. Keskinen, and P. Mansikkamäki, "Environmental evaluation of new technology: printed electronics case study," *Journal of Cleaner Production,* vol. 17, no. 9, pp. 791-799, 6// 2009, doi: http://dx.doi.org/10.1016/j.jclepro.2008.11.020.

[40]   M. P. Tsang, G. W. Sonnemann, and D. M. Bassani, "Life-cycle assessment of cradle-to-grave opportunities and environmental impacts of organic photovoltaic solar panels compared to conventional technologies," *Solar Energy Materials and Solar Cells,* vol. 156, pp. 37-48, 2016.

[41]   G. Cummins and M. P. Y. Desmulliez, "Inkjet printing of conductive materials: A review," *Circuit World,* vol. 38, no. 4, pp. 193-213, 2012/11/16 2012, doi: 10.1108/03056121211280413.

[42]   B. King and M. Renn, "Aerosol Jet direct write printing for mil-aero electronic applications," 2009.

[43]   X. Chen, K. Church, and H. Yang, "High speed non-contact printing for solar cell front side metallization," in *2010 35th IEEE Photovoltaic Specialists Conference*, 20-25 June 2010 2010, pp. 001343-001347, doi: 10.1109/PVSC.2010.5614364.

[44]   W. A. MacDonald *et al.*, "Latest advances in substrates for flexible electronics," *Journal of the Society for Information Display,* vol. 15, no. 12, pp. 1075-1083, 2007.

[45]   P. J. Smith, D. Y. Shin, J. E. Stringer, B. Derby, and N. Reis, "Direct ink-jet printing and low temperature conversion of conductive silver patterns," *Journal of Materials Science,* vol. 41, no. 13, pp. 4153-4158, 2006// 2006, doi: 10.1007/s10853-006-6653-1.

[46]   T. H. J. Van Osch, J. Perelaer, A. W. M. de Laat, and U. S. Schubert, "Inkjet printing of narrow conductive tracks on untreated polymeric substrates," *Advanced Materials,* vol. 20, no. 2, pp. 343-345, 2008.

[47]   E. Tekin, P. J. Smith, and U. S. Schubert, "Inkjet printing as a deposition and patterning tool for polymers and inorganic particles," *Soft Matter,* 10.1039/B711984D vol. 4, no. 4, pp. 703-713, 2008, doi: 10.1039/B711984D.

[48]   J. Perelaer *et al.*, "Printed electronics: the challenges involved in printing devices, interconnects, and contacts based on inorganic materials," *Journal of Materials Chemistry,* 10.1039/C0JM00264J vol. 20, no. 39, pp. 8446-8453, 2010, doi: 10.1039/C0JM00264J.

[49]   J. a. K. M. a. H. C. E. a. S. U. S. Perelaer, "Microwave Flash Sintering of Inkjet-Printed Silver Tracks on Polymer Substrates," *Advanced Materials,* vol. 21, no. 47, pp. 4830--4834, 2009, doi: 10.1002/adma.200901081.

[50]   R. Abbel *et al.*, "Photonic flash sintering of silver nanoparticle inks: a fast and convenient method for the preparation of highly conductive structures on foil," *MRS Communications,* vol. 2, no. 4, pp. 145-150, 2012.

[51]   I. Reinhold *et al.*, "Argon plasma sintering of inkjet printed silver tracks on polymer substrates," *Journal of Materials Chemistry,* vol. 19, no. 21, pp. 3384-3388, 2009.

[52]   M. Layani, I. Cooperstein, and S. Magdassi, "UV crosslinkable emulsions with silver nanoparticles for inkjet printing of conductive 3D structures," *Journal of Materials Chemistry C,* vol. 1, no. 19, pp. 3244-3249, 2013.

[53]   H. W. Tan, J. An, C. K. Chua, and T. Tran, "Metallic nanoparticle inks for 3D printing of electronics," *Advanced Electronic Materials,* vol. 5, no. 5, p. 1800831, 2019.

[54]   K. Rajan, I. Roppolo, A. Chiappone, S. Bocchini, D. Perrone, and A. Chiolerio, "Silver nanoparticle ink technology: state of the art," *Nanotechnology, science and applications,* vol. 9, p. 1, 2016.

[55]   E. V. Agina *et al.*, "Polymer surface engineering for efficient printing of highly conductive metal nanoparticle inks," *ACS applied materials & interfaces,* vol. 7, no. 22, pp. 11755-11764, 2015.

[56]   C. Guo, Y. Yu, and J. Liu, "Rapidly patterning conductive components on skin substrates as physiological testing devices via liquid metal spraying and pre-designed mask," *Journal of Materials Chemistry B,* vol. 2, no. 35, pp. 5739-5745, 2014.

[57]   "Cost of copper nanoparticles." https://www.ssnano.com/inc/sdetail/copper_nanoparticles_nanopowder__cu__99_9__100_130nm_/21194 (accessed 2021).

[58]   "Cost of 4043 aluminum wire." https://www.airgas.com/product/Welding-Products/Filler-Metal/MIG-Wire-%28GMAW-%26-SAW%29/MIG-Wire---Aluminum/p/RAD64001502 (accessed 04/23/2021, 2021).

[59]   "Cost of Aluminum nanoparticles."

https://www.ssnano.com/inc/sdetail/aluminum_nanoparticles__nanopowder__al__99_7__40_

60_nm_/276 (accessed 2021).

[60]   K. K. B. Hon, L. Li, and I. M. Hutchings, "Direct writing technology—Advances and

developments," *CIRP Annals,* vol. 57, no. 2, pp. 601-620, 2008.

[61]   V. Sukhotskiy *et al.*, "Magnetohydrodynamic Drop-on-Demand Liquid Metal 3D Printing."

[62]   Z. Fan *et al.*, "Toward the development of printable nanowire electronics and sensors,"

Advanced Materials, vol. 21, no. 37, pp. 3730-3743, 2009.

[63]   G. Gruner, "Carbon nanotube films for transparent and plastic electronics," *Journal of Materials*

Chemistry, vol. 16, no. 35, pp. 3533-3539, 2006.

[64]   L. W. McKeen, *Film properties of plastics and elastomers*. William Andrew, 2017.

[65]   D. Li, W. Y. Lai, Y. Z. Zhang, and W. Huang, "Printable transparent conductive films for flexible

electronics," *Advanced Materials,* vol. 30, no. 10, p. 1704738, 2018.

[66]   Y. Meng, T. Ma, F. J. Pavinatto, and J. D. MacKenzie, "Interface modified flexible printed

conductive films via Ag2O nanoparticle decorated Ag flake inks," *ACS applied materials &*

interfaces, vol. 11, no. 9, pp. 9190-9196, 2019.

[67]   R. Faddoul, N. Reverdy-Bruas, and A. Blayo, "Formulation and screen printing of water based

conductive flake silver pastes onto green ceramic tapes for electronic applications," *Materials*

Science and Engineering: B, vol. 177, no. 13, pp. 1053-1066, 8/1/ 2012, doi:

http://dx.doi.org/10.1016/j.mseb.2012.05.015.

[68]   J. S. Kang, H. S. Kim, J. Ryu, H. T. Hahn, S. Jang, and J. W. Joung, "Inkjet printed electronics using

copper nanoparticle ink," *Journal of Materials Science: Materials in Electronics,* vol. 21, no. 11,

pp. 1213-1220, 2010.

[69]   D. Huang, F. Liao, S. Molesa, D. Redinger, and V. Subramanian, "Plastic-compatible low

        resistance printable gold nanoparticle conductors for flexible electronics," *Journal of the*

        electrochemical society, vol. 150, no. 7, pp. G412-G417, 2003.

[70]   Y. J. Lee, C. Lee, and H. M. Lee, "Synthesis of oxide-free aluminum nanoparticles for application

        to conductive film," *Nanotechnology,* vol. 29, no. 5, p. 055602, 2018.

[71]   "Price, ICI-003, Copper Oxide Inkjet Ink, 50mL." https://store.novacentrix.com/Metalon-ICI-003-

        copper-oxide-inkjet-ink-p/910-0059-01.htm (accessed 2020).

[72]   "Price, JS-A102A, Silver Inkjet Ink, 50mL." https://store.novacentrix.com/product-p/910-0106-

        01.htm (accessed 2020).

[73]   J. Niittynen, R. Abbel, M. Mäntysalo, J. Perelaer, U. S. Schubert, and D. Lupo, "Alternative

        sintering methods compared to conventional thermal sintering for inkjet printed silver

        nanoparticle ink," *Thin Solid Films,* vol. 556, pp. 452-459, 2014.

[74]   X. Wu, S. Shao, Z. Chen, and Z. Cui, "Printed highly conductive Cu films with strong adhesion

        enabled by low-energy photonic sintering on low-Tg flexible plastic substrate," *Nanotechnology,*

        vol. 28, no. 3, p. 035203, 2016.

[75]   Y. Lee, J.-r. Choi, K. J. Lee, N. E. Stott, and D. Kim, "Large-scale synthesis of copper nanoparticles

        by chemically controlled reduction for applications of inkjet-printed electronics,"

        Nanotechnology, vol. 19, no. 41, p. 415604, 2008.

[76]   J. Cheon, J. Lee, and J. Kim, "Inkjet printing using copper nanoparticles synthesized by

        electrolysis," *Thin Solid Films,* vol. 520, no. 7, pp. 2639-2643, 2012.

[77]   S. P. Chen, H. L. Chiu, P. H. Wang, and Y. C. Liao, "Inkjet printed conductive tracks for printed

        electronics," *ECS Journal of Solid State Science and Technology,* vol. 4, no. 4, pp. P3026-P3033,

        2015.

[78]   "Cost of copper nanoparticles."

https://www.ssnano.com/inc/sdetail/copper_nanoparticles_nanopowder__cu__99_9__100_13

0nm_/21194 (accessed 2020).

[79]   "Cost of silver nanoparticles." https://www.novarials-store.com/collections/all-

nanoparticles/products/silver-nanoparticles-100nm (accessed 2020).

[80]   W. Zapka, *Handbook of Industrial Inkjet Printing: A Full System Approach*. John Wiley & Sons,

2017.

[81]   "Cost of silver salts." https://www.sigmaaldrich.com/materials-science/material-science-

products.html?TablePage=19295364 (accessed 2020).

[82]   "Cost of copper salt." https://www.alfa.com/en/catalog/A18569/ (accessed 2020).

[83]   B. Lee, Y. Kim, S. Yang, I. Jeong, and J. Moon, "A low-cure-temperature copper nano ink for

highly conductive printed electrodes," *Current Applied Physics,* vol. 9, no. 2, Supplement, pp.

e157-e160, 3// 2009, doi: http://dx.doi.org/10.1016/j.cap.2009.03.008.

[84]   M. F. A. M. van Hest *et al.*, "Direct-write contacts: Metallization and contact formation," 2008:

IEEE, pp. 1-3.

[85]   G. Cummins, R. Kay, J. Terry, M. P. Y. Desmulliez, and A. J. Walton, "Optimization and

characterization of drop-on-demand inkjet printing process for platinum organometallic inks,"

2011: IEEE, pp. 256-261.

[86]   H. M. Nur, J. H. Song, J. R. G. Evans, and M. J. Edirisinghe, "Ink-jet printing of gold conductive

tracks," *Journal of Materials Science: Materials in Electronics,* vol. 13, no. 4, pp. 213-219, 2002.

[87]   C. J. Curtis, A. Miedaner, M. F. A. M. Van Hest, and D. S. Ginley, "Printing aluminum films and

patterned contacts using organometallic precursor inks," ed: Google Patents, 2010.

[88]   Y.-I. Lee and Y.-H. Choa, "Adhesion enhancement of ink-jet printed conductive copper patterns

on a flexible substrate," *Journal of Materials Chemistry,* vol. 22, no. 25, pp. 12517-12522, 2012.

[89] E.-B. Jeon, S.-J. Joo, H. Ahn, and H.-S. Kim, "Two-step flash light sintering process for enhanced adhesion between copper complex ion/silane ink and a flexible substrate," *Thin Solid Films,* vol. 603, pp. 382-390, 2016.

[90] A. L. a. S. P. J. a. S. D.-Y. a. R. N. a. D. B. a. O. B. P. Dearden, "A Low Curing Temperature Silver Ink for Use in Ink-Jet Printing and Subsequent Production of Conductive Tracks," *Macromolecular Rapid Communications,* vol. 26, no. 4, pp. 315--318, 2005, doi: 10.1002/marc.200400445.

[91] E. H. a. A. W. M. d. L. a. U. S. S. Jolke Perelaer and Chris, "One-step inkjet printing of conductive silver tracks on polymer substrates," *Nanotechnology,* vol. 20, no. 16, p. 165303, 2009.

[92] S. M. B. a. D. M. L. a. M. C. a. A. V. a. P. A. M. a. D. McGorman, "Ink-jet fabrication of electronic components," *Journal of Micromechanics and Microengineering,* vol. 17, no. 5, p. 967, 2007.

[93] S. F. Jahn *et al.*, "Inkjet printing of conductive silver patterns by using the first aqueous particle-free MOD ink without additional stabilizing ligands," *Chemistry of materials,* vol. 22, no. 10, pp. 3067-3071, 2010.

[94] H. Kang, E. Sowade, and R. R. Baumann, "Direct intense pulsed light sintering of inkjet-printed copper oxide layers within six milliseconds," *ACS applied materials & interfaces,* vol. 6, no. 3, pp. 1682-1687, 2014.

[95] J. Lee, B. Lee, S. Jeong, Y. Kim, and M. Lee, "Enhanced surface coverage and conductivity of Cu complex ink-coated films by laser sintering," *Thin Solid Films,* vol. 564, pp. 264-268, 2014.

[96] T. Rivkin, C. Curtis, A. Miedaner, J. Perkins, J. Alleman, and D. Ginley, "Direct write processing for photovoltaic cells," 2002: IEEE, pp. 1326-1329.

[97] A. Kamyshny, J. Steinke, and S. Magdassi, "Metal-based ink jet inks for printed electronics," *Open Appl. Phys. J.Open Applied Physics Journal,* vol. 4, 2011.

[98] G. Li, X. Wu, and D.-W. Lee, "A galinstan-based inkjet printing system for highly stretchable electronics with self-healing capability," *Lab on a Chip,* vol. 16, no. 8, pp. 1366-1373, 2016.

[99]   "Cost of gallium alloys." https://www.rotometals.com/low-melting-point-alloy-galinstan-68-5-ga-21-5-in-10-sn-50-grams/ (accessed 2020).

[100]   K. B. Perez and C. B. Williams, "Combining additive manufacturing and direct write for integrated electronics—a review," 2013, pp. 962-979.

[101]   B. Li, P. A. Clark, and K. H. Church, "Robust direct-write dispensing tool and solutions for micro/meso-scale manufacturing and packaging," 2007: American Society of Mechanical Engineers, pp. 715-721.

[102]   L.-J. Wei and C. H. Oxley, "Carbon based resistive strain gauge sensor fabricated on titanium using micro-dispensing direct write technology," *Sensors and Actuators A: Physical,* vol. 247, pp. 389-392, 2016.

[103]   T. H. J. a. P. J. a. d. L. A. W. M. a. S. U. S. van Osch, "Inkjet Printing of Narrow Conductive Tracks on Untreated Polymeric Substrates," *Advanced Materials,* vol. 20, no. 2, pp. 343--345, 2008, doi: 10.1002/adma.200701876.

[104]   H. Sirringhaus and T. Shimoda, "Inkjet printing of functional materials," *MRS bulletin,* vol. 28, no. 11, pp. 802-806, 2003.

[105]   R. Tao *et al.*, "Homogeneous Surface Profiles of Inkjet-Printed Silver Nanoparticle Films by Regulating Their Drying Microenvironment," *The Journal of Physical Chemistry C,* vol. 121, no. 16, pp. 8992-8998, 2017/04/27 2017, doi: 10.1021/acs.jpcc.6b12793.

[106]   T. R. Hebner, C. C. Wu, D. Marcy, M. H. Lu, and J. C. Sturm, "Ink-jet printing of doped polymers for organic light emitting devices," *Applied Physics Letters,* vol. 72, no. 5, pp. 519-521, 1998.

[107]   K. E. Paul, W. S. Wong, S. E. Ready, and R. A. Street, "Additive jet printing of polymer thin-film transistors," *Applied Physics Letters,* vol. 83, no. 10, pp. 2070-2072, 2003.

[108]   T.-F. Guo, S.-C. Chang, S. Pyo, and Y. Yang, "Vertically integrated electronic circuits via a combination of self-assembled polyelectrolytes, ink-jet printing, and electroless metal plating processes," *Langmuir,* vol. 18, no. 21, pp. 8142-8147, 2002.

[109]   S. Khan, L. Lorenzelli, and R. S. Dahiya, "Technologies for printing sensors and electronics over large flexible substrates: a review," *IEEE Sensors Journal,* vol. 15, no. 6, pp. 3164-3185, 2015.

[110]   M. Orme, "A novel technique of rapid solidification net- form materials synthesis," *Journal of Materials Engineering and Performance,* vol. 2, no. 3, pp. 399-405, 1993.

[111]   R. F. S. Melissa Orme, "Enhanced Aluminum Properties by means of precise droplet deposition," *ASME Journal of Manufacturing Science and Engineering,* vol. 122, pp. 484-493, 2000.

[112]   J. W. Priest, H. Bordett, C. V. Smith Jr, P. DuBois, D. G. Vanecek, and B. R. Holt, "Liquid Metal-Jetting: Its Application to SMT," *Journal of Surface Mount Technology,* vol. 6, no. 5, pp. 4-9, 1993.

[113]   H. Hieber, "Method of applying small drop-shaped quantities of melted solder from a nozzle to surfaces to be wetted and device for carrying out the method," ed: Google Patents, 1989.

[114]   D. J. Hayes, M. T. Boldman, and D. B. Wallace, "Method and apparatus for dispensing spherical-shaped quantities of liquid solder," ed: Google Patents, 1993.

[115]   J.-H. Chun and C. H. Passow, "Production of charged uniformly sized metal droplets," ed: Google Patents, 1993.

[116]   M. E. Orme and E. P. Muntz, "Method and apparatus for droplet stream manufacturing," ed: Google Patents, 1993.

[117]   T. M. Smith and R. E. Winstead, "Electrodynamic pump for dispensing molten solder," ed: Google Patents, 1995.

[118] A. A. Tseng, M. H. Lee, and B. Zhao, "Design and Operation of a Droplet Deposition System for Freeform Fabrication of Metal Parts," *Journal of Engineering Materials and Technology,* vol. 123, no. 1, pp. 74-84, 1999, doi: 10.1115/1.1286187.

[119] R. Berkhout, W. P. J. Classens, H. C. M. Van Genuchten, and E. V. Kuznetsov, "Device for ejecting droplets of a fluid having a high temperature," ed: Google Patents, 2013.

[120] E. M. Sachs, M. G. Gibson, P. A. Hoisington, and R. R. Fontana, "Magnetohydrodynamic deposition of metal in manufacturing," ed: Google Patents, 2017.

[121] M. Suter, E. Weingärtner, and K. Wegener, "MHD printhead for additive manufacturing of metals," *Procedia CIRP,* vol. 2, pp. 102-106, 2012/01/01/ 2012, doi: https://doi.org/10.1016/j.procir.2012.05.049.

[122] M. Suter, "Printing cell and printing head for printing of molten metals,"

[123] P. A. Sackinger, M. Essien, H. C. Peebles, and E. M. Schlienger, "Apparatus for jet application of molten metal droplets for manufacture of metal parts," ed: Google Patents, 2001.

[124] S. H. G. Joppen and H. M. A. Wijshoff, "Method for jetting droplets of an electrically conductive fluid," ed: Google Patents, 2017.

[125] S. Vader and Z. Vader, "Conductive liquid three dimensional printer," ed: Google Patents, 2017.

[126] S. Chandra and R. Jivraj, "Apparatus and method for generating droplets," ed: Google Patents, 2002.

[127] "Method for ejecting molten metals," ed: Google Patents, 2016.

[128] H. Ohashi, H. Ushijima, and K. Horibe, "Method for producing circuitry using molten metal droplets," ed: Google Patents, 2006.

[129] "Cost of aluminum 4043 feed wire." https://www.fastenal.com/products/details/0865021 (accessed 2020).

[130] M. Ree, H. Han, and C. C. Gryte, "Water sorption in thin films of high-temperature polyimides: the effect of imidization history," *High Performance Polymers,* vol. 6, no. 4, pp. 321-334, 1994.

[131] K. L. Mittal, *Polyimides: synthesis, characterization, and applications*. Springer Science & Business Media, 2013.

[132] M. Simonelli *et al.*, "Towards digital metal additive manufacturing via high-temperature drop-on-demand jetting," *Additive Manufacturing,* vol. 30, p. 100930, 2019.

[133] D. Soltman and V. Subramanian, "Inkjet-Printed Line Morphologies and Temperature Control of the Coffee Ring Effect," *Langmuir,* vol. 24, no. 5, pp. 2224-2231, 2008/03/01 2008, doi: 10.1021/la7026847.

[134] I. M. Hutchings and G. D. Martin, *Inkjet technology for digital fabrication*. John Wiley & Sons, 2012.

[135] L.-h. Qi, S.-y. Zhong, J. Luo, D.-c. Zhang, and H.-s. Zuo, "Quantitative characterization and influence of parameters on surface topography in metal micro-droplet deposition manufacture," *International Journal of Machine Tools and Manufacture,* vol. 88, pp. 206-213, 2015.

[136] M. Y. Koledintseva, A. G. Razmadze, A. Y. Gafarov, S. De, J. L. Drewniak, and S. Hinaga, "PCB conductor surface roughness as a layer with effective material parameters," 2012: IEEE, pp. 138-143.

[137] S. Chandra and C. T. Avedisian, "On the collision of a droplet with a solid surface," *Proceedings of the Royal Society of London. Series A: Mathematical and Physical Sciences,* vol. 432, no. 1884, pp. 13-41, 1991.

[138] J. San Lee, B. M. Weon, J. H. Je, and K. Fezzaa, "How does an air film evolve into a bubble during drop impact?," *Physical review letters,* vol. 109, no. 20, p. 204501, 2012.

[139] L. Xu, W. W. Zhang, and S. R. Nagel, "Drop splashing on a dry smooth surface," *Physical review letters,* vol. 94, no. 18, p. 184505, 2005.

[140] W. Bouwhuis *et al.*, "Maximal air bubble entrainment at liquid-drop impact," *Physical review letters,* vol. 109, no. 26, p. 264501, 2012.

[141] J. de Ruiter, J. M. Oh, D. van den Ende, and F. Mugele, "Dynamics of collapse of air films in drop impact," *Physical review letters,* vol. 108, no. 7, p. 074505, 2012.

[142] M. M. Driscoll and S. R. Nagel, "Ultrafast interference imaging of air in splashing dynamics," *Physical review letters,* vol. 107, no. 15, p. 154502, 2011.

[143] C. Josserand and S. T. Thoroddsen, "Drop impact on a solid surface," *Annual review of fluid mechanics,* vol. 48, pp. 365-391, 2016.

[144] J. de Ruiter, D. van den Ende, and F. Mugele, "Air cushioning in droplet impact. II. Experimental characterization of the air film evolution," *Physics of fluids,* vol. 27, no. 1, p. 012105, 2015.

[145] J. M. Kolinski, S. M. Rubinstein, S. Mandre, M. P. Brenner, D. A. Weitz, and L. Mahadevan, "Skating on a film of air: drops impacting on a surface," *Physical review letters,* vol. 108, no. 7, p. 074503, 2012.

[146] W. Xiong and P. Cheng, "Numerical investigation of air entrapment in a molten droplet impacting and solidifying on a cold smooth substrate by 3D lattice Boltzmann method," *International Journal of Heat and Mass Transfer,* vol. 124, pp. 1262-1274, 2018.

[147] S. Schiaffino and A. A. Sonin, "Molten droplet deposition and solidification at low Weber numbers," *Physics of fluids,* vol. 9, no. 11, pp. 3172-3187, 1997.

[148] V. Mehdi-Nejad, J. Mostaghimi, and S. Chandra, "Air bubble entrapment under an impacting droplet," *Physics of fluids,* vol. 15, no. 1, pp. 173-183, 2003.

[149] M. Qu, Y. Wu, V. Srinivasan, and A. Gouldstone, "Observations of nanoporous foam arising from impact and rapid solidification of molten Ni droplets," *Applied physics letters,* vol. 90, no. 25, p. 254101, 2007.

[150]   H. Yi, L.-h. Qi, J. Luo, Y. Jiang, and W. Deng, "Pinhole formation from liquid metal microdroplets impact on solid surfaces," *Applied Physics Letters,* vol. 108, no. 4, p. 041601, 2016.

[151]   R. K. Shukla, A. Kumar, R. Kumar, D. Singh, and A. Kumar, "Numerical study of pore formation in thermal spray coating process by investigating dynamics of air entrapment," *Surface and Coatings Technology,* vol. 378, p. 124972, 2019.

[152]   R. Kumar, R. K. Shukla, A. Kumar, and A. Kumar, "A computational study on air entrapment and its effect on convective heat transfer during droplet impact on a substrate," *International Journal of Thermal Sciences,* vol. 153, p. 106363, 2020.

[153]   P. G. Pittoni, Y.-C. Lin, R.-J. Wang, T.-S. Yu, and S.-Y. Lin, "Bubbles entrapment for drops impinging on polymer surfaces: The roughness effect," *Experimental Thermal and Fluid Science,* vol. 62, pp. 183-191, 2015.

[154]   I. H. Karampelas *et al.*, "Drop-on-demand 3D metal printing," *Informatics, Electronics and Microsystems,* pp. 153-155, 2017.

[155]   V. Sukhotskiy *et al.*, "Magnetohydrodynamic drop-on-demand liquid metal 3D printing," *Proceedings of the Solid Freeform Fabrication,* 2017.

[156]   J. Kestin, S. T. Ro, and W. A. Wakeham, "Viscosity of the noble gases in the temperature range 25–700 C," *The Journal of Chemical Physics,* vol. 56, no. 8, pp. 4119-4124, 1972.

[157]   I. F. Bainbridge and J. A. Taylor, "The surface tension of pure aluminum and aluminum alloys," *Metallurgical and Materials Transactions A,* vol. 44, no. 8, pp. 3901-3909, 2013.

[158]   "Dupont™ kapton® summary of properties." https://www.dupont.com/content/dam/dupont/amer/us/en/products/ei-transformation/documents/DEC-Kapton-summary-of-properties.pdf (accessed 08/05/2020, 2020).

[159] H. Haghighi and I. Cotton, "Analysis of the Degradation Kinetics of Kapton Film in an Aerospace Environment," 2019: IEEE, pp. 1-4.

[160] D.-K. Yang, W. J. Koros, H. B. Hopfenberg, and V. T. Stannett, "Sorption and transport studies of water in Kapton polymide. I," *Journal of applied polymer science,* vol. 30, no. 3, pp. 1035-1047, 1985.

[161] M. Akram, K. M. B. Jansen, S. Bhowmik, and L. J. Ernst, "Moisture absorption analysis of high performance polyimide adhesive," 2011: SAMPE.

[162] B. Bensaid, X. Boddaert, P. Benaben, R. Gwoziecki, and R. Coppard, *Reliability of OTFTs on flexible substrate: Mechanical stress effect*. 2011.

[163] H.-Y. Lee, S.-M. Yi, J.-H. Lee, H.-S. Lee, S. Hyun, and Y.-C. Joo, "Effects of bending fatigue on the electrical resistance in metallic films on flexible substrates," *Metals and Materials International,* vol. 16, no. 6, pp. 947-951, 2010/12/01 2010, doi: 10.1007/s12540-010-1213-2.

[164] S. I. Park, J. H. Ahn, X. Feng, S. Wang, Y. Huang, and A. Rogers John, "Theoretical and Experimental Studies of Bending of Inorganic Electronic Materials on Plastic Substrates," *Advanced Functional Materials,* vol. 18, no. 18, pp. 2673-2684, 2008/09/23 2008, doi: 10.1002/adfm.200800306.

[165] S. Grego, J. Lewis, E. Vick, and D. Temple, "Development and evaluation of bend-testing techniques for flexible-display applications," *Journal of the Society for Information Display,* vol. 13, no. 7, pp. 575-581, 2005/07/01 2012, doi: 10.1889/1.2001215.

[166] K. Alzoubi, S. Lu, B. Sammakia, and M. Poliks, "Factor Effect Study for the High Cyclic Bending Fatigue of Thin Films on PET Substrate for Flexible Displays Applications," *Journal of Display Technology,* vol. 7, no. 6, pp. 348-355, 2011, doi: 10.1109/JDT.2010.2076772.

[167] M. Yang *et al.*, "Mechanical and environmental durability of roll-to-roll printed silver nanoparticle film using a rapid laser annealing process for flexible electronics," *Microelectronics*

Reliability, vol. 54, no. 12, pp. 2871-2880, 2014/12/01/ 2014, doi:

https://doi.org/10.1016/j.microrel.2014.07.004.

[168]   O. Glushko, M. J. Cordill, A. Klug, and E. J. W. List-Kratochvil, "The effect of bending loading

conditions on the reliability of inkjet printed and evaporated silver metallization on polymer

substrates," *Microelectronics Reliability,* vol. 56, pp. 109-113, 2016/01/01/ 2016, doi:

https://doi.org/10.1016/j.microrel.2015.10.007.

[169]   T. Happonen, J. Häkkinen, and T. Fabritius, "Cyclic bending reliability of silk screen printed silver

traces on plastic and paper substrates," *IEEE Transactions on Device and Materials Reliability,*

vol. 15, no. 3, pp. 394-401, 2015.

[170]   A. A. Abdallah, P. C. P. Bouten, and G. de With, "Experimental study on buckle evolution of thin

inorganic layers on a polymer substrate," *Engineering Fracture Mechanics,* vol. 77, no. 14, pp.

2896-2905, 2010/09/01/ 2010, doi: https://doi.org/10.1016/j.engfracmech.2010.07.012.

[171]   B. Huber, J. Schober, M. Kaiser, A. Ruediger, and C. Schindler, "Rotate-to-bend setup for fatigue

bending tests on inkjet-printed silver lines," *Flexible and Printed Electronics,* vol. 3, no. 3, p.

035005, 2018.

[172]   S.-M. Yi, I.-S. Choi, B.-J. Kim, and Y.-C. Joo, "Reliability issues and solutions in flexible electronics

under mechanical fatigue," *Electronic Materials Letters,* vol. 14, no. 4, pp. 387-404, 2018.

[173]   O. Glushko, A. Klug, E. J. W. List-Kratochvil, and M. J. Cordill, "Monotonic and cyclic mechanical

reliability of metallization lines on polymer substrates," *Journal of Materials Research,* vol. 32,

no. 9, pp. 1760-1769, 2017.

[174]   B. Kang, Z. Zhao, and D. Poulikakos, "Solidification of liquid metal droplets impacting

sequentially on a solid surface," *Journal of Heat Transfer,* vol. 116, no. 2, pp. 436-445, 1994.

[175]   T. Bennett and D. Poulikakos, "Heat transfer aspects of splat-quench solidification: modelling

and experiment," *Journal of Materials Science,* vol. 29, no. 8, pp. 2025-2039, 1994.

[176]   G. Trapaga, E. F. Matthys, J. J. Valencia, and J. Szekely, "Fluid flow, heat transfer, and solidification of molten metal droplets impinging on substrates: comparison of numerical and experimental results," *Metallurgical Transactions B,* vol. 23, no. 6, pp. 701-718, 1992.

[177]   J. M. Waldvogel and D. Poulikakos, "Solidification phenomena in picoliter size solder droplet deposition on a composite substrate," *International Journal of Heat and Mass Transfer,* vol. 40, no. 2, pp. 295-309, 1997.

[178]   Z. Zhao, D. Poulikakos, and J. Fukai, "Heat transfer and fluid dynamics during the collision of a liquid droplet on a substrate—I. Modeling," *International Journal of Heat and Mass Transfer,* vol. 39, no. 13, pp. 2771-2789, 1996.

[179]   S. Kamnis, S. Gu, T. J. Lu, and C. Chen, "Numerical modelling of sequential droplet impingements," *Journal of Physics D: Applied Physics,* vol. 41, no. 16, p. 165303, 2008.

[180]   H. Tabbara and S. Gu, "Modelling of impingement phenomena for molten metallic droplets with low to high velocities," *International Journal of Heat and Mass Transfer,* vol. 55, no. 7-8, pp. 2081-2086, 2012.

[181]   M. Pasandideh-Fard, V. Pershin, S. Chandra, and J. Mostaghimi, "Splat shapes in a thermal spray coating process: simulations and experiments," *Journal of Thermal Spray Technology,* vol. 11, no. 2, pp. 206-217, 2002.

[182]   M. Pasandideh-Fard, S. Chandra, and J. Mostaghimi, "A three-dimensional model of droplet impact and solidification," *International Journal of Heat and Mass Transfer,* vol. 45, no. 11, pp. 2229-2242, 2002.

[183]   Y. Z. Zheng, Q. Li, Z. H. Zheng, J. F. Zhu, and P. L. Cao, "Modeling the impact, flattening and solidification of a molten droplet on a solid substrate during plasma spraying," *Applied Surface Science,* vol. 317, pp. 526-533, 2014.

[184]   M. Sussman, P. Smereka, and S. Osher, "A level set approach for computing solutions to incompressible two-phase flow," *Journal of Computational physics,* vol. 114, no. 1, pp. 146-159, 1994.

[185]   A. Kumar, S. Ghosh, and B. K. Dhindaw, "Simulation of cooling of liquid Al–33 wt.% Cu droplet impinging on a metallic substrate and its experimental validation," *Acta Materialia,* vol. 58, no. 1, pp. 122-133, 2010.

[186]   V. R. Voller and C. Prakash, "A fixed grid numerical modelling methodology for convection-diffusion mushy region phase-change problems," *International Journal of Heat and Mass Transfer,* vol. 30, no. 8, pp. 1709-1719, 1987.

[187]   S. K. a. S. Gu, "Numerical modelling of droplet impingement," *Journal of Physics D: Applied Physics,* vol. 38, no. 19, p. 3664, 2005.

[188]   J. P. Van Doormaal, G. D. Raithby, and B. H. McDonald, "The segregated approach to predicting viscous compressible fluid flows," 1986: American Society of Mechanical Engineers, pp. V001T01A084-V001T01A084.

[189]   M. Perić, "Analysis of pressure-velocity coupling on nonorthogonal grids," *Numerical Heat Transfer,* vol. 17, no. 1, pp. 63-82, 1990.

[190]   B. P. Leonard, "Order of accuracy of QUICK and related convection-diffusion schemes," 1993.

[191]   J. U. Brackbill, D. B. Kothe, and C. Zemach, "A continuum method for modeling surface tension," *Journal of computational physics,* vol. 100, no. 2, pp. 335-354, 1992.

[192]   S.-y. Zhong, L.-h. Qi, J. Luo, H.-s. Zuo, X.-h. Hou, and H.-j. Li, "Effect of process parameters on copper droplet ejecting by pneumatic drop-on-demand technology," *Journal of materials processing technology,* vol. 214, no. 12, pp. 3089-3097, 2014.

[193]   "Cost of polyimide film." https://www.professionalplastics.com/skapt.005x24.000hn-lb?utm_medium=shoppingengine&utm_source=googlebase&utm_campaign=googlebase&dfw_

tracker=36203-SKAPT.005X24.000HN-

LB&gclid=Cj0KCQjwu7OIBhCsARIsALxCUaOyi7WlZ1PxeLzTiu5Wh4gCEbsua7v7J-

9CA2M9CIqNnqHQJfjOfcsaAqaQEALw_wcB (accessed 2021).

[194]   "Cost of PET film."

https://www.usplastic.com/catalog/item.aspx?itemid=36640&gclid=Cj0KCQjwu7OIBhCsARIsALx

CUaPyU3dz1OW7kYih5vN58o1RiFHtteM6O4vfHX8kD5yHPohXjliGoOAaAudqEALw_wcB

(accessed 2021).